AN ABSTRACT OF THE THESIS OF

Steven E. Sloop for the degree of Doctor of Philosophy in Chemistry presented on May 2, 1996. Title: Synthesis and Characterization of Polymer Electrolytes and Related Nanocomposites.

Abstract approved: Redacted for Privacy

Michael M. Lerner

A general introduction, and review of materials investigated for use in solid state batteries is provided in chapters 1 and 2. These include descriptions of cathode, anode and electrolyte materials, fundamental properties of polymer electrolytes (PEs), and electrode / electrolyte interfaces, as well as an outline of the mechanical, and electrochemical requirements of polymer electrolytes. Chapter 3 describes the experimental techniques utilized in these investigations. Chapter 4 reports the results of an investigation into crosslinking poly(ethylene oxide) and poly[oxymethylene-oligo(oxyethylene)] with ultraviolet radiation. The ionic conductivity of the UV crosslinked PE is shown to be similar to PEs derived from the linear electrolytes. Polymer rheology demonstrates an increase in dynamic modulus with the exposure of PEO or PEM to 254nm radiation. The crosslink density decreases with depth into these disks, and a relatively high concentration of hydroxyl resides on the surface of the crosslinked polymers. A GCMS investigation of the degradation products of crosslinked PEO in HBr/Acetic acid reveals a possible reaction mechanism for crosslink formation, which is proposed. Chapter 5 investigates Li/PE interfacial characteristics of PEs derived from UV crosslinked PEO, and PEM.

Crosslinked films develop interfacial resistance in the mega-Ω cm^2 range, upon addition of polyethylene glycol dimethyl ether (PEGDME), or treatment with a methylating, or silylating agent, these PEs maintain interfacial resistances (350 - 1000 Ωcm^2) similar to their linear PEs. In Chapter 6, PE/electrode interfaces of cathodes derived from $Li_xPEO_yMoO_3$ have resistances near 250 Ω cm^2, while those derived from $Li_{0.25}MoO_3$ have resistances near 20,000 Ω cm^2 at 60° C, and suggest that incorporation of PEO within layered cathode materials lowers the PE interfacial resistance. Chapter 7 describes the incorporation of polyethylene imine (PEI) into $HTiNbO_5$ and $H_xTi_{2-x/4}\square_{x/4}O_4 \cdot H_2O$. The products of aqueous reactions show maximum layer expansions of ~28 Å in both solids. The $HTiNbO_5$ - PEI reaction progresses through phases with layer expansions of 4, 10, 14 and 28 Å, the reaction rate is influenced by the pH of the solution, and slows progressively below pH~10.

Synthesis and Characterization of Polymer Electrolytes and Related Nanocomposites

by

Steven E. Sloop

A THESIS

submitted to

Oregon State University

in partial fulfillment of
the requirements for the
degree of

Doctor of Philosophy

Completed May 2, 1996
Commencement June 1996

Doctor of Philosophy thesis of Steven E. Sloop presented on May 2, 1996

APPROVED:

Redacted for Privacy

Major Professor, representing Chemistry

Redacted for Privacy

Chair of the Department of Chemistry

Redacted for Privacy

Dean of the Graduate School

I understand that my thesis will become part of the permanent collection of Oregon State University libraries. My signature below authorizes release of my thesis to any reader upon request.

Redacted for Privacy

Steven E. Sloop, Author

ACKNOWLEDGMENT

I would like to thank my mentor, Mike Lerner for his guidance through my graduate experience. As the years progress, may students always locate Mike *in the lab*. Also, I would like to thank my friends and colleagues which I met in the Lerner Lab: John Lemmon, Zhengwei Zhang, Jinhe Wu, Rick Nafshun, Chris Oriakhi, Gary Ramachandran, I will remember the ideas and friendship shared, and look forward to the times when we may continue these conversations.

I am thankful for the love of my family, and my friends, without which this dream would not have been possible.

> If one advances confidently in the direction of his dreams, and endeavors to live the life which he has imagined, he will meet with a success unexpected in common hours.
>
> -Thoreau

CONTRIBUTION OF AUTHORS

Dr. Michael M. Lerner was involved in the design, analysis, and writing of each manuscript. Dr. Thomas S. Stephens, at the U.S. Naval Warfare Laboratory, China Lake, CA. collected rheological data, and reported upon it in Chapter 4. Dr. Scott Hawke, at Willamette University, assisted in the collection of scanning electron micrographs reported upon in Chapter 7.

TABLE OF CONTENTS

TABLE OF CONTENTS CONTINUED

TABLE OF CONTENTS CONTINUED

Page

TABLE OF CONTENTS CONTINUED

Page

TABLE OF CONTENTS CONTINUED

Page

LIST OF FIGURES

LIST OF FIGURES CONTINUED

LIST OF FIGURES CONTINUED

LIST OF FIGURES CONTINUED

LIST OF TABLES

LIST OF REACTION SCHEMES

Scheme **Page**

Synthesis and Characterization of Polymer Electrolytes and Related Nanocomposites

Chapter 1

Introduction

1.0 **Thesis Organization.**

This thesis is divided into 7 sections. Chapter 1 gives a general introduction to cathode, and anode materials for solid state batteries, while Chapter 2 provides a detailed introduction to polymer electrolytes. Chapter 3 concentrates on the preparation, and characterization techniques utilized in crosslinking polyethylene oxide (PEO), and polyoxymethylene oligo oxyethylene (PEM), their nanocomposites with MoO_3, and interfaces with lithium metal. Chapter 4 discusses the characteristic properites of UV crosslinked PEO, and PEM, and presents a description of the photochemical process that may occur. Chapter 5 reports upon the interfacial characteristics of these crosslinked polyethers with lithium metal. Chapter 6 investigates the behavior of a polymer electrolyte interface with the nanocomposite, $Li_xPEO_yMoO_3$. Finally, Chapter 7 reports upon the intercallation of polyethylene imine (PEI) into $HTiNbO_5$, and the layered titanate, $H_xTi_{2-x/4}\square_{x/4}O_4 \cdot H_2O$. Chapter 8 summarizes the overall results.

1.1 **Research Goals.**

Exponential growth in worldwide power consumption over recent generations, and concerns about urban air pollution have motivated research and development of efficiency-

related technology such as high energy density secondary batteries [1,2]. Such batteries may store solar power, excess electrical generation (during off-peak hours), or provide a rechargeable power source for electric vehicles [3,4]. The developmental goal of these secondary batteries is to reversibly harness the theoretical maximum potential energy from lithium-based reactions, which is influenced by the fundamental properties of materials comprising the battery. The electrolyte/electrode components developed in the materials chemists' laboratories should have the following general characteristics: (i) conductive electrode/electrolyte interfaces. (ii) Electrolytes that exhibit high conductivity of cations, mechanical stability, tolerance of high cell voltages, and reversible deposition and striping of lithium from the electrodes. (iii) Electrodes that provide maximum capacity (mAh g^{-1}), and conductivity to and from the electrolyte.

The principal concern of this thesis is the development of mechanical and electrochemical properties of existing polymer electrolytes (PEs) for an all-solid lithium-based battery. This introductory chapter reviews some materials that may be used in such a battery, and provides perspective as to the number of possible secondary batteries and what electrodes may be placed against a PE. Also included is a disscusion of the electrical, and structural changes that accompany lithium incorporation into these cathodes or anodes, as well as some salient definitions.

1.2 **Thermodynamics of Lithium Reactions.**

Lithium occurs naturally in a cationic form that can electrochemically be reduced into metallic lithium. In order to preserve its state, the metal must be stored in an inert

atmosphere or *in vacuo*. Figure 1.1 shows some elements listed according to their standard reduction potential. Of all elements, lithium has the lowest standard reduction potential at -3.045V vs. SHE; therefore, it is a very strong reducing agent [5]. (The remainder of this thesis will use electrode potentials relative to $Li \rightleftharpoons Li^+ + e^-$, $E^\circ=0$). Strong thermodynamic driving forces in lithium chemistry are derived from its low ionization potential (*IP*), and small ionic radius (0.59 - 0.76 Å), which can be demonstrated in Hess's Law describing the formation of a lithium halide [6]:

$$\Delta H_f = H_S + 1/2D + IP + EA + U \qquad (1.1)$$

where H_S is the sublimation energy of the solid metal, D is the dissociation energy of a molecular halogen, EA is the electron affinity of the halogen atom, and U represents the energy of coalescence of the gaseous ions to form a crystal (lattice energy). The small cationic size contributes to high lattice energies within its salts, as demonstrated by the

$$U = \frac{1200.5 V Z_+ Z_-}{r_c + r_a} \left(1 - \frac{0.345}{r_c + r_a}\right) kJmol^{-1} \qquad (1.2)$$

minimization of cationic radius (r_c) and anionic radius (r_a) in Katpustinskii's equation [6]: Where V is the number of ions per formula unit, and $Z_{+,-}$ are their charges.

Ethers and polyethers demonstrate kinetic stability against metallic lithium near room temperature. No visible reaction immediately occurs when lithium is placed in etheric solvents (such as tetrahydrofuran - THF - , diethyl ether, or polyethylene oxide). On the other hand, reactions occur rapidly at room temperature in water or alcohol, where

Couple	E° / V
$F_2 + 2e^- \rightarrow 2F^-$	+ 2.87
$Fe^{3+} + e^- \rightarrow Fe^{2+}$	+ 0.77
$[PtCl_4]^{2-} + 2e^- \rightarrow Pt + 4Cl^-$	+ 0.60
$2H^+ + 2e^- \rightarrow H_2$	0.0
$Zn^{2+} + 2e^- \rightarrow Zn$	- 0.76
$Al^{3+} + 3e^- \rightarrow Al$	- 1.68
$Mg^{2+} + 2e^- \rightarrow Mg$	- 2.36
$Na^+ + e^- \rightarrow Na$	- 2.71
$Ca^{2+} + 2e^- \rightarrow Ca$	- 2.87
$Li^+ + e^- \rightarrow Li$	- 3.05

Figure 1.1. Some Standard Reduction Potentials at 25°C.

the hydroxyl functionality, with its labile O-H bond, easily contacts the lithium metal surface, causing oxidation of the metal, and the formation of lithium alkoxides and oxides [7]:

$$2ROH + 2Li \rightarrow 2ROLi + H_2 \qquad (1.3)$$

1.3 **Battery Performance and Anodic Lithium Compounds.**

The energy density of a battery is defined as the free energy of anode oxidation and cathode reduction per battery volume: Wh cm^{-3}. Specific energy density is expressed in units of energy per mass: Wh kg^{-1} [8]. Capacity refers to the amount of charge stored between the electrodes, and is usually measured in Ah; high energy density batteries utilize high capacity electrodes with a high electrochemical potential difference (voltage). Lithium is an attractive anode because it has the lowest gram density of solid elements, the highest anodic capacity (3.8 Ah g^{-1}), and low toxicity; however, lithium is chemically unstable against most electrolytes. Cell operation, or cycling, involves electrochemical discharge followed by charge. The anode is oxidized during discharge, and the lithium ions produced traverse the electrolyte, intercalate into the cathode until it reaches the (practical) capacity limit. The voltage required for intercalation of the cathode may change during the cycle as it experiences structure changes [9]. Charging is the reverse process, where cations are extracted from the cathode and reduced at the anode. Reduction does not occur evenly on a lithium metal anode, typically, dendrites form and lead to short circuits [8, 10]. These issues direct development of alternate, low potential (Li/Li^+) lithium anodes.

While most lithium compounds are classic salts, some have electrochemical potentials within 1V of lithium metal and share similar properties, the lightest of these may be of interest for battery anodes. Some compounds include alloys, such as LiAl, where the two metals exist as a solid solution.

Carbon is an attractive electrode material for lithium batteries, it is lightweight, nontoxic, inexpensive, and allows for constructing batteries in the discharged state, which reduces the manufacture requirements. There are polymorphs of carbon that vary in degree of crystallinity and may be used as electrodes, these include graphite, coke, carbon black and polyacenic semiconductors [11]. Graphite is a crystalline, layered compound in which each layer (a graphite sheet) consists of a two-dimensional conjugated π-system, with weak bonds existing between the graphite sheets. Coke, and carbon black are porous, low crystallinity structures compared with graphite; however, they still contain multilayered domains of graphite sheets. Polyacenic carbons (Figure 1.2) have a house of cards structure, and each sheet is not expansive, therefore, the concentration of edge sites is much higher than in crystalline graphite, and very few multilayered domains exist in these carbons.

Li/C compounds are synthesized by exposure of carbon to gaseous lithium [12], by reaction with lithium naphthalide in tetrahydrofuran (THF) [13], or by electrochemical reaction of solvated lithium salts and carbon [14]. The intercalated lithium partially transfers its 2s electron into the antibonding molecular orbital on the sheets, these compounds have electrochemical potentials in the range of 0.1-0.5V vs. Li/Li^+ [6, 14]. Lithium intercalation into graphite may be limited by cation-cation repulsion within the

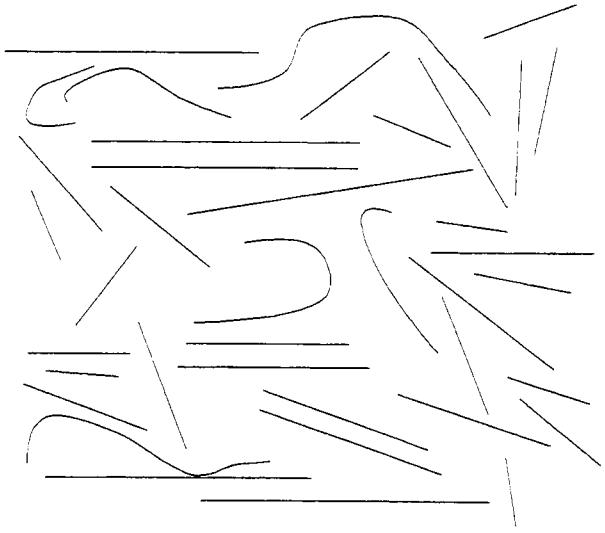

Figure 1.2. The house of cards structure representing polyacenic carbons, these are not coherently stacked layers as in graphite. The edge of a planar, or curved graphitic sheet is depicted.

galleries, the maximum lithium content is Li_1C_6, or a lithium layer for each carbon sheet, which gives a capacity of 372 mAh g^{-1} (Figure 1.3). The application of high pressure (50 kbar at 280°C) can increase the metal content, and produce a chemical potential close to metallic lithium [15]. Polyacenic semiconductors may intercalate lithium past the usual limit of graphite as a result of two factors: their low crystalline, porous, house-of-cards structure allows coverage of both sides of the graphite-like sheets with lithium ions, producing twice the theoretical lithium ion capacity of graphite (740 mAh g^{-1}). Also, an interaction between lithium and sheet-edges is indicated by an increase in capacity with hydrogen content [16]. All of these compounds have reduced capacity with respect to that of lithium metal (3.86 Ah g^{-1}).

1.4 **Lithium Ion Reversible Cathodes.**

Some transition metal oxides and sulfides investigated for use as reversible lithium battery electrodes are summarized in Table 1.1. Solids that contain mobile lithium ions are candidates for battery electrodes, and can serve as cathodes against lithium or Li/C anodes. In lithium ion batteries, the energetic driving force is derived from a limited electrochemical potential difference between electrodes, essentially; these batteries shuttle cations between electrodes. The high voltages that are possible in such electrodes (4 V) contribute to energy density, and pose unique challenges for the electrolyte utilized in cathode/anode separation, as many electrolytes suffer degradation under such conditions.

(a)

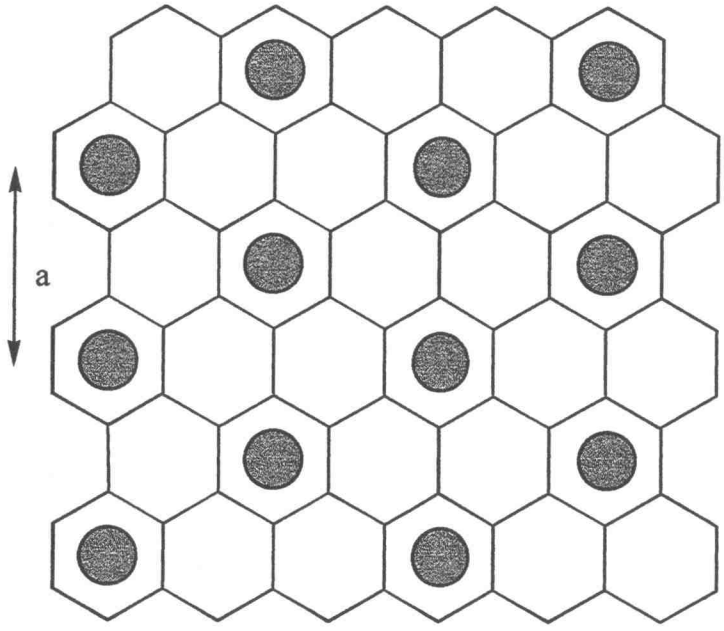

(b)

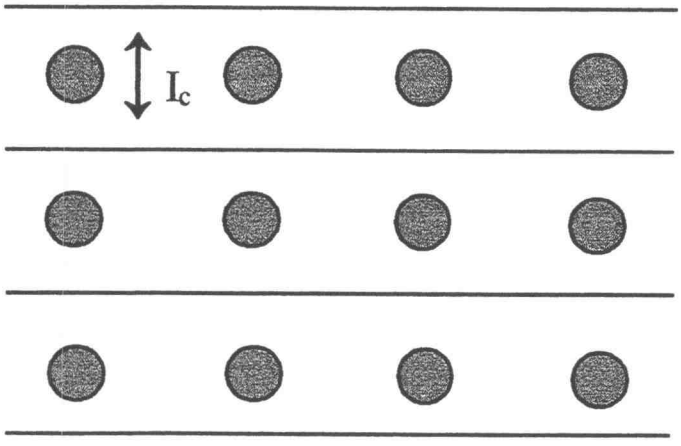

Figure 1.3 The structure of LiC_6, (a) Li^+ is positioned with a hexal structure where a = 4.26 Å (b) the stacking of the compound is AαAα with I_c = 3.706 Å.

Compound	*Voltage* vs. Li/Li^+	*Energy Density (Theoretical)*	*Energy Density (Practical)*	*Structure*	*Comments*
$Li_xV_2O_5$ $Li_xV_3O_8$	3.2 3	- 650 Wh/kg	1600 Wh/kg -	aerogel amorphous	$0 < x < 3$ [35]
WO_2 MoO_2	1 1.4	- 278	- -	rutile	Unstable Li^+cycling [18]
$Li_xFe_2O_3$	low	-	-	corundum	Unstable Li^+cycling [36]
$LiCoO_2$ $LiNiO_2$ $LiVO_2$	4.5 2.8-4.5 -	766 350 -	200 80-100 -	layered MO_2 framework	- - unstable to Li^+cycling [18,25]
$LiMnO_2$	3	-	-	layered	[24]
$Li[Ti_{0.67}Li_{0.33}]O_4$	1.5	-	110	spinel	Stable cycling, anode? [28]
LiV_2O_4, $LiCo_2O_4$ $LiMnO_2$ $LiMn_2O_4$	4 3.5 3.5 4	320 - - -	120 - 220 -	spinel (ramsdellite)	Stable Li^+cycling. - Unstable Li^+cycling [25, 34] Recently Syntheized [37]
$Li_{1.03}Mn_{1.97}O_4$ $LiZn_{0.05}Mn_{1.95}O_4$	4 4	- 159*	- -	"stabilized" spinels	* vs. $Li[Ti_{0.67}Li_{0.33}]O_4$
MoO_3	2	-	-	layered	
TiS_2	2	480	100	layered	
MoS_2	2	-	-	layered	

Table 1.1 Summary of Metal Oxide/Sulfide Electrodes.

Cycling lithium-transition-metal-oxides may affect their capacity, one fundamental reason for capacity loss and low cycle life is related to the structure of the cathode material and changes it may incur upon lithium extraction/insertion [9]. Layered transition metal oxides and spinels display little structure change upon lithium ion insertion/extraction; therefore, these are attractive electrodes for lithium ion cells. Ideally, cell-volume changes occur isotropically, without rearrangement of transition metal, and oxygen ions. Many of these structures are metastable and may nucleate a new phase during charge or discharge, which precludes their use in a secondary cell [17]. Examples of these structure types will be examined below [18].

Hexagonal structures of layered of $LiMO_2$ (M= Co, Ni, V) have close packed oxygen anion arrays, in which every other layer contains octahedrally coordinated transition metal ions; lithium ions migrate in the two dimensional van der Waals gap (gallery) between adjacent oxygen layers. The Ni and Co analogs are attractive battery cathodes [19-23], whereas the Mn and V compounds display serious limitations [24]. When lithium is extracted from $LiVO_2$, the V cations (residing as described above) irreversibly migrate into the gallery and decrease the two-dimensional lithium ion conduction. As the lithium ion content decreases within Co or Ni-oxide layered

compounds, they maintain their structure, interlayer repulsions increase the basal spacing, and the two-dimensional lithium ion conductivity [22, 23].

The spinel frameworks, $Li[M_2]O_4$, provide three-dimensional lithium ion conduction, and can display isotropic volume changes upon lithium cycling [25]. Although, the cubic and orthorhombic spinels display different characteristics, the cubic structures: $Li[M_{1.67}Li_{0.33}]O_4$ (M= Mn, Ti) may cycle numerous times without capacity loss, while the orthorhombic spinel, ramsdellite, (MnO_2) expands 21% upon lithium ion insertion [26, 27]. The cubic spinel has enough cations between every anionic layer to provide the lattice energy to maintain an ideal cubic close packed oxygen array upon de-lithiation; therefore, it tolerates lithium ion extraction/insertion with a volume change of around 1%.

The cubic spinel compound class: $Li[Ti_{1.67}Li_{0.33}]O_4$ has a relatively low electrochemical potential (1.5 V), and may be an anode material. This electrode coupled with a high voltage cathode such as $LiCoO_2$ (4V) could produce a battery with an operating voltage of 2.5 V, or twice that of nickel-cadmium cells [28].

The Mn variant of the cubic spinel, $LiMn_2O_4$ is a viable cathode candidate; however, lithium ion extraction is slowed if the Mn oxidation state falls below 3.5, which occurs when lithium is overloaded into the cathode [25]. This results in a Jahn-Teller

distortion on particle surfaces where low oxidation state (d^4) Mn tetragonally distorts from cubic symmetry [29]. These limitations may be addressed by cell operation management, or optimization of cathode synthesis. Cubic systems of $Li_{1+\delta}Mn_{2-\delta}O_4$ with Mn absent sites have an average manganese ion oxidation state of slightly greater than 3.5, the Jahn-Teller distortion is not observed in these cathodes and they display stability upon cycling [29].

1.5 **Surface-Area Electrode-Performance Relationship.**

The ionic conduction of the electrolyte, and electrodes are important to battery performance. Electrodes with easily accessed reduction sites may attain higher practical capacities over those in which ions topotactically insert through long distances ($1\mu m$) of layers or tunnels. An increase in the surface area of an electrode material will produce a greater practical capacity [30]. Sol-gel processing is effective in producing high surface area solids: vanadium pentoxide (V_2O_5) aerogels prepared from supercritical drying with CO_2 at 32° C and 1200psi creates a surface area of $450m^2/g$ and display a higher level of lithium ion insertion at 3 Li per formula unit instead of 2 Li per formula unit for low surface area amorphous V_2O_5 gels [31]. Also, as an anodic example (discussed earlier), high surface area polyacenic carbons achieve higher capacity than graphite.

1.6 **Polymer Electrolytes.**

In a PE battery, the separation between the cathode and anode could be at most 25 μm, and cell failure can occur if opposing electrodes make contact through a mechanically unstable PE. In summary, there are several desired properties for a PE: (i) mechanical stability, (ii) tolerance of the high voltages (>5 V) required in cycling some cathode materials, (iii) high cationic conductivity (t_+=1), as the anions do not contribute to the reversible electrochemical cell reactions, and (iv) the polymer and solvated salt must be chemically stable against, or able to form a stable interface with the electrodes. All of these characteristics must be maintained from room temperature to about 120°C [32, 33].

Currently, there is no electrolyte that meets all of these qualifications, but PE's are attractive candidates for such a system. The fundamentals of PE's with respect to conductivity, cation solvation, as well as their developments are discussed in the following chapter. Research into crosslinking PEs with UV radiation for improvement of mechanical stability is treated in Chapter 4. The interfacial properties of UV-crosslinked PEs are covered in Chapter 5, and Chapter 6.

1.7 **References.**

1. Cohen, J. E. *Science* **1995**, *269*, 341.

2. Suziki, D. Keynote Address to the National Science Teachers Association, Seattle, Wa. 1989.

3. Kalhammer, F. R.; Kozawa, A.; Moyer, C. B.; Owens B. B. *Interface* **1996**, *Spring*, 32.

4. Gray, F. M. *Solid Polymer Electrolytes* VCH: New York, 1991; ch 1.

5. Laidler, K. J.; Mieser, J. H. *Physical Chemistry* Benjamin/Cummings: Menlo Park, 1982; p 314.

6. West, A. R. *Solid State Chemistry* John Wiley & Sons: New York, 1984; p. 284.

7. Streitwiser, A.; Heathcock, C. H. *Introduction to Organic Chemistry 2nd Ed.*; Macmillan: New York, 1981; p. 260.

8. Gauthier, M.; Belanger, A; Kapfer, B.; Vassort, G.; Armand, M. In *Polymer Electrolyte Reviews-2* MacCallum, J. R.; Vincent, C. A. Eds. Elsevier: New York, 1989; p. 285.

9. Yamamoto, O. in *Solid State Electrochemistry* Bruce, P. G. Ed.; Cambridge, New York, 1995; ch. 11.

10. Gray, F. M. *Solid Polymer Electrolytes* VCH: New York, 1991; p.13.

11. Yata, S. et al., *Synth. Met.* **1994**, *62*, 153.

12. Guerard, D.; Herold, A. *Carbon* **1975**, *13*, 337.

13. Shu, Z. X.; McMillan, R. S.; Murray, J. J. *J. Electrochem. Soc.* **1993**, *140*, 922.

14. Dahn, J.R.; Zheng, T.; Liu, Y.; Xue, J.S. *Science* **1995**, *270*, 590.

15. Namilova, V.A.; Guerard, D.; Lelaurain, M.; Fateev, O. *Carbon*, in press.

16. Zheng, T. et al. *J. Electrochem. Soc.* **1995**, *142*, 1281.

17. Gopalakrishnan, J. *Chem. Mater.* **1995**, *7*, 1265.

18. Thackeray, M. M. *Proceedings of The Electrochemical Society* **1994**, *94-28*, 233.

19. Mizushima, K.; Jones, P. C.; Wiseman, P. J.; Goodenough, J. B. *Mat. Res. Bull.* **1980**, *15*, 783.

20. Magaura, T. *Prog. Batt. And Batt. Mater.* **1991**, *10*, 209.

21. Ohzuku, T.; Ueda, A.; Nagayama, M. *J. Electrochem. Soc.* **1993**, *140*, 1862.

22. Ohzuku, T.; Ueda, A.; Nagayama, M.; Komori, H. *Electrochim. Acta* **1993**, *28*, 1159.

23. Li, W.; Reimers, J. N.; Dahn, J. R.; *Solid State Ionics* **1994**, in press.

24. Rossouw, M. H.; Liles, D. C.; Thackeray, M. M. *J. Solid State Chem.* **1993**, *104*, 464.

25. Scosati, B. in *Electrochemistry of Novel Materials* Lipkowski, J.; Ross, P. N. Ed.s; VCH: New York, 1994; ch. 3.

26. Thackeray, M. M.; de Kock, A.; Rossouw, M. H.; Liles, D. C.; Hoge, D.; Bittihn, R.; *J. Electrochem. Soc.* **1992**, *139*, 363.

27. Colbow, K. M.; Dahn, J. R.; Haering, R. R. *J. Power Sources* **1989**, *26*, 397.

28. Rossen, E; Reimers, J. M.; Dahn, J. R. *Solid State Ionics* **1993**, *62*, 53.

29. Gummow, R. J.; de Kock, A.; Thackeray, M. M. *Solid State Ionics* **1994**, *69*, 59.

30. Le, D. B.; Passerini, S.; Chu, X.; Chang, D.; Owens, B. B.; Smyrl, W. H. *Proceedings of The Electrochemical Society* **1994**, *94-28*, 306.

31. Park, H. K.; Smyrl, W. H. *J. Electrochem. Soc.* **1994**, *141*, L25.

32. Fauteux, D. *Proceedings of The Electrochemical Society* **1994**, *94-28*, 379.

33. Armand, M.; Sanchez, J. Y.; Gauthier, M.; Choquette, Y. In *Electrochemistry of Novel Materials* Lipkowski, J.; Ross, P. N. Ed.s; VCH: New York, 1994; ch. 2.

34. Reimers, J. N.; Fuller, E. W.; Rossen, E.; Dahn, J. R. *J. Electrochem. Soc.* **1993**, *140*, 3396.

35. Shodai, T.; Sakurai, Y.; Okada, S. *Proceedings of The Electrochemical Society* **1994**, *94-28*, 224.

36. Thakeray, M. M.; David, W. I. F.; Goodenough, J. B. *Mat. Res. Bull.* **1982**, *17*, 785.

37. Liu, W.; Farrington, G. C.; Chaput, F.; Dunn, B. *J. Electrochem. Soc.* **1996**, *143*, 897.

Polymer Electrolytes

Chapter 2

2.0 **Introduction.**

To provide a foundation, and context for the investigative work in Chapters 4-6 the following aspects of PEs are introduced: ion solvation and conductivity in PEs, a broad description of polymers and salts investigated for PEs, crosslinked polyethers as mechanically stable electrolyte films, PE/electrode interfacial models, as well as research progress toward conductive, and robust anode/PE interfaces.

2.1 **Solvation of Ions by Polymers.**

Considering the Second Law of Thermodynamics, $\Delta G = \Delta H - T\Delta S$, the polymer (solvent) and salt (solute) interactions responsible for electrolyte formation can be subdivided into entropic and enthalpic contributions. Solution formation between a solvent and an ionic solid requires the solvent-ion interactions to overcome the lattice energy of the salt, $+\Delta H_L$. In the case of polyalkyl ethers, such as polyethylene oxide (PEO), the solvation energy, $-\Delta H_S$, results from coordinate bonds formed in Lewis acid-base interactions between etheric oxygen lone pairs and salt cations. Another positive enthalpic term, $+\Delta H_P$, represents the energy required to break polymer-polymer attractions, and create a polymer-solute interaction site. The value of $+\Delta H_P$ is generally smaller than $+\Delta H_L$ and varies with polymer type. Finally, these low dielectric polymers do not

completely solvate salts into single ions, therefore, ion aggregates may exist, and the values of ΔH_L and ΔH_S may be decreased [1].

In liquid solvents, the entropy of solvation is positive, and is influenced by the transition from crystalline to solvated ions. In contrast, PE formation is accompanied by a decrease in entropy, and consists of contributions from the polymer ΔS_P, and the salt ΔS_S. The polymer configurational entropy, S_P, decreases because of increased order upon PE formation, which occurs from intra and interchain crosslinks between polymers in coordination with cations. Even though the physical change from a crystalline salt to solvated salt is represented by a positive ΔS_S, it is generally not greater in magnitude than ΔS_P [1].

The positive values of $-T\Delta S$ describing the process of PE formation are realized in the observation of salt precipitation from the electrolyte system PEM-$Ca(CF_3SO_2)_2$ upon heating, and the well known lower solubility of PEO in water as the temperature is increased [2].

Salt solubility can be increased by using higher dielectric polymers containing polar groups such as hydroxyl; however, this needs to be balanced with the electrochemical stability of these groups, for example, the lability of the O-H bond may lead to unwanted electrode reactions, or depolymerization under high polarization [3].

The structure surrounding ions solvated in polymer solvents has been addressed using a number of techniques including X-ray crystallography, NMR, and Raman spectroscopy. The amorphous phase is not directly observed with diffraction techniques, nonetheless, the description of crystalline PEs can provide insight into the polymer-salt

interactions that may exist in this phase. The crystal structures of some $PEO(MA)_x$ electrolytes have been described where M= Li^+, Na^+, K^+, Rb^+, and A= SCN^-, ClO_4^-, $CF_3SO_3^-$. The cations, in coordination with ether oxygens, have lone pair coordination numbers of 5 for Li^+, 4 for Na^+, 7 for K^+ and Rb^+ [4-6]. Pulse field gradient ^{27}Na NMR (PFG-NMR) demonstrates the existence of two types of cations that differ in mobility, such cations may be free, bound, single, or aggregated [7]. Vibrational frequencies around 860-870 cm^{-1} are observed in the IR Raman spectra of various PEs, and suggest the existence of cation-ether oxygen solvation, and show evidence of ion aggregation especially at increased temperature [8].

2.2 **Electrolyte Salts.**

Salts that dissolve to form PEs with low dielectric polymers, such as PEO, are characterized by low lattice energies. Shriver *et al.* report a maximum ΔH_L of 850 kJ/mol for salt solubility into PEO [9]. Large nonmetal polyatomic anions such as ClO_4^-, $CF_3SO_3^-$, BF_4^-, AsF_6^-, or $(CF_3SO_2)_2N^-$ form low lattice energy salts with lithium ions, and are therefore used as electrolyte salts. Generally, low t_+ values (cation transference) limit the utility of these salts, and specifically, the potentially explosive nature of perchlorate makes it unattractive. Efforts to synthesize other conductive, low lattice energy salts have produced long-chain fluoroalkylsulfonylimide or fluoroalkylsulfonylmethide lithium salts with soft anion centers containing N or C. Strong covalent bonds in these anions contribute to their oxidation resistance, and the extremely large anionic size may contribute to their low mobility, and high t_+ values [10]. Also, they demonstrate a

(a)

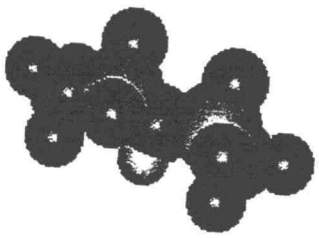

(b)

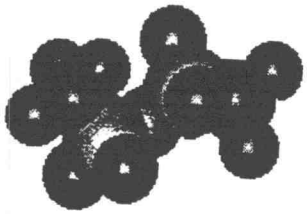

(c)

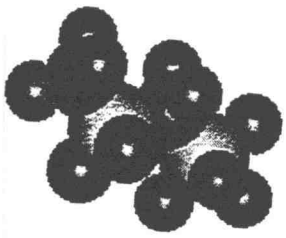

Figure 2.1. Large anions with delocalized negative charge. R=H, alkyl, acyl, CF_3SO_2 [3]. (a) Trifluoromethanesulfonimide (TFSI), (b) Trifluoromethanesulfonylmethide (TFSM), and (c) pentafluorothiodifluoromethane sulfonate. Other electrolyte salt anions include ClO_4^-, AsF_5^-, PF_5^-.

plasticizing effect on semicrystalline polyethers, increasing their room temperature conductivities. Examples of these salts are shown in Figure 2.1 [10].

2.3 **Conductivity.**

Ionic conduction in any media can be described with the following relationship:

$$\sigma = \Sigma_i \, n_i e_i \mu_i \tag{2.1}$$

Where σ is conductivity, n is the number of charge carriers, e is their charge, and μ is the mobility of the charge carrier. To conduct in a crystalline solid, ions must gain kinetic energy from a thermal source and/or an applied electric field in order to overcome a translational energy barrier; when this occurs, the ion quickly moves (hops) from one site to another where the process repeats. The exponential relationship between conductivity and inverse temperature is described in the Arrhenius equation:

$$\sigma = Ae^{-\frac{E_a}{k_b T}} \tag{2.2}$$

Where E_a is the activation energy required to surmount the internal energy barrier and A is related to the number of charge carriers within the sample [11].

PEs typically demonstrate a gently sloping curve when the log of conductivity is plotted against reciprocal absolute temperature; such a deviation from Arrhenius theory requires an alternate model to describe conductivity in PEs. The ionic conductivity of a

PE may depend upon macromolecular properties of the polymer host, and not upon simple activation theory outlined above for crystalline solids.

The Vogel-Tamman-Fulcher (VTF) equation describes the characteristic conductivity-inverse temperature relationship observed in PEs. It is descriptive in nature, and uses the equilibrium glass transition temperature, T_0 , which denotes the thermodynamic onset of long range polymeric motion, and pseudo activation energy (B) as fitting parameters.

$$\sigma = Ae^{-\frac{B}{k_b(T-T_0)}} \tag{2.3}$$

This relation can be derived from a free volume model [12, 13], in which voids occur within the polymer matrix at a thermal energy coinciding with the equilibrium glass transition temperature T_0, (T_0=T_g-50). The observed glass transition, T_g, occurs when the void (or free-volume) concentration can accommodate long-range polymer gyrations; T_g is the temperature at which long-range macromolecular motion occurs (for this motion to occur, a void space is needed for the chains to move into). An association, therefore, exists between polymer mobility and ionic conductivity, in which amorphous PEs well above T_g have higher ionic conductivity than their semicrystalline, or glassy counterparts. These flexible polymers may break and reform the coordination sphere of an ion, allowing its conduction in an electric field. Polymers with strong interchain interactions, or rigid backbones with conjugated pi-bonds, have limited segmental flexibility and ionic

conduction. Low T_g, amorphous polymers with flexible backbones, therefore, are attractive electrolyte materials [14].

The same ion-polymer, ion-ion, and polymer-polymer interactions governing solubility of salts in polymers also affect conductivity. In these electrolytes, charge carrier concentration increases with salt content, and the presence of significant ion-polymer interactions decreases the configurational entropy of polymer chains, which, in turn, decreases conductivity. These effects are demonstrated by increased PE glass transition temperatures over the pure polymer [10]. Finally, the probability of ion aggregation increases with salt concentration, which is not desirable because the large size of these aggregates may inhibit their mobility [15-18].

Ion-polymer interactions have been observed with PFG-NMR, and INVREC. These indicate the presence of both mobile and bound cations in the PE matrix [7]. Ion-ion interactions have been observed within polyelectrolytes, in which the anion is covalently bound to the polymer, which conducts only cations. The addition of a cation solvent such as cryptand releases cations from their bound (to the polymer) state, and causes a 10-fold increase in conductivity [19].

2.4 **Polymers for Polymer Electrolytes.**

Polymers investigated for use as PEs contain three general types of functional units: etheric, imine, and thioetheric. Polyethylene oxide (PEO) is the prototypical polymer investigated as a PE. The low cost, and safety of PEO make it attractive for use. The two-carbon spacing between coordinating groups allows for favorable coordination

orientation, contributing to the success of PEO as a solvent. In contrast, the backbone of poly(methylene oxide), (PMO), $(CH_2O)_n$ is too rigid; and neither PMO nor poly(trimethylene oxide) $(CH_2CH_2CH_2O)$ can attain low energy conformations to maximize cation coordination [3]. Poly(propylene oxide) (PPO) is a solvent; however, the electrolyte concentrations attained are lower than the analogous PEO systems because of the steric hindrance created by atactic methyl groups. The coordination ability of the nitrogen heteroatom in polyethylene imine is stronger than ether in PEO due to its stronger Lewis base character, but these electrolytes have lower conductivities than their analogous PEO electrolytes [20]. Poly(alkylene sulfides) are observed to form electrolytes with soft-cation salts like silver, and are not effective lithium salt solvents [21].

At room temperature, PEO (above M_w 1500D) is a semicrystalline elastomer with a glass transition temperature (T_g) of -65°C and melting point (T_m) of 65°C. The melting temperatures of its PEs are close to 65°C; however, Li(imide) salts display lower melting PEs [10]. Because conductivity increases above the melting temperature, and applications may require high conductivity (10^{-4}-10^{-3} Scm^{-1}), PEO electrolyte cells operate well above room temperature (100° C). Work toward low T_g, and T_m PEs has produced both inorganic, and organic-backbone amorphous polymers, of which a few examples are shown in Figure 2.2, and discussed below.

Within elastomeric PEO and its electrolytes, the crystalline fraction consists of ethoxy monomers arranged into helical units [22]. Reduced melting points are achieved by inhibiting the ability the polymer to form crystallites, which is accomplished by disrupting the repetition of ethoxy units in the backbone. These polymers may be synthesized by

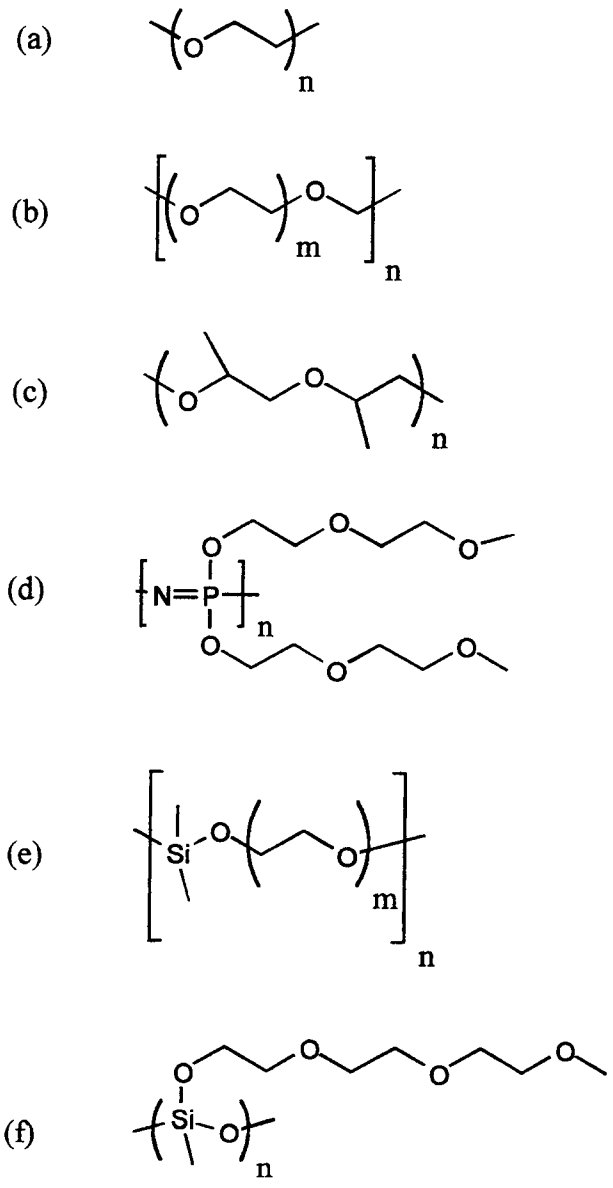

Figure 2.2. Some low T_g, T_m PE candidates: (a) polyethylene oxide (PEO), (b) poly[oxymethylene oligo-oxyethylene] (PEM), (c) atactic polyproylene oxide (PPO), (d) poly[bis-(methoxy ethoxy ethoxy)phosphazene] (MEEP), (e) poly[dimethylsiloxyl oligo-oxyethylene], and (f) poly{[ω-methoxyoligo-(oxyethylene)ethoxy]methoxy siloxane} (PMMS).

statistical polymerization of oligo-oxyethylene with a difunctional linking agent, L, such that the polymer $[(CH_2CH_2O)_m\text{-}L]_n$ is produced. Some possibilities of L include, urethane, carbonate, siloxane [27], phosphate or oxymethylene [23]. Poly[oxymethylene oligo-oxyethylene] (PEM) is an oxymethylene linked polymer, with formula: $[(CH_2CH_2O)_m(CH_2O)]_n$ where m = 8.7 and n ≈ 1,000, which produces $M_w \sim 1 \times 10^5$ D [24, 25].

PEM is synthesized from a condensation reaction between methylene chloride and PEG [24, 25], or from the ring opening polymerization of trioxane and dioxolane [26]. The condensation reaction may produce polymers with average molar masses of about 1×10^5 D, whereas the later reaction produces a viscous product with a low average molar mass of around 23,000 D. The condensation synthesis takes place in two steps: first, the formation of chloroether from methylene chloride and PEG:

$$CH_2Cl_2 + H(OCH_2CH_2)_{8\text{-}10}OH \rightarrow H(OCH_2CH_2)_{8\text{-}10}OCH_2Cl + HCl \qquad (2.4)$$

which is followed by a rapid reaction between the chloroether and PEG.

$$H(OCH_2CH_2)_{8\text{-}10}OCH_2Cl + H(OCH_2CH_2)_{8\text{-}10}OH \rightarrow$$

$$[H(OCH_2CH_2)_{8\text{-}10}O]_2CH_2 + HCl \qquad (2.5)$$

Increasing the molecular weight of PEG used in the reaction augments the number of ethoxy repeats between methoxy linkages. Use of PEG 200, PEG 400, and PEG 600 produces PEM with T_m's of -9°C, 10°C, and 26°C respectively; the limit as PEG weight increases should approach the T_m of PEO (65°C).

Polymers containing backbones comprising flexible inorganic moieties, such as siloxy $(Si\text{-}O)_n$ or phosphazene $(N{\equiv}P)_n$, typically, have low glass transition temperatures and low melting points [28-31]. Ethoxy oligomers graphed onto the inorganic backbone produce comblike polymers, these include (Figure 2.2): poly[bis-(methoxy ethoxy ethoxy phosphazene)](MEEP), and poly{[ω-methoxyoligo-(oxyethylene)ethoxy]methoylsiloxane} (PMMS). The T_g of MEEP is -84°C, and PMMS is -123° C (PEO= -65° C), they are completely amorphous at room temperature. While an inorganic backbone does not contribute directly to coordination chemistry, it increases the mobility of the ethoxy units, and produces high room temperature ionic conductivity.

Amorphous character in a polymer electrolyte may enhance the ionic conductivity; however, such polymers are without mechanically stability. Under prolonged application of force (ie. gravity, or stack pressure in a battery) they will flow. In order for PEs to be practical, they must maintain separation between electrodes when processed into films of ~25 μm thickness. In order to increase the mechanical stability of conductive, amorphous polymers, crosslinks can be introduced within the system without a large decrease in conductivity.

2.5 **Networked Polyethers.**

There are two general methods employed to introduce crosslinks or branch sites into polyethers: the synthesis of gelled or networked samples from smaller components, or the exposure of a linear polymer to ionizing radiation. A linear polymer that has some degree of crosslinks introduced has an increase the mechanical stability. These sites

distribute external force, and can change a viscous material into an elastic one with a sufficient concentration [32]. In addition, these sites can dampen long range motion of polymer chains without affecting their local motion, so that a mechanically stable sample will not flow, and have the ionic conductivity of a linear PE. A minimum distance between crosslink sites can be determined in which sufficient conductivity and mechanical stability can be provided [33].

Such an optimal crosslink density leaves enough linear weight between crosslinks (***D***) to maintain ionic conductivity for a given electrolyte concentration [33]. If the PE is an amorphous polymer such as PEM, the limiting distance between crosslinks can be much greater. The ***D*** value in crosslinked, conductive PEO based PEs is close to 1500 D (the upper limit for room temperature liquid PEO). Because PEs can have lower melting temperatures than the pure polymer, the actual limiting weight between crosslinks is greater than 1500 D, and has been suggested to be $\boldsymbol{D} = n \times 1000$, where $2n - 1$ lithium ions are solvated per ethoxy oligomer [33].

2.5.1 **Gelled PEM**.

Polymers produced in a condensation reaction incur elimination of a small molecule (H_2O) for each linkage created, this process is illustrated for the polyether synthesis below:

$$nR(OH)_2 + nR'Cl_2 + 2nKOH \rightarrow [-ROR'O-]_n + 2nH_2O + 2nKCl \qquad (2.6)$$

Where the bifunctional reactants are a diol, such as polyethylene glycol, or dichloromethane, and water is the condensate. Branched polymers are produced from the reaction above with an admixture of trifunctional alcohol ($R(OH)_f$, f = 3). Alternatively, tetra functional species (f = 4) can be introduced into the reaction mixture, producing crosslink sites. Statistically, the quantity, *d*, of R"$(OH)_f$ (f = 3, 4) admixed to the reaction is evaluated to produce a networked polymer where one branch/crosslink site always leads to another [34].

$$dR''(OH)_f + nR(OH)_2 + nR'Cl_2 + 2nKOH \rightarrow$$
$$gelled[-ROR'O-]_n + 2nH_2O + 2nKCl \qquad (2.7)$$

The quantity of crosslinking/branching agent in the reaction is small, therefore, the sites are not shown in the formula of the product, and the product is referred to as *gelled.*

Crosslinked PEM can be synthesized with an admixture of polyfunctional alcohol ($R(OH)_{3,4}$) to the reaction of CH_2Cl_2 and PEG 400. The resulting product has long chains of amorphous polymer between crosslink sites. The polyfunctional alcohols make crosslinks in either of the reaction steps outlined previously. Pand *et al.* used glycerol: $CH_2(OH)CH(OH)CH_2(OH)$, TMP: $CH_3CH_2C(CH_2OH)_3$, and pentaerithytol: $C(CH_2OH)_4$ as crosslinking and branching agents. The high molecular weight branched systems produced were observed to dissolve in water for gel permeation chromatographic (GPC)

analysis, indicating low levels of crosslinking (< 1%). The use of pentaerithrytol resulted in a polymer of $M_W = 1.2\times10^6$D, whereas, the linear polymer (from a control experiment) had $M_W = 3.7\times10^5$ D [35].

Mechanical analyses of these crosslinked PEMs demonstrate an increase in modulus with molecular weight; however, a sharp decrease in modulus occurred for each sample at 10° C in correspondence with the melting point of PEM, indicating that these networked polymers melt at a similar temperature, and that the liquid phase experiences a decrease in mechanical stability. The PEs from the crosslinked or branched polymers demonstrate similar ionic conductivities as the linear PE [35].

2.5.2 **Urethane Crosslinked Polymers**.

Polyethers can be crosslinked with isocyanate (urethane) moieties. Copolymeric PEO-PPO crosslinked with isocyanate has been produced on an industrial scale as urethane foam. This crosslinking agent has been utilized in the development of polyether networks for electrolytes, an example of urethane crossslinked PEO chains is given in Figure 2.3 [36].

Watanabe *et al.* compared characteristics of crosslinked block-copolymers of polypropylene oxide/polyurethane urea (PPO/PUU) with long, and short PPO segments of 3000 D and 2000 D respectively. The log of conductivity of the crosslinked samples with the longer segments was -6.6 S cm^{-1} (and -7 S cm^{-1} for the sample with shorter segments), these data relate with the lower glass transition temperature of the short segment products [37].

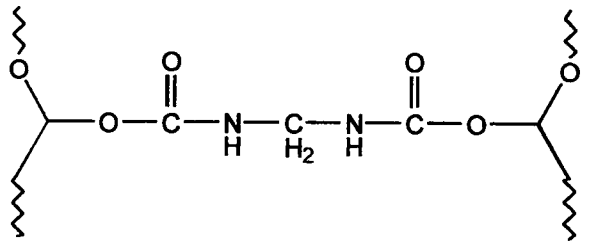

Figure 2.3. Isocyanate crosslinked PEO, the polymer is implied on the left and right sides of the diagram.

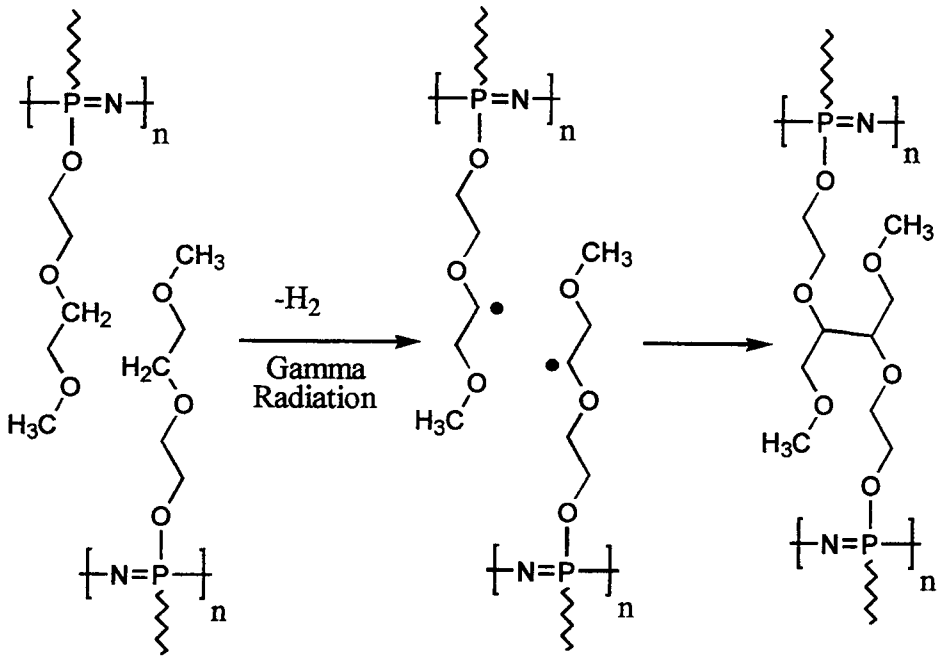

Reaction Scheme 2.1. The reaction proposed for gamma radiation crosslinking of MEEP.

2.5.3 Radiation Crosslinked Polymer Electrolytes.

PEO and MEEP have been crosslinked by exposure to gamma radiation. The reaction is displayed for MEEP in Reaction Scheme 2.1. [38] An investigation of the gamma irradiated PEO films reports upon the formation of mechanically stable, conductive systems [39]. The high energy gamma rays are capable of cleaving C-H bonds, and leaving carbon radicals that further react to produce crosslink sites along with $H_{2(g)}$.

MEEP has also been crosslinked by exposure to ultraviolet radiation in the presence of photoinitiators. The resulting crosslinked product swells in water without dissolving, indicating that it contains a concentration of crosslink sites of at least 1% [40].

Gelled polymers may be more difficult to process into thin films than linear polymers, therefore, radiation methods may be a more attractive technique because existing films can be crosslinked. Examples of crosslinking films of polyethers will be introduced in Chapters 4 and 5.

2.6 Electrode/Electrolyte Interfaces.

A high energy density battery must have efficient charge transfer from one electrode to another across an electrolyte. Loss in ion transfer may occur if the electrolyte (with its components and impurities) reacts with active lithium to produce a passive layer between lithium metal and the electrolyte, which results in lower conductance at the electrode/PE interfacial region. The additional resistive, interfacial layer impedes lithium ion conduction during cell charge or discharge, an added *i*R drop across the cell results, and decreases the cell voltage (and therefore, the potential to perform work). While this

discussion focuses on the lithium metal /PE interface, similar characteristics may describe a cathode (transition metal chalogenide)/ PE interface [41, 42].

Generally, there are two types of electrode/electrolyte interfaces that occur against lithium: a porous electrolyte interface (PEI), or a solid electrolyte interface (SEI). The composition, morphology, and characteristics of the interface depend on the nature of the electrolyte, and cell operating conditions [41].

A PEI is composed of a polymeric layer developed onto an electrode surface as the result of an interfacial reaction between the electrolyte and the electrode. This interface can be thought of as a completely passive, electronic and ionic insulator; however, ionic conductivity can occur through pores, if their size accommodates solvent molecules and ions. As θ, the fraction of the electrode surface covered by the PEI increases, cation access to the electrode is inhibited, and the cell conductivity drops. Ionic conduction across the layer is limited to areas free of the PEI. The PEI system is demonstrated within some liquid electrolyte/Li interfaces, and can be seen in electrolyte/electrode systems such as in organic electrolyte/Pt interfaces [41, 42].

A solid electrolyte interface (SEI) may exist at the junction between electrode and electrolyte. The mode of conductivity, electronic or ionic, and composition-morphology are not well understood; however, ionic conduction is expected, and some clues, from impedance analysis, exist as to its structure [43]. The conductivity of an SEI has characteristics of some known ionic conducting crystalline solids. Both display Arrhenius behavior over a wide temperature range, and behave similarly under changing electric field

strengths (discussed below). An SEI, therefore, is thought to be a solid ionic conductor with a cationic transference number of unity ($t_+=1$) [41].

In solid cationic conductors, charge carriers conduct in a hopping mechanism from one potential-well to another, while maintaining overall charge balance within the solid. These potential-wells can be either interstitial, or crystal defect sites within the solid. Young demonstrated that a SEI behaves like a solid cationic conductor. The current density within the SEI follows the direction and magnitude of the applied electric field, and an exponential relationship exists between current density and electric field for strong fields. Along the direction of a weak field, the current density is about the same as that against the field, indicating that ions are not accelerated enough to overcome the potential barrier for conduction [44].

As a result of SEI formation, one interface essentially becomes two: the SEI/Li, and the SEI/PE interfaces. This separates the anode and the electrolyte, adds to the cell resistance, and may contribute to dendrite growth. Irregularities and nonuniformity within this layer form regions where lithium metal deposition may be dendritic, and lead to cell failure [45].

Some SEI characteristics can be observed with ac impedance spectroscopy (discussed in Chapter 3.). Growth of the layer is observed through the increase of interfacial resistance over time. At constant temperature, the layer grows exponentially and then stabilizes after a few hours; the process repeats when the cell is heated [41]. Between the initial PE/electrode contact and SEI stabilization, two processes occur: both the coverage (θ) of the electrode, and the SEI thickness increase. Low viscosity liquid

electrolytes and copolymerized or plasticized PEs achieve complete coverage of the electrode surface; however, coverage with a solid, high a molecular weight polymer is incomplete, and voids may be present at the interface. Impedance analyses of a surface composed of adsorbed PE reveal that they have lower interfacial capacitances than interfaces composed of voids [43].

The SEI composition can, therefore, be described as a conglomeration of particles and voids. The composition of the particles may be a function of the electrolyte salt, and the presence of impurities (H_2O, R-OH, catalysts) in the PE [46], although, very pure PEs also show SEI formation [42]. In the heterogeneous mass that makes up the SEI, lithium ion conduction probably occurs near particle surfaces in a hopping mechanism from void to void. Increased disorder of the SEI may reduce interfacial coverage and result in a relatively conductive interface. With this hypothesis in mind, the addition of ceramic particles to the PE was observed to decrease interfacial impedance; similarly, lithium ion conducting aluminum oxides mixed with PE demonstrate a stable, conductive anode interface in cells up to 120°C [47].

2.7 **Methods of Controlling the SEI.**

Two general approaches have been taken in order to minimize of the detrimental effects of SEI formation: passivation of the anode prior to cell construction (pre-passivation), or alteration of the PE composition with additives.

In pre-passivation, a thin layer of an organic polymer is applied to the electrode, producing an ionically conductive coating, under controlled conditions. Upon cell

construction and use, the preformed interface should prevent further SEI growth. This strategy was investigated by Fauteux, where a LiAl alloy was treated with a 2:1 mixture of 2-vinyl naphthalene/dioxane mixture using a plasma polymerization process; the subsequent cells were constructed with either a liquid electrolyte (propylene carbonate) or a PE, ($PEO_{20}LiCF_3SO_3$). In both cases, the interfacial impedance changed very little over time, indicating the presence of a completely formed, chemically inert, SEI prior to cell construction [48].

The pre-passivated interface may best be described as having both polymeric, and crystalline ionic conduction mechanisms. This interface demonstrated Arrhenius behavior consistent with a solid ionic conductor; however, higher conductivity is demonstrated by interfaces with etheric-based copolymers rather than the aliphatic-based polymers. The ease of segmental motion in etheric networks over pi-bonded aliphatic polymers may account for the high interfacial conductivity. Naphthalene interacts with lithium to form free-radical anion complexes at a potential of 0.3V vs. Li/Li^+(Figure 2.4). These anions may reduce dendrite growth through electric field homogenization across the metal electrode surface [45].

As noted, increasing the disorder within the SEI is expected to enhance ion transfer across the interface, and workers continue to use ceramic additives to attain this end. Scrosati reported the mixture of ceramic and PE: $(PEO)_8Li[(CF_3SO_2)_2N]$-γ-$LiAlO_2$ has a significantly enhanced lithium electrolyte interface over the electrolyte alone [49]. Other PEO electrolyte systems have also demonstrated this effect upon the addition of ceramics, including γ-$LiAlO_2$ and MgO [49]. The particle size utilized in these

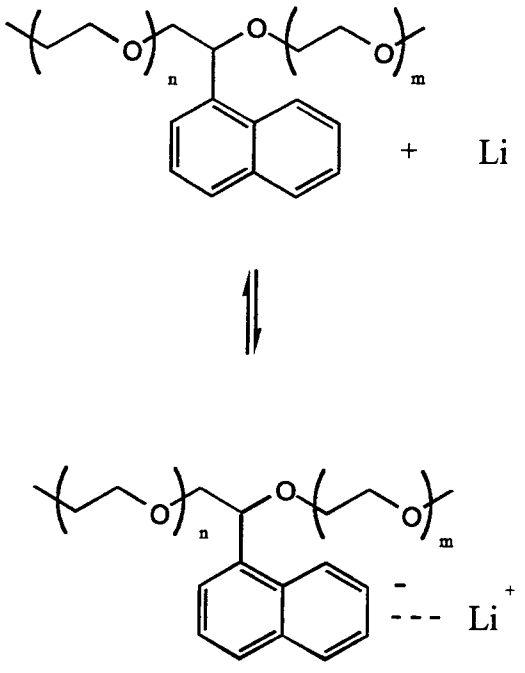

Figure 2.4. The naphthalenic structure of the pre-passivation coat, and the charge-transfer anion that may exist on the lithium metal surface.

investigations was <1μm, and the relationship between particle size and interfacial resistance has not been established; however, each ceramic produced a similar effect. Solid polymer electrolytes with ceramic particles may have low θ values due to the roughness of the electrolyte surface, which would decrease SEI formation [43].

2.8 **References.**

1. Bruce, P. G.; Gray, F. M. in *Solid State Electrochemistry* Bruce, P. G. Ed.; Cambridge: New York, 1995; ch. 6.

2. Mehta, M. A.; Lightfoot, P.; Bruce, P. G. *Chem. Mater.* **1993**, *5*, 1338.

3. Armand, M.; Sanchez, J. Y.; Gauthier, M.; Choquette, Y. In *Electrochemistry of Novel Materials* Lipkowski, J.; Ross, P. N. Ed.s; VCH: New York; 1994, ch. 2.

4. Chatani, Y.; Okamura, S. *Polymer* **1987**, *28*, 1815.

5. Lightfoot, P.; Metha, M. A.; Bruce, P.G. *J. Mater. Chem.* **1992**, *2*, 379.

6. Bruce, P. G. *Electrochim. Acta.* **1995**, *40*, 2077.

7. Lemmon, J. P. PhD Thesis, Oregon State University, 1994.

8. Torell, L. M.; Schantz, S. Polymer *Electrolyte Reveiws-2* Eds Maccallum, J. R. and Vincent, C. A., Elsevier Applied Science, NY, p. 1.

9. Papke, D. L.; Ratner, M. A.; Shriver, D. F. *J. Electrochem. Soc.* **1982**, *129*, 1694.

10. Nafshun, R. L.; Lerner, M. M.; Hamel, N. N.; Nixon, P. G.; Gard, G. L. *J. Electrochem. Soc.* **1995**, *142* , L153.

11. Laidler, K. J.; Mieser, J. H. *Physical Chemistry* Benjamin/Cummings: Menlo Park, 1982; p. 370.

12. Cohen, M. H.; Turnbull, D. *J. Chem. Phys.* **1959**, *31*, 1164.

13. Cohen, M. H.; Grest, G. S. *Phys. Rev. B* **1980**, *B21*, 4113.

14. Ratner, M. A. in *Polymer Electrolyte Reviews-1* MacCallum, J. R.; Vincent, C. A. Ed.s; Elsevier: New York, 1987; ch. 7.

15. Lemmon, J. P.; Lerner, M. M. *Macromolecules* **1992**, *25*, 2907.

16. Nafshun, R. L.; Lerner, M. M., 1995, unpublished results

17. Gray, F.M. in *Polymer Electrolyte Reviews-1* MacCallum, J. R.; Vincent, C. A. Ed.s; Elsevier: New York, 1987; ch. 6.

18. Lonergan, M. C.; Shriver, D. F.; Ratner, M. A. *Electrochim. Acta* **1995**, *40*, 2041.

19. Lonergan, M. C. Ph.D. Thesis Northwestern Universtiy 1994.

20. Harris, C. S.; Shriver, D. F.; Ratner, M A. *Macromolecules* **1986**, *19*, 188.

21. Clancy, S.; Shriver, D. F.; Ochrymowycz, L. A. *Macromolecules* **1986**, *19*, 606.

22. Takahashi, Y.; Takadoro, H. *Macromolecules* **1973**, *6*, 672.

23. Booth, C.; Nicholas, C. V.; Wilson, D. J. *Polymer Electrolyte Reviews-2* Maccallum, J. R. and Vincent, C. A. Eds, Elsevier Applied Science, NY, p. 241.

24. Craven, J. R.; Mobbs, R. H.; Booth, C.; Giles, J. R. M. *Makromol. Chem., Rapid. Commun.* **1986**, *7*, 81.

25. Nicholas, C. V.; Wilson, D. J.; Booth, C.; Giles, J. R. M. *Brit. Polym. J.* **1988**, *20*, 289.

26. Giles, J. R. M.; Booth, C.; Mobbs, R. H. *Proceddings, 6th Risø International Symposium on Metallurgy and Materials Science* Risø National Lab., Roskilde; 1985, p. 329.

27. Nagoka, K., Naruse, K., Naruse, H., Shinohara, I., Watanabe, M. *J. Polym. Sci. Polym. Let.* **22**, *1984*, 659.

28. Nagoka, K., Naruse, K., Naruse, H., Shinohara, I., Watanabe, M. *J. Polym. Sci. Polym. Let.* **22**, *1984*, 659.

29. Blonsky, P. M.; Shriver, D. F.; Austin, P.; Allcock, H. R. *J. Am. Chem. Soc.* **1986**, *106*, 6854.

30. Xia, D. W.; Soltz, K.; Smid, J. *Solid State Ionics* **1984**, *14*, 221.

31. Khan, I. M.; Yuan, Y.; Fish, D.; Wu, E.; Smid, J. *Macromolecules* **1988**, *21*, 2684.

32. Sperling, L. *Introduction to Physical Polymer Science* Wiley & Sons: New York, 1986.

33. Berthier, C.; Gorecki, W.; Miner, M.; Armand, M. B.; Chabagno, J. M.; Rigaud, P. *Solid State Ionics* **1983**, *11*, 91.

34. Flory, P. J. *Principles of Polymer Chemistry* Cornell, UP: Ithica NY, 1953; ch. 3.

35. Pang, Y.; Mai, S-M.; Huang, K-Y.; Luo, Y-Z.; Thatcher, J. H.; Colley, R. A.; Nicholas, C. V.; Booth, C. *J. Mater. Chem.* **1995**, *5*, 831.

36. Killis, A., LeNest, J. F., Cheradame, H.; Gandini, A. *Macromol. Chem.* **1982,** *183*, 2835.

37. Watanabe, M.; Oohashi, S.; Sanui, K.; Ogata, N.; Kobayashi, T.; Ohataki, Z. *Macromolecules* **1985**, *18*, 1945.

38. Allcock, H. R.; Nelson, C. J.; Coggio, W. D. *Proceedings of the American Chemical Society Division of Polymeric Materials: Science and Engineering* **1993**, *68*, 76.

39. MacCallum, J.R., Smith, M.J., Vincent, C.A. *Solid State Ionics* **1984**, *11*, 307.

40. Nelson, C. J.; Coggio, W. D.; Allcock, H. R. *Chem. Mater.* **1991**, *3*, 786.

41. Fautuex, D.; Little, A. *Electrochim. Acta* **1993**, *38*, 1199.

42. Gray, F. *Solid Polymer Electrolytes* VCH, New York; 1991, ch. 10.

43. Peled, E. *Proc. Electrochem. Soc.* **1994**, *94-28*, 1.

44. Young, L. *Anodic Oxide Films* Academic Press: New York, 1961.

45. Fauteux, D. *Proc. Electrochem. Soc.* **1994**, *94-28*, 16.

46. Peled, E. *J. Electrochem. Soc.* **1979**, *126*, 2047.

47. Peled, E.; Golodnitsky, D.; Ardel, G.; Eshkenazy, V. *Electrochim. Acta* In Press.

48. Takahara, Z.; Ogumi, Z.; Kanamura, K.; Uchimoto, Y. *The Electrochemical Society Fall Meeting*, New Orleans, Louisiana, Oct. 10-15, 1993, extended abstract no. 4.

49. Boroghini, M. C.; Mastragostino, M.; Passerini, S.; Scosati, B. *J. Electrochem. Soc.* **1995**, *142*, 2118.

Chapter 3

Experimental

3.0 PEM Synthesis and Characterization.

PEM was synthesized via a Williamson condensation reaction [1-3], in which alcohols and halogenated hydrocarbons combine to produce ethers. The product was methoxy-linked polyethylene glycol (PEG 400) with 8 or 9 ethoxy units per oxymethylene linkage: $HO[(CH_2CH_2)_{8.7}(CH_2O)]_nH$.

3.0.1 PEM Synthesis.

Under an inert atmosphere, to avoid water uptake, an electric coffee grinder was used to produce 50 g of powdered KOH (Aldrich, reagent grade). After loading KOH into a three-necked-reaction flask, it was capped with a septum, an electric stir motor and condenser were attached, and the apparatus was placed into an ice-bath and purged with nitrogen. Afterward, 50 mL of dry methylene chloride (Mallinkrodt, spectroscopic grade) was added and allowed to stir. Dry PEG400 (Aldrich, reagent grade) was added via a syringe (through a large gauge needle) to the stirring vessel, the reaction proceeded for about 15min and turned into a viscous, rubbery mass. After about 30 min, another 50 mL of methylene chloride was added via a syringe, and the reaction continued overnight. All subsequent manipulations were in air, unless noted otherwise.

The mass of PEM, KCl, H_2O, KOH, PEG, and methylene chloride present after the reaction was cut into pieces using a wire worked into the flask. The polymer was dialyzed

(Dialysis, 10,000 D porosity) against deionized water for ten days (or until the solution reached pH~7). Afterward, the aqueous polymer solution was dried with a rotovap. Bumping was an initial problem, and the process required observation until it subsided at about 50°C. Final drying was performed in a Teflon cup enclosed in a drying tube (Figure 3.1) *in vacuo* at 70°C for 24 h; the product was a transparent, amber polymer.

3.0.2 **PEM Characterization.**

A PEM average molecular weight, M_W=7.5×10^4 D, was determined using gel permeation chromatography (GPC). Linear Hydrogel columns were used (Waters, linear ultra hydrogel 6-13μm) with a filtering pre-column attachment for protection from large particles, and a mobile phase of millipore filtered water to separate water soluble polymers as a function of molecular weight. The mobile phase contained 0.01 M NaN_3 to suppress biological growth. All of the samples had concentrations no larger than 0.2 wt.%. The calibration of GPC columns was accomplished with analysis of monodisperse (M_W / M_N≈1) PEO standards (Poly Standards), and a linear plot was obtained for Log(1/M_W) vs. elution volume.

The statistical copolymeric composition, and structure of the product were determined using proton ^{1}H, or carbon ^{13}C nuclear magnetic resonance spectroscopy (NMR). About 10-15 mg of sample was dissolved in an NMR tube with about 2.5 mL of $CDCl_3$, or D_2O (Cambridge). Utilizing a Bruker 300 MHz instrument, the sample was exposed to a 70,500 Gauss magnetic field, and then the response signal was analyzed from 32 (for proton), or 300, (for carbon) pulses and manipulated.

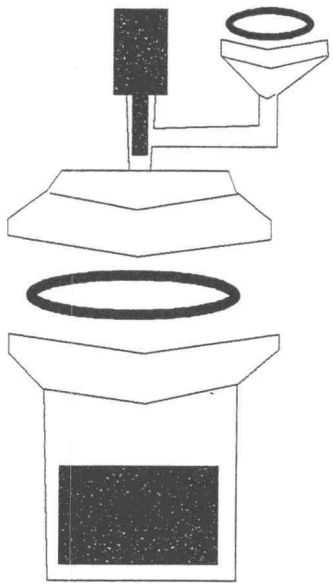

Figure 3.1. The drying tube has a Teflon stopcock on top so that the contents can be sealed in a vacuum, or under an inert gas. A neoprene o-rings seal the system when clamped between the glass joints.

A differential scanning calorimeter (Shimadzu DSC-50Q) was used to identify thermal events of glass transition temperature T_g and melting temperature T_m's. Two hermetically sealed aluminum pans were placed in the enclosed heating unit, one contained 40 mg of the sample, and the other was empty. A heating rate of 10° C/min was usually employed. Thermograms were recorded as energy change vs. temperature, in which positive peaks corresponded with exothermic events, and negative peaks represented endothermic events. T_g's were recorded at the inflection point of the typical "s" shaped curve. Melting temperatures were recorded at the intersection of the baseline with the positive peak slope.

3.1 **Crosslinking PEO and PEM with UV Radiation.**

PEO ($M_w = 5\times10^6$ D; Aldrich), or PEM ($M_w = 7.5\times10^4$ D) was dissolved in acetonitrile (Mallinkrodt, spectroscopic grade), and a viscous solution (PEO: 1 g / 20 mL and PEM: 1 g / 10 mL) was cast onto Teflon matting and dried in air. The polymer was cut into disks about 0.4 mm thick and further dried at 60° C *in vacuo* for 12 h, or disks were formed in glass rings and similarly dried. Disks containing benzopheneone (Spectrum, reagent grade) as a photoinitiator were also prepared. PEO solutions with benzophenone were handled under red light to avoid polymer scission, and disks were stored in the dark. PEM samples containing benzophenone were not noticeably degraded under ambient light. Following irradiation, benzophenone and low molecular weight by-products were removed by washing in acetone (Mallinkrodt, Spectroscopic).

Disks were sealed in 1 in. diameter quartz tube and placed into a Rayonet rotating UV reactor fitted with Hg vapor tubes (254 nm, 110 V AC outlet). Irradiation times varied from 5 min to 60 h. Samples were rotated to promote even exposure.

Irradiated discs swelled isotropically in deionized water, relative to the extent of crosslinking. The Flory-Rehner equation was employed to derive a value for crosslink density [4]:

$$n = -[\ln(1 - v_2) + v_2 + \chi v_2^2] \; / \; V_1[v_2^{1/3} - v_2/2] \qquad (3.1)$$

Where n is the crosslink density (mol / mL), v_2 is the volume ratio of an unswollen to a swollen polymer, V_1 is the molar volume of the solvent (mL / mol), χ is the polymer-solvent interaction parameter, and has a value of 0.45 for PEO/water solutions [5]. This value has been used to describe other PEO crosslinked systems [5]. Samples were evaluated as percent crosslinked, which refers to the number of crosslinks present per 100 ethoxy units in the polymer sample.

3.2 **Preparation of Polymer Electrolytes.**

PEM-salt electrolytes were prepared with a stoichiometry of etheric oxygen to lithium ratio of $O:Li^+ = 25:1$ (or 15:1 for PEO) by co-dissolution or salt imbibition (for the crosslinked polymers) from a solution of $LiClO_4$ (Aldrich reagent, dried *in vacuo* at 200° C for several days) in CH_3CN (distilled from CaH_2). The resulting salt complexes were dried *in vacuo* and stored in a dry argon atmosphere. Where noted, 10 wt. % polyethylene glycol (400) dimethyl ether (PEGDME) (Fluka, spectroscopic grade) was

added as a plasticizing agent. In the value described in Chapter 4, $NaClO_4$ was used in stoichiometric combination with PEO or PEM to obtain $PEO_{15}NaClO_4$, or $PEM_{50}NaClO_4$.

3.3 **Mechanical Behavior.**

3.3.1 **Introduction.**

The evaluation of the mechanical characteristics of PEs is accomplished by measuring sample deformation, and elasticity under an external shear force. Polymer rheology is the study of such behavior, and has been applied to numerous examples of polymeric media is under stress. The deformation, and elasticity of a polymer can be related to its fundamental characteristics of T_g, and T_m. Below the T_g, polymers are glassy and very stiff. Above the T_g, polymers are rubbery, and will eventually flow as a viscous liquid above the T_m. Polymer rheology is thus related to the frequency of force applied to the sample, as well as the temperature of the experiment. Also, the deformation of a polymer sample at a given frequency and temperature can be replicated when the sample is exposed to longer frequencies at lower temperatures, these different experiments are fundamentally related through mathematical relations detailed below.

The measurement of deformation and elasticity is accomplished with a rheometer, which imposes *stress* upon a disc of a polymer sample in a *shear* direction, and measures the resulting *strain*. Shear modulus is defined as the ratio of the stress and strain for a polymer at a given temperature:

$$G = \frac{f}{s} \tag{3.2}$$

where f, and s are stress and strain, respectively. Low shear modulus values are associated with viscous behavior (a typical value may be 10^5 dyn cm^{-2}), and strain depends upon the frequency of the applied stress. Shear modulus is represented in terms of loss, and storage modulus, where G' refers to energy elastically stored, while G" refers to shear energy lost to deformation. These components can be represented in the complex plane as:

$$G(\omega) = G'(\omega) + jG''(\omega) \tag{3.3}$$

where $j=(-1)^{-½}$, and ω is frequency. The sinusoidal relationship between stress and strain, and their complex notation, are shown in Figure 3.2.

Moduli is plotted as a function of frequency of applied stress at a reference temperature. Shear modulus of a polymer is measured for one frequency of applied force at several temperatures, then transformed to the modulus vs. frequency plot using the time-temperature superposition principle:

$$G(T_1, t) = G(T_2, t/a_T) \tag{3.4}$$

The principle is described by the logarithmic relationship between temperature and time (t) for macromolecular motion. The shift factor, a_T, adjusts modulus along the time axis over experimentally inaccessible time scales, which creates a more complete description of the mechanical behavior of the polymer from a partial data set. The shift factor is calculated

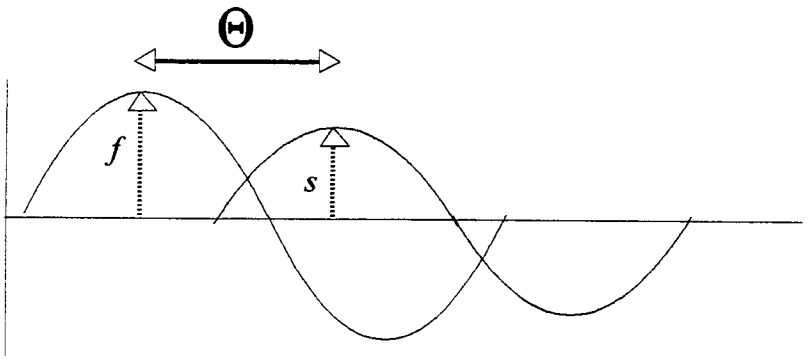

Figure 3.2. The incident stress, *f*, is separated by phase angle θ from the resulting strain, *s*. The moduli is the ratio of stress and strain magnitude.

using the Williams-Landry-Ferry (WLF) equation:

$$\log a_T = -\frac{C_1(T - T_g)}{C_2 + T - T_g} \tag{3.5}$$

Where T is the experimental temperature (in K), and C_1 and C_2 are constants. The WLF equation describes most amorphous polymers between T_g and T_g+100°C. An example of the final curve produced from the shear measurements, and the three behavior characteristics are demonstrated in Figure 3.3 [4, 6].

3.3.2 **Experimental**.

The dynamic modulus were measured in oscillatory shear between parallel plates in a Rheometrics (Piscataway, N. J.) Model RDS-2 rheometer by Tom Stephens in the U.S. Navy Weapons Research Laboratory at China Lake, CA. Disks were cut from the cast or irradiated films, then pressed to the diameter of the plates (12.7, or 9.525 mm). Samples were held in the plates with a light (100-1000 g) compressive force to ensure good contact and to prevent slipping of the sample on the plates. Care was taken to make measurements at strain amplitudes of 0.03 or less, since the modulus sometimes appeared to decrease at higher strains. The sample temperature was controlled using a convection oven that closed around the sample and the plates. Nitrogen was used in the oven to prevent oxidation.

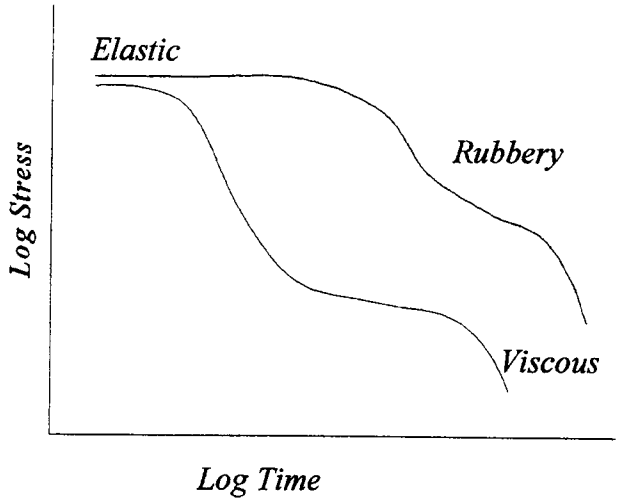

Figure 3.3. Stress decay at a reference temperature, the three regions of viscoelastic behavior are shown. A constant shear force applied for a long time result in deformation of the polymer. The crosslinked polymer (upper curve) maintains solid, elastic behavior over a larger frequency/temperature range than does the linear polymer (lower curve).

3.4 **Crosslinked Polymer Analysis by Degradation.**

A 0.5g portion of PEO, PEM, or crosslinked polymer was mixed with 5mL of $HBr/CH_3CH_2O_2H$ (Fluka, 40 % w / v) under nitrogen in a 1/4" glass tube and sealed with a flame. The mixture was allowed to react at 150° C in an oil bath for 5 h. Complete decomposition of linear PEO into dibromoethane proceeded as follows:

$$HO(CH_2CH_2O)_nH + 2nHBr \rightarrow nBrCH_2CH_2Br + 2H_2O \qquad (3.6)$$

After reaction, the tube was opened and poured into a 20 mL vial, 10 mL of water was added to the mixture, followed by five drops of dry CS_2 (Mallinkrodt, spectroscopic grade), and the mixture was then shaken and allowed to settle. The CS_2 layer contains alkyl bromides produced in the reaction. This sample was diluted 5X, and an aliquot prepared for GC / MS analysis.

A Hewlett-Packard 5890 GC fitted with a thin film stationary phase of ULTRA 2 (crosslinked 5 % phenyl methyl silicone, of dimensions: 25 m × 0.2 mm × 0.11 μm), and a Hewlett-Packard Series II Mass Selective Detector was used for analysis. The sample size was 50-100 ng.

3.5 **Li/C Preparation.**

Under an argon atmosphere, reduced graphite for LiC_x electrodes was prepared by a reaction of synthetic graphite (Aldrich, 99.99 %, average particle size < 2 μm, dried by heating to a red glow *in vacuo*) with excess lithium naphthalide. A lithium naphthalide

solution was prepared from naphthalene (Aldrich, reagent grade) and solid lithium in dry THF (Mallinkrodt, spectroscopic grade). The solid product was filtered, then rinsed with THF. The black product obtained produced H_2 gas upon reaction with water. The pressed electrode pellets had a geometric surface area of area = $1cm^2$.

3.6 $PEO_XLi_YMoO_3$ Nanocomposite Preparation.

Li_xMoO_3 was synthesized in a three-step process, MoO_3 (Aldrich, reagent, 5 g) reacted with an aqueous solution of $Na_2S_2O_3$ (Aldrich, reagent, 100 mL, 1 M) where thiosulfate reduced MoO_3 to produce the sodium bronze. The Na_xMoO_3 reaction was sonicated at ultrahigh frequency for five minutes, then stirred overnight, and allowed to settle before decanting the supernatant. Subsequent washing with water removed excess thiosulfate, and the black sodium bronze was dried *in vacuo*. X-ray diffraction (XRD) of the product indicated complete reaction by the absence of peaks associated with MoO_3.

Lithium Ion exchange was accomplished by overnight stirring of Na_xMoO_3 (1 g) with aqueous LiCl (Aldrich, reagent, 100 mL, 1 M) to produce $Li_{0.25}MoO_3$. The mixture settled for several hours before the supernatant was isolated by centrifugation (and discarded). Sodium analysis by atomic absorption spectroscopy indicated that five repetitions of the ion exchange process reduced the sodium-ion content to # 1 mol %. and the lithium content is.

$Li_xPEO_yMoO_3$ nanocomposites were prepared with the exfoliation-absorption technique [7, 8]. Anhydrous $Li_{0.25}MoO_3$ was exfoliated by sonication in 50 mL of water, and an aqueous solution of PEO (0.3 g in 60 mL) was added, and the reaction stirred

overnight. Precipitation of the composite was aided by adjusting the reaction pH - 4, 5 with a few drops of 0.1 M aqueous HCl, and centrifugation. The product was rinsed with water and dried *in vacuo*.

The electrode consisted of a weight percent mixture of 54 % PEO (a binder), 4 % brij (Aldrich), 2 % carbon black, with the balance taken up by Li_xMoO_3. Other electrodes contained 50 % nanocomposite, 44 % PEO, 4 % brij, and 2 % carbon black. The PEO-lithium bronze nanocomposite was known to contain about 25 wt.% PEO.

3.7 **Impedance Spectroscopy**.

3.7.1 **Introduction**.

Impedance Spectroscopy (IS) is used to investigate frequency dependent phenomena in PE systems, and can differentiate responses within bulk or interfacial regions of a cell. This section offers some explanation of impedance spectroscopy, and how it is used to determine conductivities and other cell parameters.

All of the relationships used in IS are developed from the fundamental electrical expressions concerning resistance and capacitance. Ohm's Law describes the direct relationship between current I and voltage V:

$$V = IR \tag{3.7}$$

The resistance of a cell can be determined from a linear plot of V vs. I under direct current. Capacitor elements store electric charge, Q. For identical parallel plates of area

A, separated by a distance ℓ, the amount of charge acquired by each plate is proportional to the applied voltage:

$$Q = CV \tag{3.8}$$

Where C (capacitance, CV^{-1} or F) is the constant of proportionality, and depends upon the nature of the dielectric material between the electrodes. The vacuum capacitance is:

$$C_0 = \varepsilon_0 \frac{A}{\ell} \tag{3.9}$$

where ε_0 is the permittivity of free space (8.85×10^{-12} C^2 N^{-1} m^{-2}). With a dielectric material placed between the plates, the capacitance of the system at a given voltage increases (with respect to a vacuum) by a factor of the dielectric constant, ε_r (unitless). Electric dipoles induced on molecules placed in an electric field, or permanent dipoles present on the molecules, will arrange to form a layer of opposite charge with respect to the capacitor plates; this electrical double layer shields the bulk from the charge present upon the plate (Figure 3.4). The dielectric constant can also be defined as the ratio of the cell voltage across the dielectric material (V), to the cell voltage across a vacuum (V_0).

$$\varepsilon_r = \frac{V_0}{V} \tag{3.10}$$

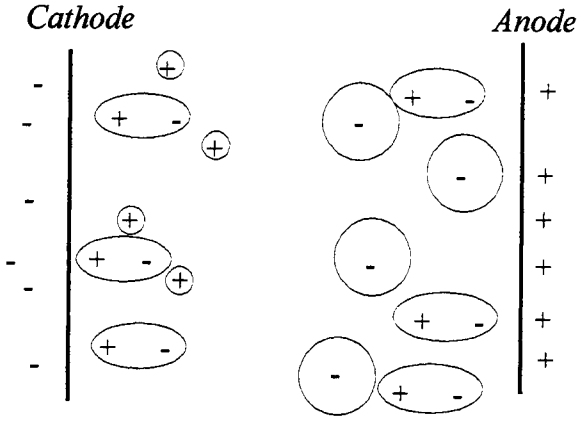

Figure 3.4. The double layer between electrode charge and ions in the bulk electrolyte, a negative electronic charge is shown on the cathode surface (on the left), and a positive charge on the anode (on the right).

The capacitance between two electrodes is proportional to the product of the free space permittivity and dielectric constant of the material filling the space.

$$C = \varepsilon_r \varepsilon_0 \frac{A}{\ell} \tag{3.11}$$

These expressions are developed from cells polarized by direct current [9].

3.7.2 The Impedance Experiment and Equivalent Circuits.

IS uses alternating voltage rather than direct current during an experiment. This allows for evaluation of individual cell impedances that add up to the overall cell response. Ions move through a conducting medium with respect to voltage direction and magnitude, their impedance is a function of voltage frequency and is characteristic of the conducting material (and temperature). The impedance of areas of the cell with unique characteristics, such as the bulk and interface, can be differentiated. In IS, high frequency alternating voltages do not polarize cells, and allow for the bulk electrolyte, and interfacial impedances to be independently evaluated.

When a sample is contained between two metal electrodes, and a sinusoidal voltage of known amplitude and frequency V_f generated, the resulting current within the bulk electrolyte possesses an amplitude, I_f, and phase shift, θ relative to the exciting potential (Figure 3.5). The impedance of a PE cell depends upon voltage frequency. The ratio of the exciting voltage to the current response is the magnitude of the impedance:

$$|Z| = \frac{V_f}{I_f} \tag{3.12}$$

Impedance can be plotted in a complex plane (Figure 3.5), where θ is the phase shift, and $|Z|$ is the sum of the real and imaginary parts: Z', and Z'', respectively

$$|Z| = Z' - jZ'' \tag{3.13}$$

where $j = (-1)^{½}$.

Models representing the AC impedance response comprise equivalent circuits, consisting of simple electrical components. Electronic resistors operate independent of frequency, in the range studied, therefore, the impedance of a single resistor is $|Z|=R$, with $\theta = 0°$ (Figure 3.6). The current response of a capacitor is shifted 90° behind the exciting voltage, and the impedance magnitude for a capacitor is frequency dependent:

$$Z^* = \frac{-j}{\omega C} \tag{3.14}$$

where ω is the angular frequency ($2\pi f$) and C is the capacitance. The response of a capacitor plotted in the complex plane is, therefore, a vertical line (Figure 3.5).

The results of some common combinations of resistors and capacitors are plotted in Figure 3.6. The typical AC impedance response for PE cells is frequency dependent with $0° \leq \theta \leq 90°$, and is represented by parallel resistor/capacitor combinations (Figure 3.5 and 3.6) [10-12].

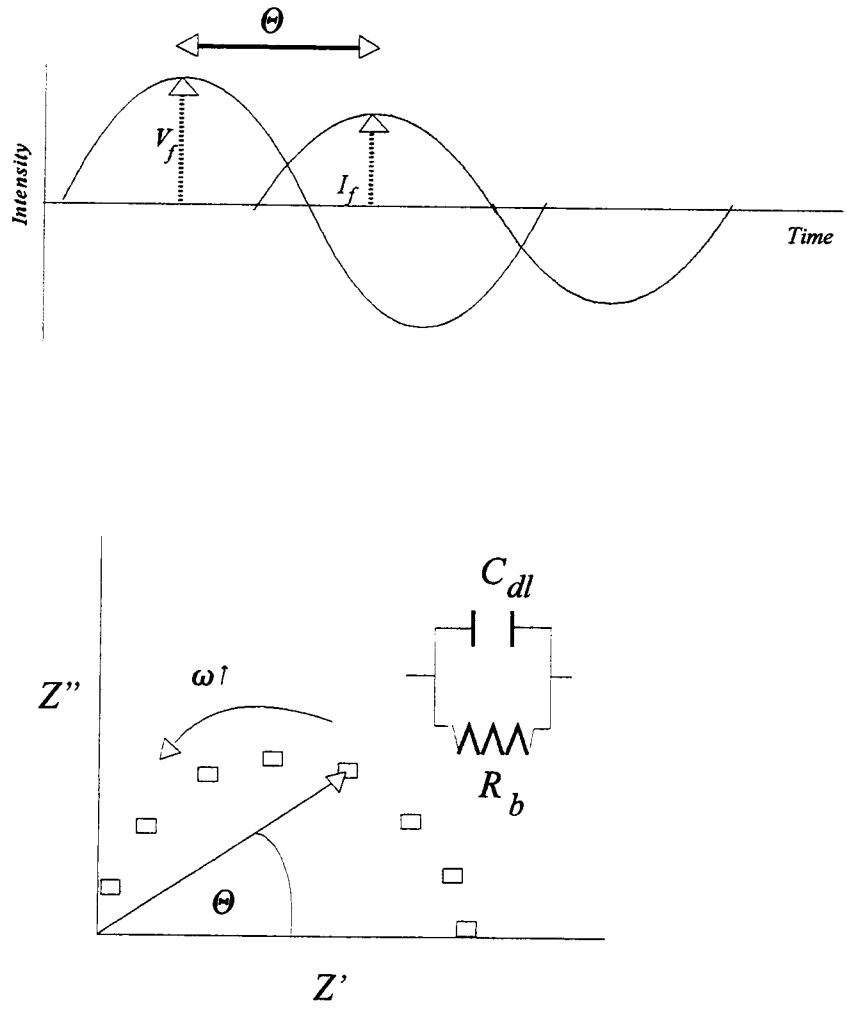

Figure 3.5. The frequency relationship between applied voltage, V_f, and the resulting current I_f, is shown in the upper graph (magnitude vs. time). The lower graph is a Nyquist plot of real vs. imaginary impedance (Ω), with an equivalent circuit shown. As the voltage frequency, ω, decreases, the impedance approaches bulk resistance: $|Z|=R_b$ where $\theta= 0$.

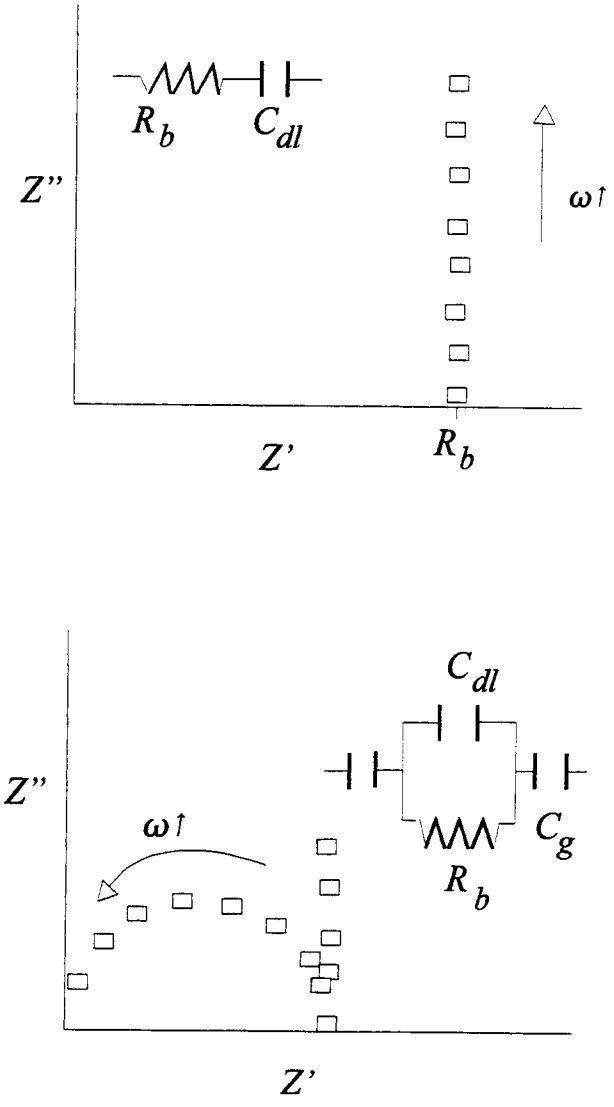

Figure 3.6. Nyquist plots of some circuit models. In the upper graph, a capacitor represents the spike, at a resistance value Z'. The lower graph is the response from non-blocking electrodes, and is represented by parallel RC circuit of bulk resistance, and double layer capacitance.

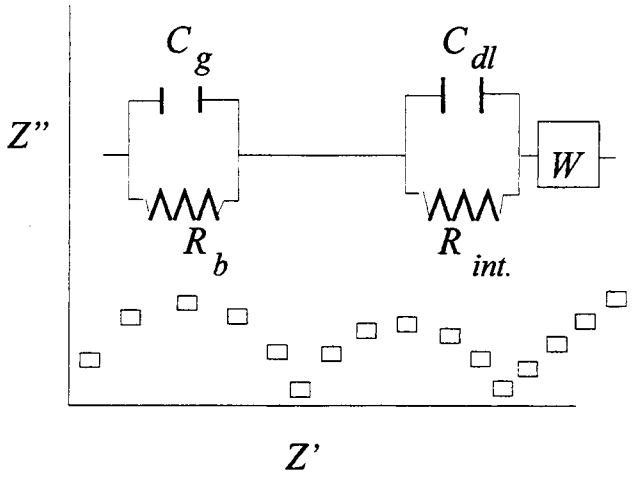

Figure 3.6. (continued) An equivalent circuit for a thin-film electrolyte cell with non-blocking electrodes, such as Li/PE/Li. The diffusion-limited Warburg element represents the 45° spur at the low frequency end of the plot. R_b is the bulk resistance of the electrolyte, and C_g is its geometric capacitance.

3.7.3 **Electrolyte Layer Thicknesses**. [3, 10, 24]

In order to translate the conductance (R^{-1}) into conductivity of any electrolyte layer, the layer thickness must be known. For a solid electrolyte interface, the geometry cannot be directly measured; however, a value can be estimated using experimental capacitance and resistance values in the equation developed below.

Firstly, IS experimental data can be represented in terms of admittance, Y^*:

$$Y^* = \frac{1}{Z^*} = \frac{1}{Z' - jZ''} = Y' + jY'' \qquad (13.15)$$

The admittance of a resistor, therefore, is $1/R$ and a capacitor is $j\omega C$ [11]. For a resistor and capacitor in a parallel, the admittance is:

$$Y^* = \frac{1}{R} + j\omega C \qquad (3.16)$$

This expression provides a convenient starting point for calculating layer thickness. Substitution of the expression for conductivity, $\sigma = \ell/AR$, and capacitance into the equation expresses admittance as a function of frequency in terms of conductivity, electrode area, electrolyte area, and dielectric constant.

$$Y^* = \frac{A\sigma}{\ell} + j\frac{\omega A \varepsilon_0 \varepsilon_r}{\ell} \qquad (3.17)$$

As noted, the impedance plot of polymer electrolytes produces semicircular arcs, and the

voltage frequency at the top of these arcs, ω_{max}, produces a Z' maximum, where $Z' = Z''$, (or $Y' = Y''$). This can be expressed as the point where $\omega_{max} RC = 1$, substitution into this yields $\omega_{max} = \sigma(\varepsilon_0 \varepsilon_r)^{-1}$. Thus, ω_{max} is independent of sample geometry, and is an intensive property [13]. Rewriting the previous equation to express conditions at the semicircle maxima leads to the following:

$$Y^* = \frac{1}{R} + j\frac{\omega_{max} \varepsilon_0 \varepsilon_r}{\ell} \tag{3.18}$$

and because $Y'=Y''$ at this point:

$$\frac{1}{R} = \frac{\omega_{max} \varepsilon_0 \varepsilon_r}{\ell} \tag{3.19}$$

which leads to an expression of electrolyte layer thickness:

$$\ell = \omega_{max} \varepsilon_0 \varepsilon_r R A \tag{3.20}$$

Where R is the resistance corresponding with the impedance semicircle, A is the electrode area, and ε_r is the dielectric constant of the electrolyte. The permittivity for the SEI layer, ε_r, was approximated as 10, which is a reasonable value for lithium carbonate or hydroxide, the probable components of a SEI in these investigations [13, 14].

3.7.4 **Blocking Electrodes**.

These electrodes are chemically inert against the electrolyte, and cannot react to consume or produce conductive ions. Stainless steel, or platinum metal served as blocking electrodes in this investigation. The impedance response of cells with this geometrical composition can be represented by an equivalent circuit with a parallel association of a resistor (bulk, R_b) and capacitor (geometric, C_g) as described in Figure 3.7 [11].

3.7.5 **Non-Blocking Electrodes**.

In an AC experiment performed on Li/PE/Li, the high frequency response has a well-defined semicircle corresponding with R_b, and C_g, as with the case above. For the low frequency response, a well-defined semicircle is observed. This can be defined by an equivalent circuit containing a parallel combination of the interfacial capacitance, C_i, and the interfacial resistance, R_i. R_i represents the charge transfer resistance for the chemical reaction, in this case: $Li^+ + e^- \rightleftharpoons Li$, or the resistance of ions through the passive layer on the electrode/electrolyte interface. The impedance response, and equivalent circuit for a solid electrolyte with nonblocking electrodes is shown in Figure 3.6 [11].

3.7.6 **The Warburg Element**.

The equivalent circuit elements provide ideal responses under an external voltage; however, several reasons exist for incorporation of distributed elements, such as a Warburg element in the description of electrical responses within PEs, and SEIs. The electrolytes occupy space and are not ideal point resistances; many possible conduction

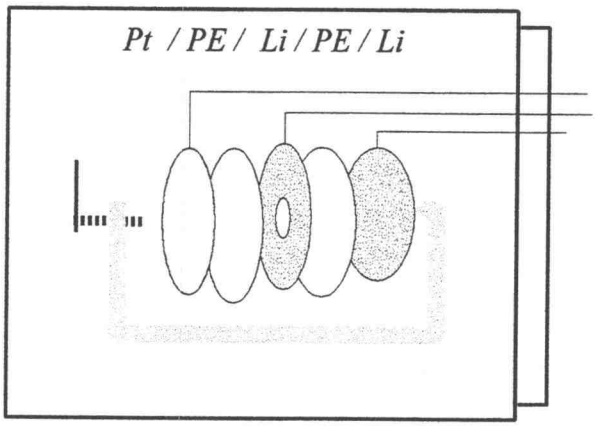

Figure 3.7. Cell geometry of the polymer electrolyte for cyclic voltammetry. Pt is the working electrode, and Li is the counter and reference electrodes.

pathways exist in the bulk electrolyte, or the SEI due to imperfections at the electrode surface, and inhomogeneities within the electrolyte. The Warburg element addresses the diffusion of charges through a finite-length diffusion pathway [10, 11].

At low frequency, the diffusion path length of an ion (assume Li^+) approaches the physical length of the electrolyte, this condition is met when the electrolyte is a thin layer. Under these circumstances, the impedance response for electrolytes with non-blocking electrodes typically demonstrates a 45° spur following the charge transfer resistance. At sufficiently low frequency, the phase angle decreases to zero at the DC limit of the cell, and the diffusion limited response is represented by the Warburg impedance [10, 11].

$$Z' = Z'' = \frac{A_w}{\omega^{1/2}} \tag{3.21}$$

Where A_w is the Warburg coefficient, and is inversely proportional to the diffusion coefficient (D_s) of the species crossing the electrode/electrolyte interface. The Warburg response Z' is directly proportional to the diffusion resistance and is an extensive property. The total diffusion resistance, and therefore Z', depends upon electrode separation, and Warburg responses are observed with thin electrolyte films with non-blocking electrodes.

3.7.7 **Constant Phase Elements**. [10]

The impedance response of an ideal parallel RC circuit produces a perfect semicircle in the complex plane. Due to inhomogeneities within polymer electrolytes,

various conduction pathways can be expected between the electrodes, each having its own impedance. This distribution results in a semicircle with its center shifted below the real axis of the complex plane. To account for the deviation from ideality, capacitor elements are replaced with constant phase elements that model the observed response.

The impedance function is manipulated with an exponential term n representative of the arc change. An ideal capacitor will have $n = 1$.

$$Z_x = \frac{R}{1 + (j\omega\tau)^{1-n}} \tag{3.22}$$

The distribution of relaxation times is reflected in the value of n $(0 \leq n \leq 1)$, with extensive arc change modeled with small values.

3.7.8 Impedance and DC Experiments.

These were performed using a Solartron 1260 Impedance Analyzer with a computer-controlled oven/cooler, sinusoidal exciting voltages (100-1000 mV) were applied (10 MHz to 5 mHz). DC potentiometry was performed on a PAR 362 Scanning Potentiostat using current densities from 0.1 mA to 0.001 mA.

3.8 **Cyclic Voltammetry.** [15]

The solid cells used in this investigation were composed of two layers of PE, each 100 μm thick, surrounding the lithium reference electrode, which was sandwiched between the platinum working electrode, and the stainless steel counter electrode. All

electrodes were 1 cm^2, and the lithium reference electrode had a hole ≈ 0.2 cm^2 to allow ions to migrate between the working and counter electrodes. The cell was held together with a modified C-clamp and placed into an argon-filled Nalgene container (Figure 3.7).

3.9 **References.**

1. Lemmon, J. P.; Lerner, M. M. *Macromolecules* **1992**, *25*, 2907.

2. Craven, J. R.; Mobbs, R. H.; Booth, C.; Giles, J. R. M. *Macromol. Chem. Rapid. Commun.* **1986**, *7*, 81.

3. Nicholas, C. V.; Wilson, D. J.; Booth, C.; Giles, J. R. M. *Br. Polym. J.* **1988**, *20*, 289.

4. Sperling, L. *Introduction to Physical Polymer Science* Wiley & Sons: New York, 1986; pp. 343-344.?

5. Ballard, D. G. H.; Cheshire, P.; Mann, T. S.; Przeworski, J. E. *Macromolecules* **1990**, *23*, 1256.

6. Rudin, A. *The Elements of Polymer Science* AP: New York, 1982.

7. Lemmon, J. P., Ph.D. Thesis, Oregon State University, 1994.

8. Lemmon, J. P.; Wu, J.; Oriakhi, C.; Lerner, M. M. *Electrochim. Acta* **1995**, *40*, 2245. 7.

9. Gianncoli, D. C. *Physics* 2nd Ed.; Prentice Hall: New Jersey, 1985; ch.s 15-18.

10. Macdonald, J. R. *Impedance Spectroscopy* J. Wiley & Sons: New York, 1987; ch.s 1-2.

11. Bruce, P. G. in *Polymer Electrolyte Reviews-1* MacCallum, J. R.; Vincent, C. A.; Elsevier: New York, 1989; ch. 8.

12. Armstrong, R. D.; Todd, M. in *Solid State Electrochemistry* Bruce, P. G. Ed.; Cambridge: New York, 1995; ch. 10.

13. Murugesamoorth, K. A.; Owen, J. R. *Br. Polm. J.* **1988**, *20*, 227.

14. Linden, E.; Owen, J. R. *Br. Polm. J.* **1988**, *20*, 237.

15. Gosser, D. K. *Cyclic Voltammetry* VCH: New York, 1994.

Chapter 4

Crosslinking Poly(ethylene oxide) and Poly[oxymethylene-oligo(oxyethylene)] with Ultraviolet Radiation.

S. E. Sloop* , M. M. Lerner* , T. S. Stephens, A. L. Tipton, D. G. Paull,

and J. D. Stenger-Smith

*Department of Chemistry and Center for
Advanced Materials Research
Oregon State University
Corvallis, Oregon 97330

Naval Air Warfare Center
Weapons Division
China Lake, CA.

J. Appl. Polym. Sci. **1994**, *53*, 1563.

4.0 **Abstract.**

Poly(ethylene oxide) (PEO) and poly[oxymethylene-oligo(oxyethylene)] (PEM) disks are crosslinked by exposure to 254 nm radiation. The rate of formation of crosslinks is greatly enhanced in the presence of benzophenone, and an average crosslink density of up to 6 mol% of ethoxy units can be obtained after several hours of irradiation. The highly crosslinked polymers are insoluble in water or organic solvents and show improved mechanical properties. Scanning calorimetry, polymer swelling, and gas chromatography-mass spectroscopy of degradation products from the crosslinked polymers are employed for characterization. Impedance measurements are reported for the crosslinked PEM, or PEO sodium-salt electrolytes. Dynamic modulus measurements show that, upon irradiation, PEO and PEM become crosslinked elastomeric solids.

4.1 **Introduction.**

Polymer electrolytes (PEs) from etheric polymers including PEO, PEM, poly[bis(2-(2-methoxyethoxy) ethoxy)phosphazene (MEEP), are investigated for use in high energy density batteries and electrochromic displays [1-4]. A general observation is that the highest ionic conductivities are found in completely amorphous materials that typically have relatively low viscosity, and do not readily form freestanding films. Investigated methods of producing crosslinked polyethers with improved mechanical characteristics include a variety of chemical syntheses[4-12] as well as gamma irradiation[13-15]. Other studies of crosslinking polyethers using similar methods were

directed toward applications such as surgical dressings [16, 17], controlled drug delivery, [16, 18, 19] and semipermeable membranes [20].

Recently, Allcock and co-workers[21] reported that MEEP undergoes crosslinking when exposed to UV radiation, with and without benzophenone added as a photoinitiator. PEO was also indicated to undergo a similar reaction, although these products were not characterized in the study. The ease, relative safety, and low cost of UV radiation in crosslinking PEO and PEM would provide significant advantages over other methods. The purpose of the effort was to examine the effect of UV radiation on the ionic transport properties, rheology, and other physical properties of PEO and PEM.

4.2 **Experimental.**

PEO ($M_w = 5\times10^6$ D; Aldrich) was dissolved in acetonitrile (Mallinkrodt, spectroscopic), and the viscous solution was cast onto Teflon matting and dried in air. The polymer was cut into disks about 0.4mm thick and further dried at 60°C *in vacuo* for 12h. PEM ($M_w = 7.5\times10^4$D) was prepared from synthesis following a literature method[22-23]. Disks were formed in glass rings and dried as above. Samples containing benzopheneone (Spectrum, reagent grade) as a photoinitiator were similarly prepared; sublimation of benzophenone from the samples did not prove significant under these conditions. PEO solutions with benzophenone were handled under red light to avoid polymer scission, and disks were stored in the dark. PEM samples containing benzophenone were not noticeably degraded under ambient light. Following irradiation,

benzophenone and low molecular weight by-products were removed in acetone (Mallinkrodt, Spectroscopic).

Disks were sealed in 1 in. diameter quartz tubes and place into a Rayonet rotating UV reactor fitted with Hg vapor tubes (254 nm). Irradiation time was varied from 5 min to 60 h. Samples were rotated to promote even exposure. Irradiated disks placed in deionized water swell isotropically relative to the extent of crosslinking. The Flory-Rehner equation was employed to derive a value for crosslink density[24]:

$$n = -[\ln(1 - \nu_2) + \nu_2 + \chi \nu_2^2]/V_1[\nu_2^{1/3} - \nu_2/2] \qquad (4.1)$$

where n is the crosslink density (mol/mL), ν_2 is the unswollen polymer volume/swollen polymer volume ratio, and V_1 is the molar volume of the solvent (mL / mol). χ is the polymer-solvent interaction parameter, which has a value of 0.45 for PEO/water systems [25], and has been used to describe other PEO crosslinked systems [26]. Crosslink densities are reported in moles per liter and mole percent. Mole percent refers to the number of crosslinks present per 100 ethoxy units in the polymer sample.

PEs of formulation $PEM_{50}NaClO_4$ and $PEO_{15}NaClO_4$ were produced by swelling the crosslinked polymers with the salt (EM, reagent) in freshly distilled acetonitrile. The swollen mass was gently stirred for 12 h. X-ray diffraction of the products has no peaks corresponding to salt crystals, and the stoichiometric ratios were confirmed for several samples by means of sodium atomic emission analysis.

Samples of crosslinked PEO (XPEO), and linear PEO were placed (100 mg) in 5 mL of a HBr / acetic acid mixture in a sealed 1/4" glass tube under Ar, and heated to

150° C in an oil bath [27]. The decomposition products were extracted with CS_2 (Mallinkrodt, Spectroscopic), and analyzed with an HP1290C gas chromatograph-mass spectrograph fitted with an HP-5MS crosslinked 5% phenyl-methyl silicone, 30 mx × 0.25 μm column.

Variable temperature impedance measurements were performed using a computer-controlled Solartron 1260 impedance analyzer and a Sun ECO1 oven. Samples were prepared as pressed disks, placed between two stainless-steel, blocking electrodes in an airtight Kel-F cell, and annealed at 70° C for several hours.

DSC measurements were obtained at a heating rate of 10 K/min using a Shimadsu DSC 50. Under an inert atmosphere, samples were loaded into hermetically sealed pans, and were quenched from above the melting point prior to measurement. Thermal transitions were recorded at the onset point. Proton and carbon NMR spectra of native and crosslinked polymers were obtained using a Bruker 300 MHZ instrument; IR spectra of polymer films sere obtained on a Nicolet 510P FTIR.

The dynamic modulus were measured in oscillatory shear between parallel plates in a Theometrics (Piscataway, N. J.) Model RDS-2 rheometer. Disks were cut from the cast or irradiated films, then pressed to the diameter of the plates (12.7, or 9.525mm). Samples were held in the plates with a light (100-1000g) compressive force to ensure good contact and to prevent slipping of the sample on the plates. Care was taken to make measurements at strain amplitudes of 0.03 or less, since the modulus sometimes appeared to decrease at higher strains. The sample temperature was controlled using a convection

oven that closed around the sample and the plates. Nitrogen was used in the oven to prevent oxidation.

4.3 **Results and Discussion.**

UV-vis spectra for PEO and PEM (Figure 4.1) exhibit a strong absorption centered at 190 nm, corresponding to a n-σ^* transition. The absorptivity in the frequency range produced by standard UV sources (250 - 300 nm) is relatively low. The dispersion of a small quantity of a conjugated molecule (such as benzophenone) greatly increases absorptivity in this range and result in an increase in the rate and extent of the photochemical reactions observed.

Sample disks approximately 0.4 mm thick were irradiated; this thickness was dictated by the requirement for rheology measurements. Disks of this thickness containing benzophenone almost completely absorb or scatter radiation at 254 nm (Figure 4.2); therefore, the photochemistry does not occur homogeneously through the disk. As a compromise between reaction rate and product homogeneity, 0.5 mol % benzophenone was chosen. Some of the thicker samples were observed to split into two films when placed into water, indicating that much of the crosslinking occurs at the surfaces. Figure 4.3 provides an estimate of the crosslink density profile across the body of a disk, where the average value of the curve represents the crosslink density measurement. All crosslink density measurements represent an average value due to the inhomogeneous distribution of crosslinks throughout the film. Nyquist plots from crosslinked PEM is shown in Figure 4.4, dampening of the semicircle is noticeable, and can be modeled with constant phase

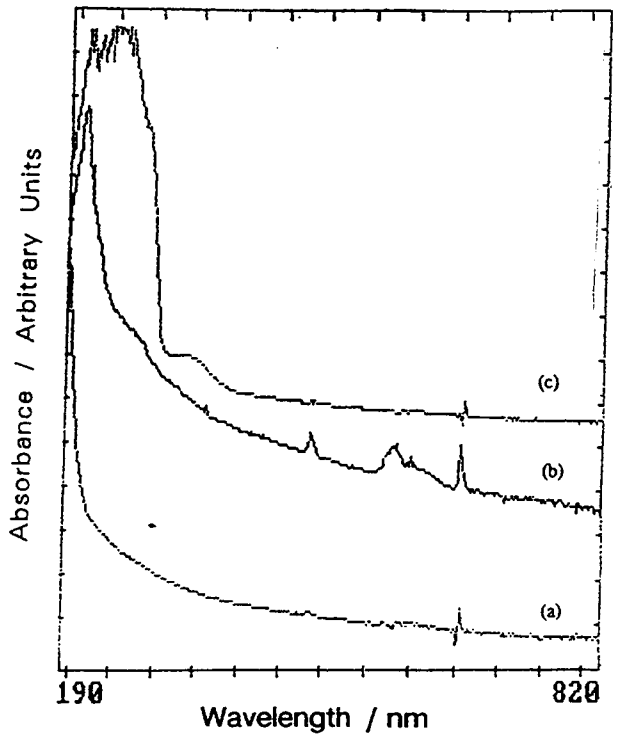

Figure 4.1. UV-Vis spectra for (a) PEO, (b) PEM, and (c) 0.5 mol % benzophenone in PEM.

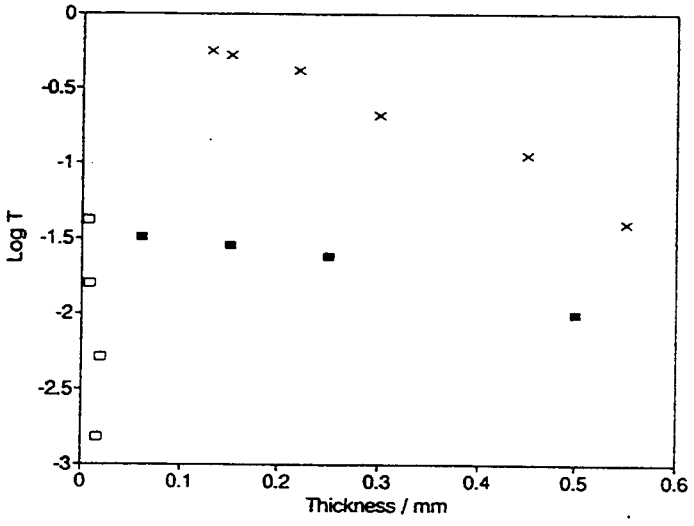

Figure 4.2 Log (transmittance) at 254 nm vs. Sample thickness for (■) PEO, (×) PEM, and (□) PEM containing 0.5 mol% benzophenone.

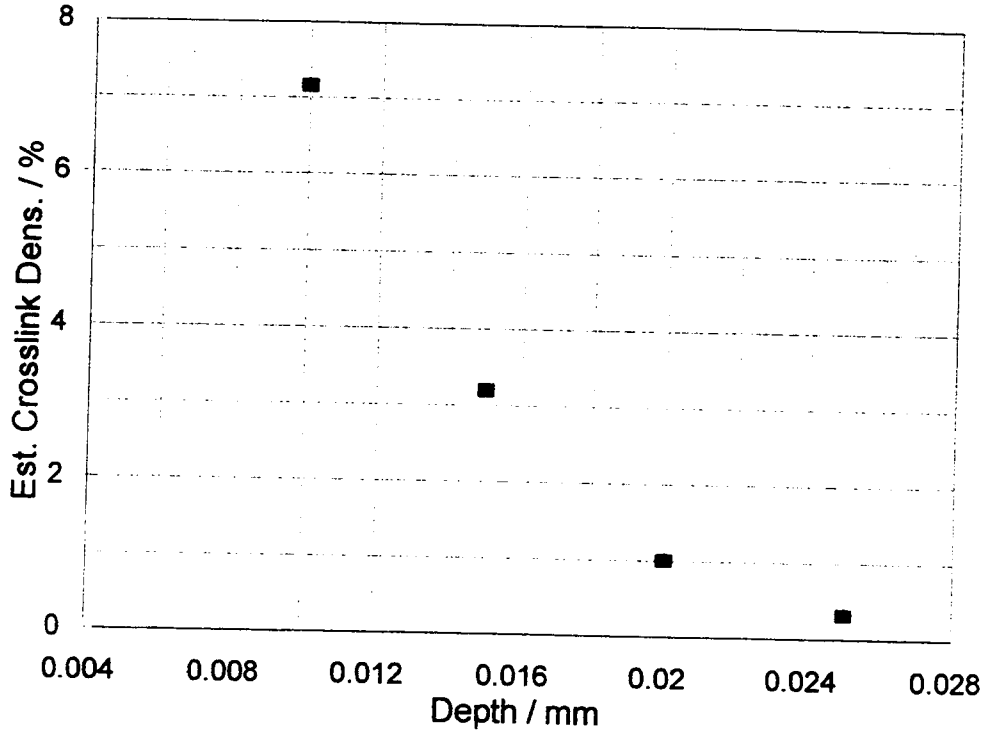

Figure 4.3 A representation of the crosslink density profile through the body of a film, derived from transmittance data.

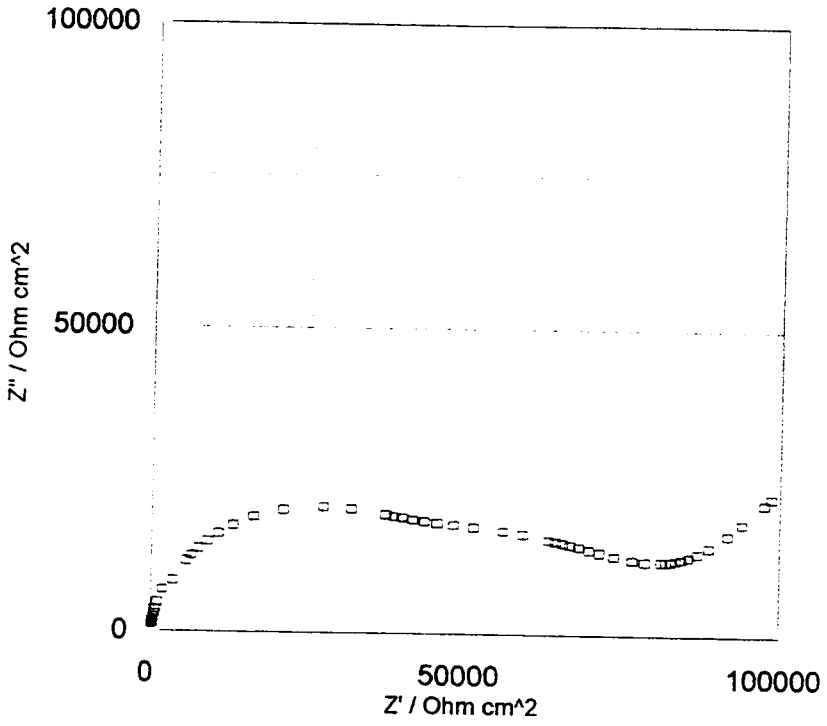

Figure 4.4 A Nyquist plot of ss/ $XPEM_{25}LiClO_4$ /ss, with a 2 mm electrolyte thickness. Crosslinking the electrolyte dampens the semicircle.

elements, which represent inhomo-geneities within a conductor that may produce resistive pathways to mobile ions [28].

Average crosslink densities typically increase with irradiation time and are enhanced by 1 or 2 orders of magnitude by the addition of the photoinitiator. As can be seen in comparing samples 7-9 with 10-13 in Table 4.1. A variation in the mean crosslink density obtained is observed under similar controlled conditions. At very long irradiation times, the decrease in mean crosslink density may correspond to significant scission of the polymer chains.

The thermal transitions of irradiated samples are essentially unchanged from those of the linear polymers. Glass transition temperatures (T_g) for all PEO and PEM samples were between -60 and -62°C, and melting endotherm were observed between 53 and 57°C for XPEO, and 5 to 10°C for XPEM. The transitions arising from the crosslinked polymer may be greatly broadened from the ensemble effect of a distributed range, where the fraction of the sample with shallow crosslink density provides the measured sharp transition. A small low-temperature shoulder on the melting endotherm is visible for some crosslinked PEO samples and may indicate two melting phases present.

Arrhenius plots for PEs from XPEM, and XPEO are shown in Figures 4.5-4.7. No significant changes in conductivities are observed through the temperature range evaluated in the samples with an average crosslink density of up to 1%.

The apparent dynamic moduli data for each sample were plotted as master curves, according to the time-temperature superposition principle [29]. Curves of the shear

Sample No.	Composition	Irradiation Time (h)	Volume Increase	Mean Cross-link Density	
				(Mol/L)	(Mol %)
1	PEO	1.0	Soluble	—	—
2	PEO	1.7	79	0.0006	0.008
3	PEO	30	35	0.0091	0.033
4	PEO	66	5.1	0.57	2.1
5	PEM	24	40	0.007	0.03
6	PEM	48	35	0.009	0.04
7	PEO + 0.5% BzPh	0.08	3.8	1.2	4.5
8	PEO + 0.5% BzPh	0.75	3.5	1.5	5.5
9	PEO + 0.5% BzPh	5	3.3	1.8	6.6
10	PEO + 0.5% BzPh	0.08	6.3	0.33	1.2
11	PEO + 0.5% BzPh	1.0	4.9	0.62	2.2
12	PEO + 0.5% BzPh	6	4.5	0.77	2.8
13	PEO + 0.5% BzPh	31	6.8	0.28	1.0
14	PEM + 0.5% BzPh	0.75	Soluble	—	—
15	PEM + 0.5% BzPh	3	16	0.045	0.31
16	PEM + 0.5% BzPh	6	12	0.074	0.39
17	PEM + 0.5% BzPh	13	9.4	0.13	0.52

able 4.1 Sample compositions, irradiation time, volume increases in water, and average crosslink densities determined from the lory-Rehner equation.

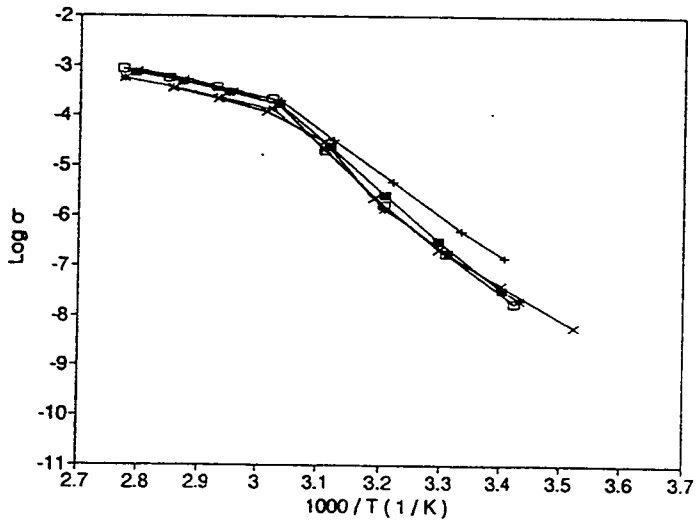

Figure 4.5 Arrhenius plots for $PEO_{15}NaClO_4$ prepared from XPEO samples (□) 1, (+) 2, (*) 3, and (×) 4.

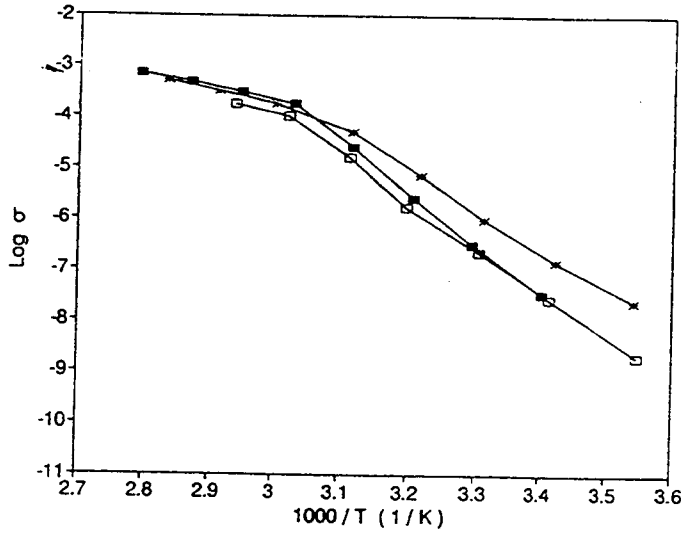

Figure 4.6 Arrhenius plots for $PEO_{15}NaClO_4$ prepared from (■) linear PEO and XPEO samples (□) 12, and (*) 13.

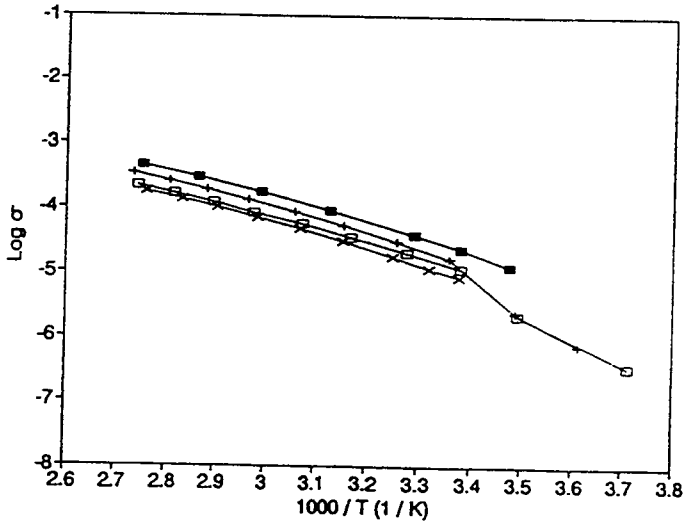

Figure 4.7 Arrhenius plots for $PEM_{50}NaClO_4$ prepared from (■) linear PEM and XPEM samples (+) 15, (□) 16, and (×) 17.

storage modulus, G', and the shear loss modulus, G'', vs. angular frequency, ω, measurements at different temperatures can be superimposed on curves measured at one temperature by plotting $b_T G'$ and $b_T G''$ vs. $a_T \omega$, where the shift factors a_T and b_T are dependent only on temperature. The factor b_T is defined as $T_0 \rho_0 / T\rho$, where T is the measurement temperature; T_0 is the reference temperature; ρ is t density at the measurement temperature and ρ_0 is the density at the reference temperature. The factor a_T is chosen so that curves measured at different temperatures superimpose with the curves measured at the reference temperature. The temperature dependence of the density was neglected here, since the density ratio $\rho_0 / \rho \approx 1$, and b_T was calculated as the ratio of absolute temperatures.

The dynamic modulus will vary through the profile of the film as a function of the distribution of crosslinks, and values will represent a weighted average. A soft layer at the sample center will tend to dominate the measurements, so the actual dependence to modulus on the extent of crosslinking will be suppressed. Although the actual modulus is not measured in heterogeneous samples, liquid behavior can be distinguished from solid behavior. Apparent modulus values reported here are computed from the measured torques and average strains.

The apparent storage moduli of linear and crosslinked PEO samples are shown in Figure 4.8, and the apparent loss modulus are shown in Figure 4.9. The open symbols show modulus for the linear PEO, and the closed symbols denote the values for XPEO of various irradiation times. With short irradiation times, the apparent storage and loss moduli decrease. This may be due to chain scission, which occurs simultaneously with

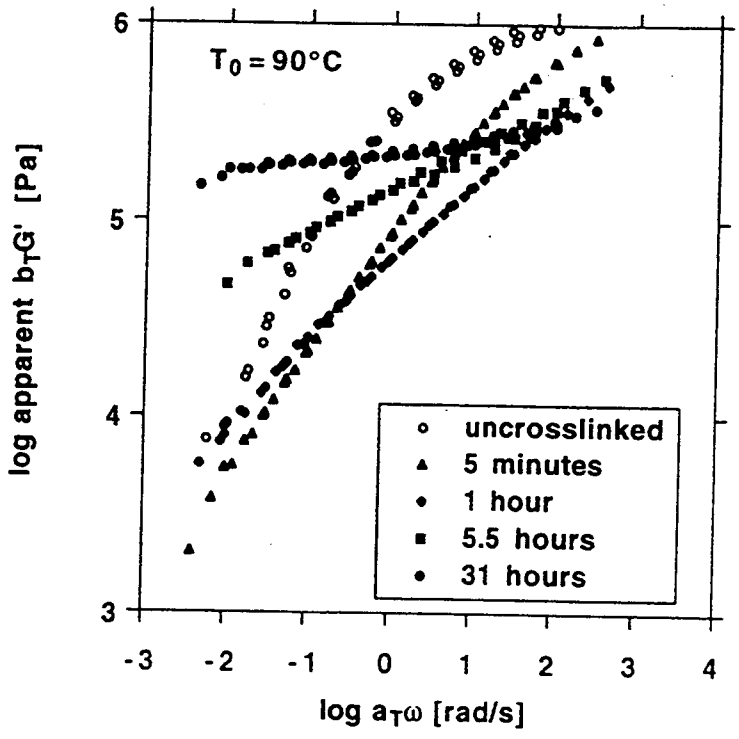

Figure 4.8 Apparent shear storage modulus for (O) linear PEO, and XPEO irradiated for (▲) 5min, (♦) 1 h, (■) 5.5 h, and (●) 31 h. Curves measured at different temperatures are shifted to the reference temperature of 90°C.

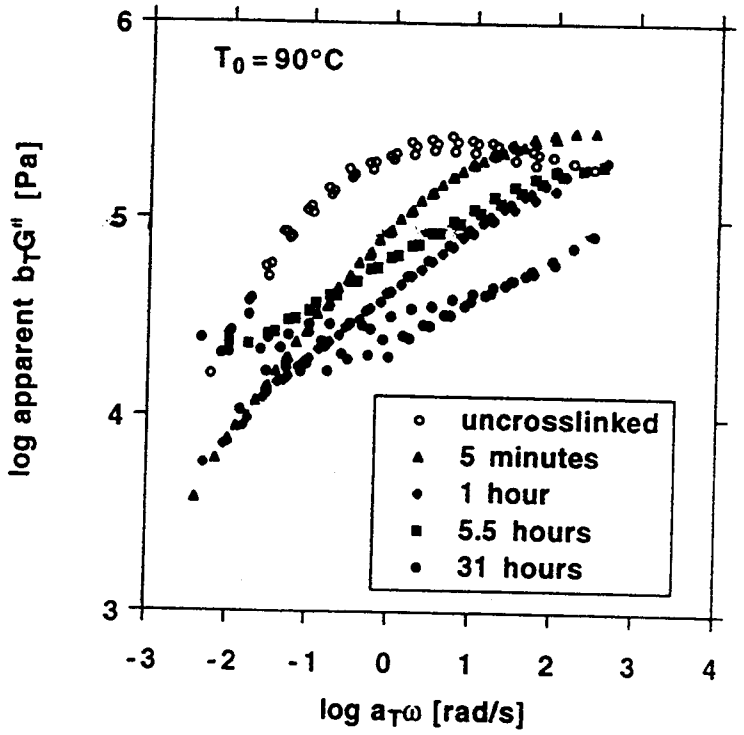

Figure 4.9 Apparent shear loss modulus for (○) linear PEO, and XPEO irradiated for (▲) 5min, (♦) 1 h, (■) 5.5 h, and (●) 31 h. Curves measured at different temperatures are shifted to the reference temperature of 90°C.

crosslinking. For irradiation times longer than 1 h, the storage modulus increases, especially at low frequencies, consistent with network formation. After 31 h, the apparent storage modulus shows a low-frequency plateau or only a very slight frequency dependence. Contrary to the degree of crosslinking as measured by swelling, the dynamic modulus data indicate that upon irradiation the PEO initially undergoes softening, then crosslinked into a network, with a monotonic increase in crosslink density with time. With sufficient crosslinking, the PEO becomes a stiff elastomer (above its crystalline melting point). Measurement of the dynamic modulus of XPEO below the crystalline melting point was not possible as the modulus were too high (above 10^6 Pa) for these thin samples.

The apparent storage moduli of linear and crosslinked PEM samples are shown in Figure 4.10, and the apparent loss modulus, in Figure 4.11. The open symbols denote the values for linear PEM, and the closed symbols, for XPEM. Upon crosslinking, both the apparent storage and loss moduli increase at low frequencies and become less frequency dependent. These observations are consistent with a broadening of the molecular weight and very light crosslinking.

The shift factor a_T and the apparent modulus obey an Arrhenius temperature dependence over the temperature range studied, as shown in Figure 4.12 and 4.13. Activation energies for flow vary, with reaction time, and are displayed in Table 4.2. These energies cannot be easily related to the extent of crosslinking because of the heterogeneous nature of the disks.

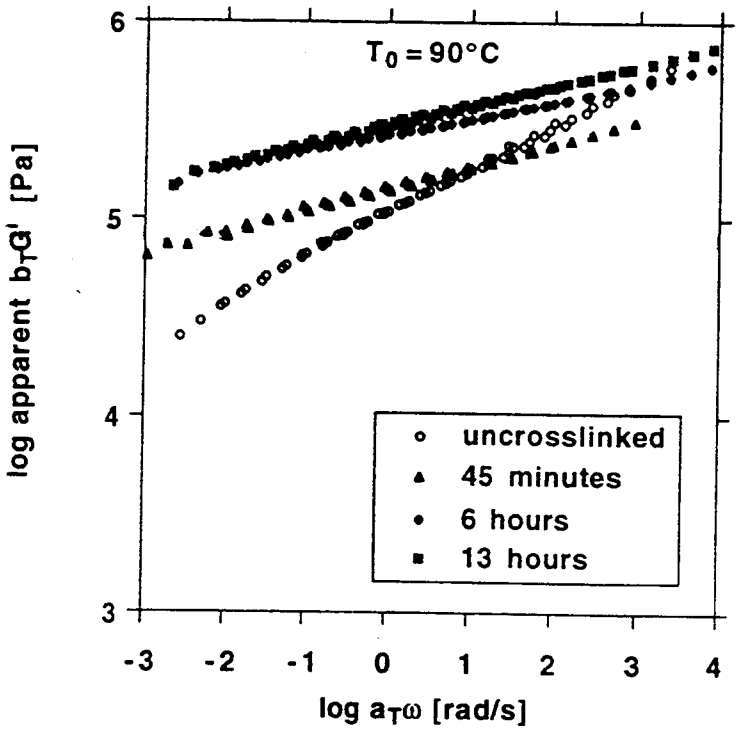

Figure 4.10 Apparent shear storage modulus for (○) linear PEM, and XPEM irradiated for (▲) 45min, (♦) 6 h, and (■) 13 h. Curves measured at different temperatures are shifted to the reference temperature of 90°C.

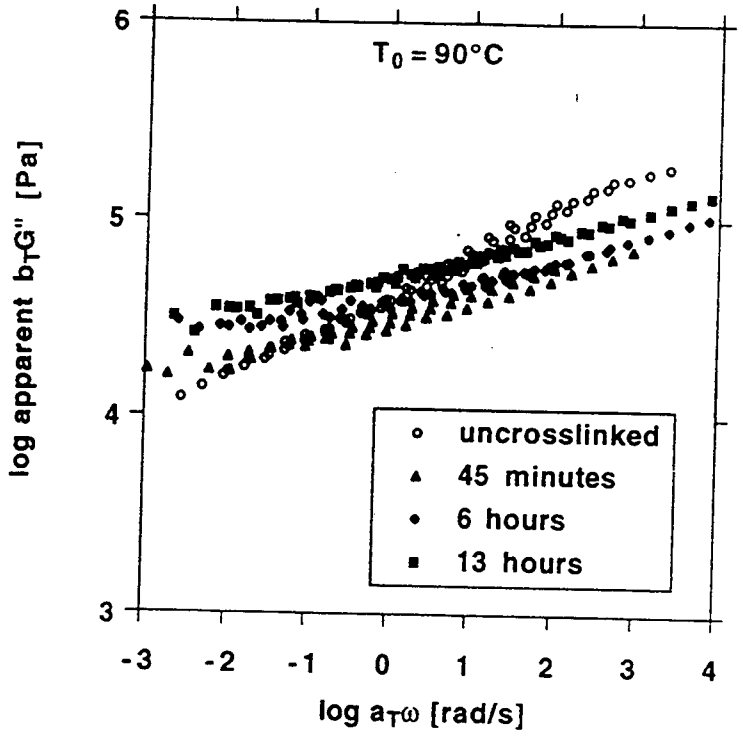

Figure 4.11 Apparent shear loss modulus for (○) linear PEM, and XPEM irradiated for (▲) 45min, (♦) 6 h, and (■) 13 h. Curves measured at different temperatures are shifted to the reference temperature of 90°C.

PEO			PEM	
Irradiation Time (h)	Activation Energy (cal/mol)		Irradiation Time (h)	Activation Energy (cal/mol)
0	7,100		0	12,000
0.083	9,100		0.75	22,000
1.0	9,700		6.0	17,000
5.5	10,000		13.0	16,000
31.0	8,600		-	-

Table 4.2 Activation energies for irradiated samples as determined by oscillatory shear.

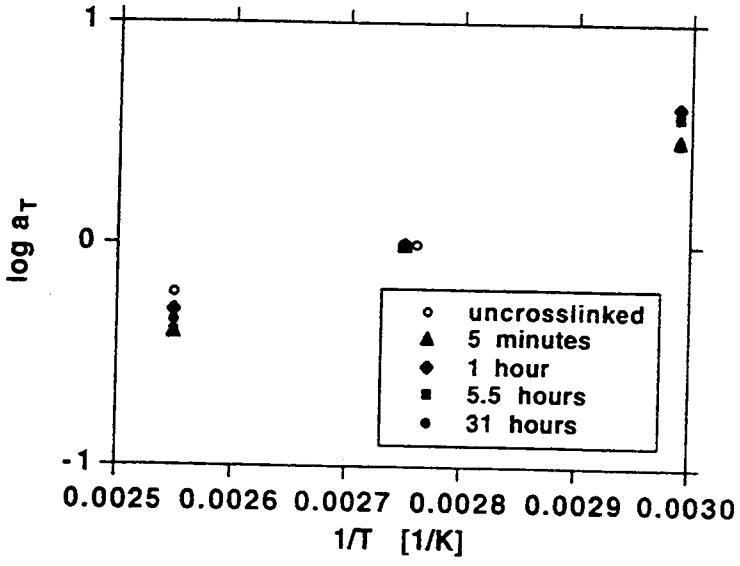

Figure 4.12 Arrhenius plots for the shift factor a_T from the dynamic modulus of (○) linear PEO, and XPEO irradiated for (▲) 5min, (♦) 1 h, and (■) 5.5 h, and (●) 31 h.

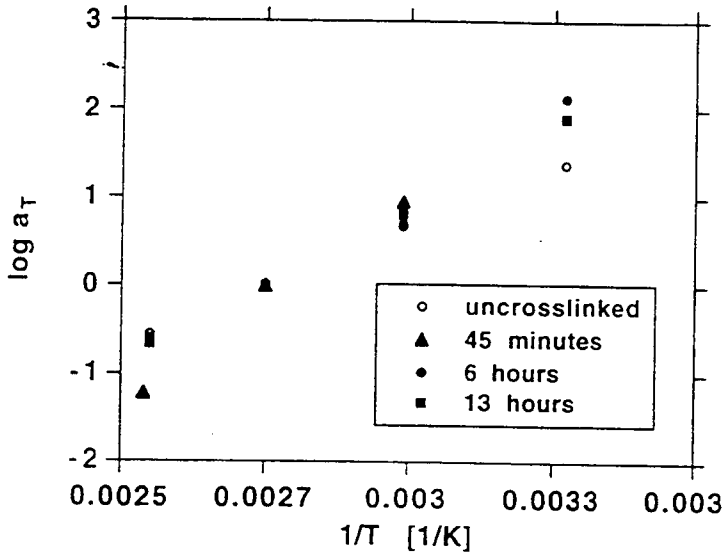

Figure 4.13 Arrhenius plots for the shift factor a_T from the dynamic modulus of (○) linear PEM, and XPEM irradiated for (▲) 45min, (♦) 6 h, and (■) 13 h.

Mechanistic details of the photochemical reactions that occur in the systems are not well understood; however, some evidence exists describing the nature of crosslink and branch sites formed. The photochemistry of polyethers is thought to initiate with the homolytic scission of C-O as has been demonstrated in the irradiation of short-chain ethers[30] and polyethers[31] with UV light. The chemistry following this initial event can be complex, and many possible routes are feasible: radicals generated may undergo intramolecular rearrangement, producing unsaturated groups, or may interact with other polymer chains producing crosslinks. Figure 4.14 shows the presence of 1,2,3,4 tetrabromobutane in GCMS analysis of the decomposition products from XPEO provides some evidence of a crosslink site produced in step 3 of Reaction Scheme 4.1, and the presence of tribromobutane suggests branch sites possibly formed in step 4.

The proton and carbon NMR spectra of even highly crosslinked products do not show new signals; however, the ^{13}C signals are noticeably broadened, which may be due to the ensemble effect of multiple crosslink sites, or may arise form the slow relaxation kinetics in highly crosslinked networks.

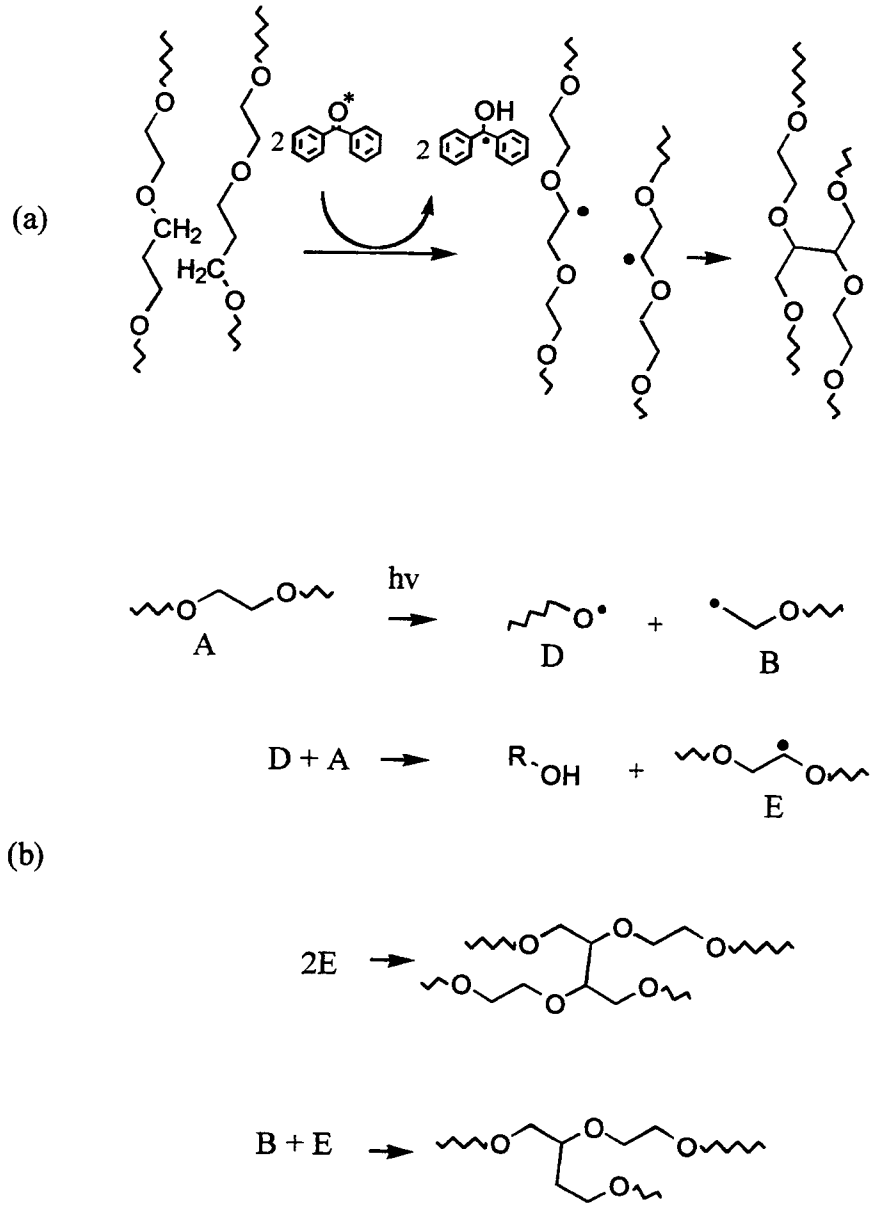

Reaction Scheme 4.1 The initial step in (a) is the excitation of benzophenone followed by hydrogen abstraction and crosslink formation. The initial step in (b) is direct C-O bond scission. The ensuing steps involve H abstraction and then termination by combining two radical polymer chains in close proximity within the solid.

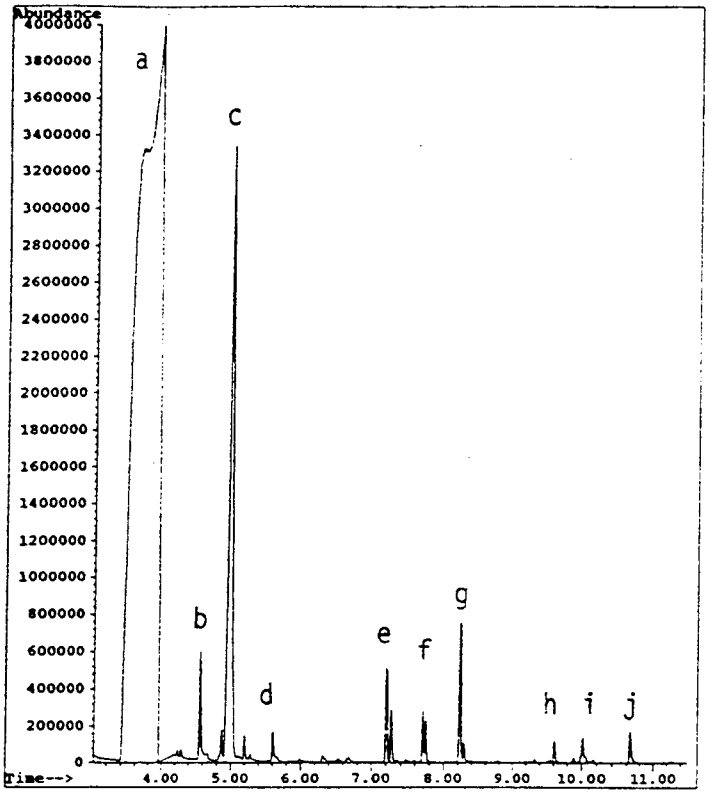

7% CROSSLINKED PEO

a. 1,2 dibromoethane
b. tribromomethane
c. 1-bromo-2-flurobenzene
d. 1,3-dibromobutene
e. 1,4-dibromo-2-butene and
   1,2,3-tribromopropane
f. 1,1,2-tribromobutane
g. 2,2,3-tribomobutane
h. 1,2,3,4-tetrabromobutane
i. 1,2,3,4-tetrabromobutane
j. benzophenone

Figure 4.14 Chromatogram and GCMS analysis of the degradation products from crosslinked PEO. Peaks a, b, c, and e were exclusively represented the control.

4.4 **References.**

1. MacCallum, J. R.; Vincent, C. A. Ed.s *Polymer Electrolyte Reviews - 1* Elsevier: New York, 1987.

2. MacCallum, J. R.; Vincent, C. A. Ed.s *Polymer Electrolyte Reviews - 2* Elsevier: New York, 1989.

3. Ratner, M.; Shriver, D. F. *Chem. Rev.* **1988**, *88*, 109.

4. Gray, F. M. *Solid Polymer Electrolytes* VCH: New York, 1991.

5. Killis, A.; LeNest, J. F.; Gandini, A.; Cheradame, H.; Cohen-Addad, J. P. *Solid State Ionics* **1984**, *14*, 231.

6. Ballard, D. G. H.; Cheshire, P.; Mann, T. S.; Przeworski, J. E. *Macromolecules* **1990**, *23*, 1256.

7. Peng, X. Ba, H.; Chen, D.; Wang, F. *Electrochim. Acta* **1992**, *37*, 1569.

8. LeNest, J. F.; Callens, S.; Gandini, A.; Armand, M. *Electrochim. Acta* **1992**, *37*, 1585.

9. Benrabah, D.; Sanchez, J. Y.; Armand, M. *Electrochim. Acta* **1992**, *37*, 1737.

10. MacFarlane, D.; Philpott, A.; Tetaz, J.; U.S. Patents 5,153,820 and 5,146,391; 1992.

11. Shackle, D.; Lee, M. ; U.S. Patent 5,037,712; 1991.

12. Kuruda, N.; Kobayashi, H.; Matsuura, K.; U.S. Patent 4,970,012; 1990.

13. MacCallum, J. R.; Smith, M. J.; Vincent, C. A. *Solid State Ionics* **1984**, *11*, 307.

14. Bennett, J. L.; Dembeck, A. A.; Allcock, H. R.; Heyen, B. J.; Shriver, D. F. *Chem. Mater.* **1989**, *1*, 14.

15. Zhang, L.; Zhang, W.; Zhang Z.; Yu, L.; Zhang, H.; Qi, Y.; Chen, D. *Radiat. Phys. Chem.* **1992**, *40*, 501.

16. Harris, J. M. Ed. *Poly(ethylene glycol) Chemistry: Biotechnical and Biomedical Applications* Plenum Press: New York, 1992.

17. King, P. A.; U.S. Patent 3,419,006; 1966.

18. Mebrey, M.; Graham, N.; U.S. Patents 5,079,009; 1992. And 5,017,382; 1991.

19. Hennink, W.; Juizer, L.; U.S. Patent 5,019,100; 1991.

20. Yankov, L.; Filipova, S.; Zlatonov, I.; Budevski, E. ; U.S. Patent 4,959,396; 1990.

21. Nelson, C. J.; Coggio, W. D.; Allcock, H. R. *Chem. Mater.* **1991**, *3*, 786.

22. Nicholas, C.V.; Wilson, D. J.; Booth, C.; Giles, J. R. M. *Br. Polym. J.* **1988**, *20*, 289.

23. Lemmon, J. P.; Lerner, M. M. *Macromolecules* **1992**, *25*, 2907.

24. Sperling, L., Ed. *Introduction to Physical Polymer Science* Wiley & Sons: New York, 1986; pp. 343-344.

25. Strazielle, C. *Makromol. Chem.* **1958**, *119*, 50.

26. Gnanou, Y.; Hild, G.; Rempp, P. *Macromolecules* **1987**, *20*, 1662.

27. Stead, J. B.; Hindley, A. H. *J. Chromatog.* **1969**, *42*, 470.

28. Macdonald, J. R. *Impedance Spectroscopy* Wiley & Sons: New York, 1987.

29. Ferry, J. *Viscoelastic Properties of Polymers* Wiley: New York, 1980; ch. 11.

30. Sonntag, C.; Schuchmann, J.; Schomberg, G. *Tetrahedron* **1972**, *28*, 4333.

31. Ivanova, T.; Melnikov, M.; Fok, N. *Dokl. Akad. Nauk SSR* **1976**, *231*, 649.

Chapter 5

Study of the Poly[oxymethylene oligo-(oxyethylene)] / Lithium Metal Interface: Comparison of Linear, Crosslinked, and Alkylated Electrolyte Films

S. E. Sloop, and M. M. Lerner

Department of Chemistry and Center for
Advanced Materials Research
Oregon State University
Corvallis, Oregon 97330

J. Electrochem. Soc. **1996**, *143*, 1292.

5.0 **Abstract.**

The formation and stabilities of interfaces between poly[oxymethylene oligo-(oxyethylene)] (PEM)-salt complexes and lithium metal or LiC_x are investigated. The Li / $PEM_{25}LiClO_4$ interface demonstrates behavior consistent with the formation of a solid electrolyte interface (SEI), with a stable interfacial resistance of 900 Ω cm^2 at 50° C. UV-crosslinked films do not form a stable interface, and R_{int} rapidly increases to greater than 10^5 Ωcm^2. When crosslinked samples are treated with methyl iodide, hexamethyldisilazane/trimethylchlorosilane (HMDS/TCMS), or upon addition of the plasticizer polyethylene glycol dimethyl ether (PEGDME), R_{int} at 50° C stabilizes at approximately 2000 Ω cm^2. The complexes require a plasticizer to form a low impedance interface with LiC_x.

5.1 **Introduction.**

There are many desirable properties for materials to be employed as solid electrolytes in lithium or lithium-ion batteries, namely (1) a high cationic conductivity, especially at ambient temperature, (2) a wide window of electrochemical stability, and (3) mechanical stability and processability. In addition to these, the electrolyte must be compatible with Li or LiC_x, meaning that a stable, low-impedance interfacial layer forms upon contact. Polyether-salt complexes containing poly(ethylene oxide), (PEO), or poly[oxymethylene oligo-(oxyethylene)] (PEM), show a stable electrochemical window of approximately 4 V and, between ambient temperature and 120 °C, exhibit ionic conductivities close to those required for some applications. Polymer electrolytes (PEs)

have therefore been widely studied for use as lithium and lithium-ion battery electrolytes, and several strategies for enhancing conductivities have been examined [1-6].

Polyether-based PEs are known to react with lithium metal to form a layer that demonstrates classic Arrhenius behavior, suggesting conduction through a thin, highly resistive surface layer (a solid electrolyte interface or SEI) [7-10]. The impedance arising from this layer can be a significant component of the total cell impedance, and can therefore significantly diminish the useful energy derived from a cell. Full characterization of the complex structure and chemical composition of the polymer/Li interface remains elusive, although the components should include Li-alkoxides, oxides, hydroxides, and/or carbonates, as well as voids.

PEM is a completely amorphous polymer above ~10° C, as are the PEM-based electrolytes; therefore, these exhibit higher bulk conductivities below 80° C than semi-crystalline PEO-salt electrolytes [11-15]. Previous reports, however, did not find a stable interface to form between PEM and lithium metal [11]. We have reported on crosslinking PEM films by irradiation with ultraviolet light in the presence of a photoinitiator [16].

PEs derived from UV- crosslinked PEM films show greatly enhanced mechanical stability. Since thin films ($< 10\ \mu m$) can be handled, and ionic conductivities are comparable to the linear PEM electrolytes, it is practical to form lower resistance electrolyte films with the crosslinked materials. There is evidence that the crosslink reaction mechanism follows the outline in Scheme 1 [17, 18]. Hydroxyl groups, arising from the hydrogen transfer to a radical precursor in step (2), are a by-product of the crosslink reaction. The presence of ROH may well affect the chemical stability of the

polymer toward metallic lithium or other anodes. This study will use impedance spectroscopy (IS) to explore the impedance and stability of the interfaces formed between the crosslinked films and typical anodes for battery applications, and to evaluate methods for controlling the interfacial reactions; an introduction to the theory, and assumptions used in the IS analysis will be treated within the experimental section.

5.2 **Experimental.**

PEM was synthesized via a Williamson condensation [13, 14], and physical data obtained on the product and the commercial grade PEO (Aldrich) utilized are provided in Table 5.1. Polymer films with thickness ≈ 100μm were prepared by air drying a viscous CH_3CN (Mallinkrodt, spectroscopic grade) solution within glass-ring supports on a Teflon mat. The films were loaded into quartz tubes and irradiated with 254 nm light under an argon atmosphere. Following the reaction, films of crosslinked PEM (XPEM) were rinsed three times with acetone (Mallinkrodt, spectroscopic grade) to remove residual linear polymer and low-molecular-weight fragments. Dimensional analysis and use of the Flory-Rehner equation[19] indicate an average crosslink density of 5 mol % for the prepared films. GPC analyses on soluble (linear) polymer samples were obtained using aqueous solutions and a series of 2 linear hydrogel columns (Waters). Thermal transitions were observed using a Shimadzu DSC-50Q analyzer fitted with a low temperature attachment.

5.2.1 Methylation, and Silylation of Alcohols

Treatment of crosslinked polymers with silylating, or alkylating groups was accomplished under the assumption that hydroxyl groups exist on the polymer-film surface as a result of radiation crosslinking; these hydroxyls were not observable using standard spectroscopic techniques.

5.2.1.1 *Methylation* [20]

Before methylation of XPEM, the reaction was studied with PEG 400. Methyl iodide (Aldrich, 5 mL, spectroscopic) and finely ground KOH (Mallinkrodt, analytical reagent, ~1 g) were placed into a test tube contained in an icebath, and PEG 400 (Aldrich, reagent, 0.5 g, vacuum dried) was added to this mixture. The reaction proceeded quickly, vigorously producing heat. After five minutes, proton NMR spectra revealed ethoxy and methyl ether protons at 2.6, and 3ppm respectively, and in an intensity ratio of about 20:3, indicating that the methylation was quantitative.

Methylated, crosslinked PEM (MXPEM) was obtained by placing XPEM films into excess methyl iodide at ambient temperature in the presence of finely ground KOH. The swollen mass was soaked and gently agitated overnight under Ar, then filtered, air dried, washed in deionized water until the filtrate pH~7, and dried *in vacuo* for 24 h at 60 °C.

Methylated, linear PEM (MPEM) was obtained by mixing 2 g of PEM with excess methyl iodide in the presence of finely ground KOH. The reaction proceeded overnight, under nitrogen, in a Teflon™ beaker placed within a drying tube. The unreacted methyl

iodide was removed with a vacuum, and trap. The product was dialyzed (Dialysis, 2000 D pore size) against deionized water for 7 days. An average molecular weight of 50,000 D was determined with GPC analysis, and the sample had an increased polydispersity with respect to original PEM samples; indicating that some depolymerization occurred. The crosslinked films, and linear polymers do not have as great a concentration of hydroxyl, as does PEG400, therefore, their reactions did not display a tremendous production of heat.

5.2.1.2 ***Silyation*** [21, 22]

Silylation of PEG 400 was accomplished following Tørnquist's procedure [21]. A 50/50 v/v mixture of hexamethyldisilazane/trimethylchlorosilane (HMDS/TMS) (Aldrich, reagent, 5 mL) was added to neat PEG 400 (1mL) at room temperature, and shaken for 5 minutes. The product phase separates after several hours, and its proton NMR displays peaks at 2.6, and 0 ppm corresponding with the ethoxy and methyl-silyl protons respectively; the intensity ratio of the ethoxy:methyl-silyl responses was about 4:1, indicating that the reaction was quantitative.

Silylated, crosslinked PEM (SXPEM) was obtained by an overnight reaction of XPEM with a 50/50 v/v mixture of TMCS and HMDS. Purification of the treated polymer was accomplished by washing three times with acetonitrile (from the bottle, Mallinkrodt, spectroscopic). The NMR analysis of SXPEM in $CDCl_3$ (without tetramethyl silane) detected a weak signal corresponding with silyl-methyl protons at 0ppm.

Linear PEM was similarly treated with the silylating agents and purified as described above. The polymer experienced a similar loss in average molecular weight and polydispersity.

5.2.2 **Preparation of PEs**

PEM-salt electrolytes were prepared with a stoichiometry of etheric O:Li = 25:1 (or 15:1 for PEO) by co-dissolution or salt imbibition from a solution of $LiClO_4$ (Aldrich reagent, dried *in vacuo* at 200 °C for several days) in CH_3CN (distilled from CaH_2). The resulting salt complexes were dried *in vacuo* and stored in a dry argon atmosphere. Where noted, 10 wt% polyethylene glycol (400) dimethyl ether (PEGDME) (Fluka, spectroscopic grade) was added as a plasticizing agent.

Symmetrical $Li/PEM_{25}LiClO_4/Li$ cells were constructed under an Ar atmosphere by pressing 1 cm^2 Li (Aldrich, 99.999%) discs against the polymer film. A modified C-clamp was used to maintain contact between electrodes and electrolyte, and the cells were sealed into a 1 L Nalgene container containing Li metal as getter. The entire apparatus was placed into a drying oven purged with Ar at 50°C.

Impedance spectroscopy was performed using a Solartron 1260 impedance analyzer with a computer-controlled oven/cooler, a 100 mV sinusoidal exciting potential was applied from 10 MHZ to 5 MHz. DC potentiometry was performed on a PAR 362 Scanning Potentiostat. Cyclic voltammograms were obtained using a 1cm^2 Pt disc working electrode, a concentric Li metal ring as reference, and a stainless steel disc as the

counter electrode. The SEI thickness was calculated using relationships derived elsewhere [11].

Impedance data can be dependent on the excitation voltage employed. Table 5.2 indicates data obtained on a test cell using 0.01, 0.1, and 1V excitation voltages. Some variation in interfacial responses occurs at 0.01 and 0.1 V, although the product of the interfacial resistance and the frequency maximum is nearly constant. The interfacial response is more strongly correlated to higher excitation voltages, as demonstrated in agreement with the DC experiments. For consistency, and to allow a reasonable comparison of different cells, an excitation voltage of 0.1V is employed in all impedance measurements described.

Reduced graphite for LiC_x electrodes was synthesized by reaction of a lithium naphthalide / THF (Mallinkrodt, spectroscopic grade) solution with synthetic graphite (Aldrich, 99.99%, avg. part. size < 2μm, dried by heating to a red glow *in vacuo*) [23]. The solid product obtained was observed to produce H_2 gas upon reaction with water. The powder was pressed into 1cm^2 electrodes in an Ar/He drybox.

5.3 **Results and Discussion.**

A representative Nyquist plot obtained by impedance analysis (Figure 5.1a) for a newly-constructed cell (Li / $PEM_{25}LiClO_4$ / Li at 25 °C) shows a high-frequency arc for the bulk response along with a well-separated, low-frequency arc for the interfacial response. These data are modeled with the equivalent circuit provided in the Figure 5.1a, which consists of two parallel (RC) circuits in series. The first RC circuit corresponds

Polymer	Average MW / D	T_g / °C	T_m / °C
PEM	6.5×10^4	- 65	8
PEO	5×10^6	- 65	65

Table 5.1. Physical data for polyethylene oxide (PEO) and poly[oxymethylene oligo-(oxyethylene)] (PEM).

Excitation Voltage / V	R_{bulk} /Ω	$\omega_{max, bulk}$ / Hz	R_{int} / Ω	$\omega_{max, int}$ / Hz
0.01	520	2 M	9000	30
0.1	470	3 M	6700	40
1.0	400	4 M	1200	400

Table 5.2. Impedance data obtained at excitation voltages of 0.01, 0.1, and 1.0 V for a $Li/PEM_{25}LiClO_4/Li$ cell at ambient temperature.

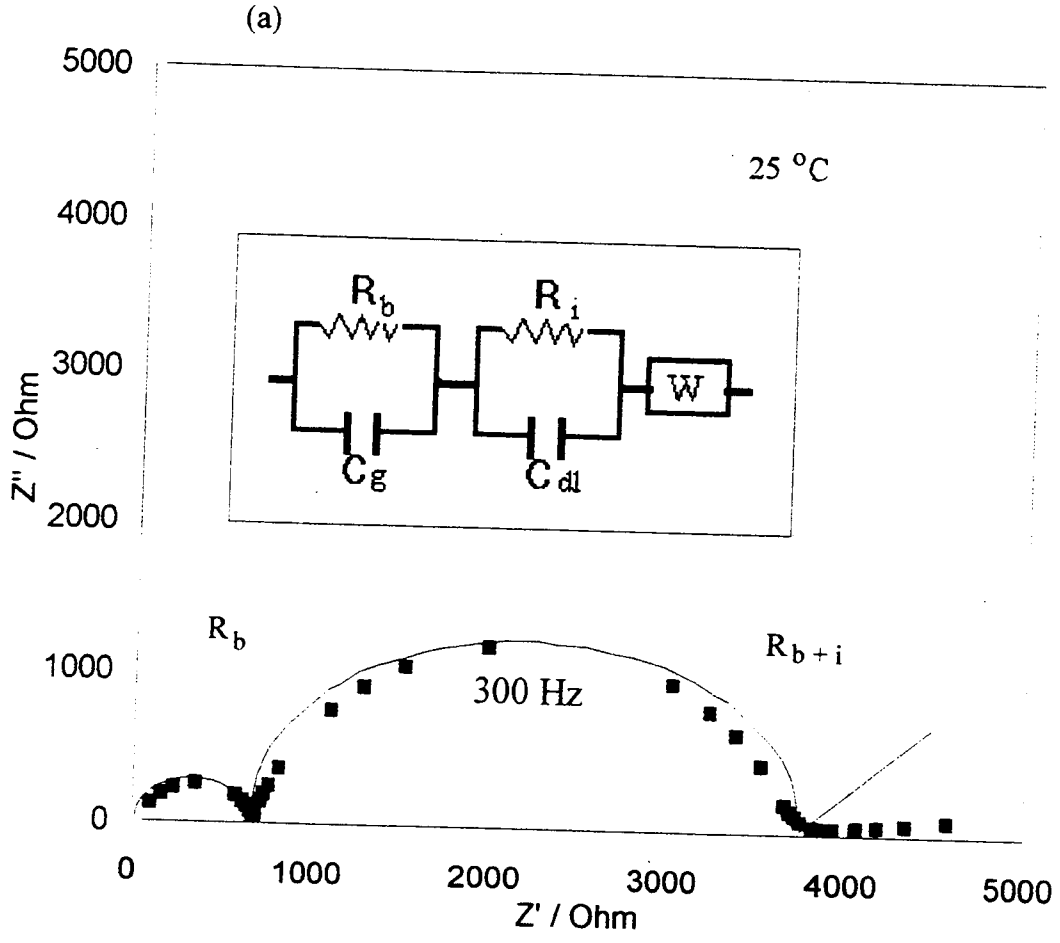

Figure 5.1. Nyquist plots and equivalent circuits for (a) $PEM_{25}LiClO_4$ and (b) $SXPEM_{25}LiClO_4$. The inset in (b) is magnified to show the bulk response, the fit parameters are: R_b=2300 Ω, Q= $1.1x10^{-8}$, and n = 0.7, (n = 1 for perfect capacitance).

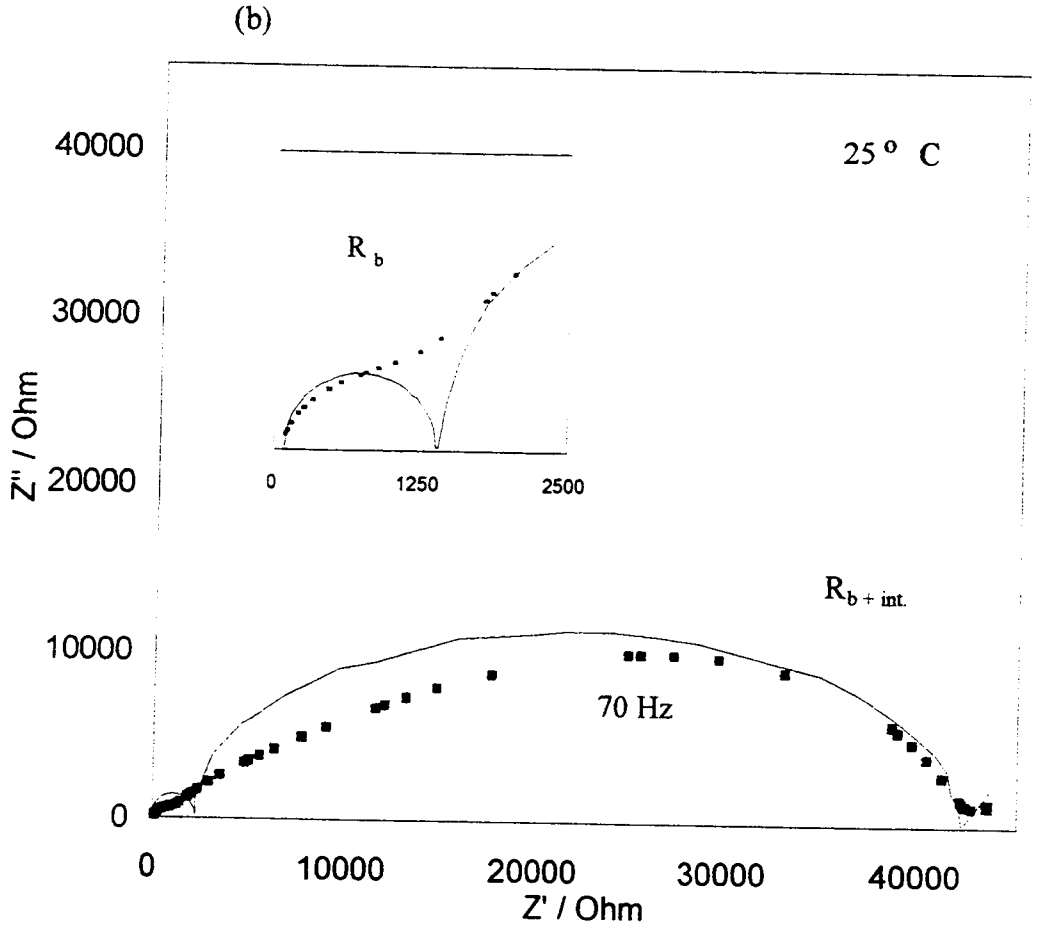

Figure 5.1 Continued

with bulk responses and, the second one to interfacial responses. The Warburg element represents low frequency ion diffusion [24]. As a method test, R_{int} for $Li/PEO_{15}LiClO_4$ was evaluated and found to stabilize at 100 Ωcm^2 at 70 °C, which agrees well with observations from other laboratories [25]. Similar Nyquist plots are obtained for the XPEM and MXPEM samples. The bulk responses using thin films of the crosslinked samples overlap the interfacial response, but are reproducibly modeled when a constant phase element (CPE) replaces C_g to allow for flattening of the bulk impedance arc [26]. This non-ideal bulk response is believed to arise as a consequence of the heterogeneous distribution of crosslink sites in the bulk polymer; consistent with observations of photochemical processing primarily producing crosslinks near the film surfaces.

The total cell resistance can also be monitored by dc measurement. The current vs. voltage curves displayed in Figure 5.2 show an approximately linear response for a cell 4 and 15 days after construction, with the change in slope indicating an increase in R_{cell}. As $R_{cell} = R_{int} + R_{bulk}$, the method is most useful when $R_{int} >> R_{bulk}$ (and therefore $R_{cell} \approx R_{int}$), a condition met in most of these cells. In these studies, R_{bulk} is generally $\approx 100\Omega cm^2$, with R_{int} at least an order of magnitude higher. Where AC and DC measurements are both obtained, there is agreement between the methods.

An Arrhenius plot of these data provided in Figure 5.3 shows the different thermal responses obtained for bulk and interfacial processes. The interfacial response is linear over the temperature range studied: the bulk response gently curves, indicating the influence of polymer dynamics on ionic transport that is described by the VTF equation [15, 27]:

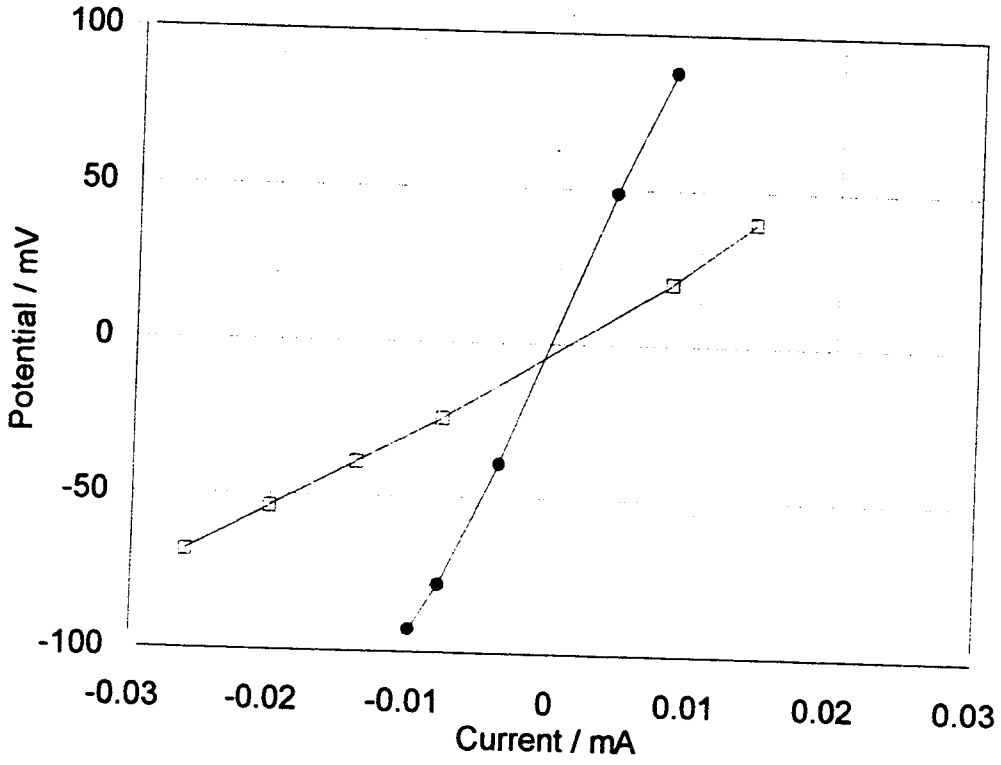

Figure 5.2. V vs. I for $XPEM_{25}LiClO_4$ /Li after (□) 4 days, and (●) 15 days. The slope of these plots provides R_b+R_{int} .

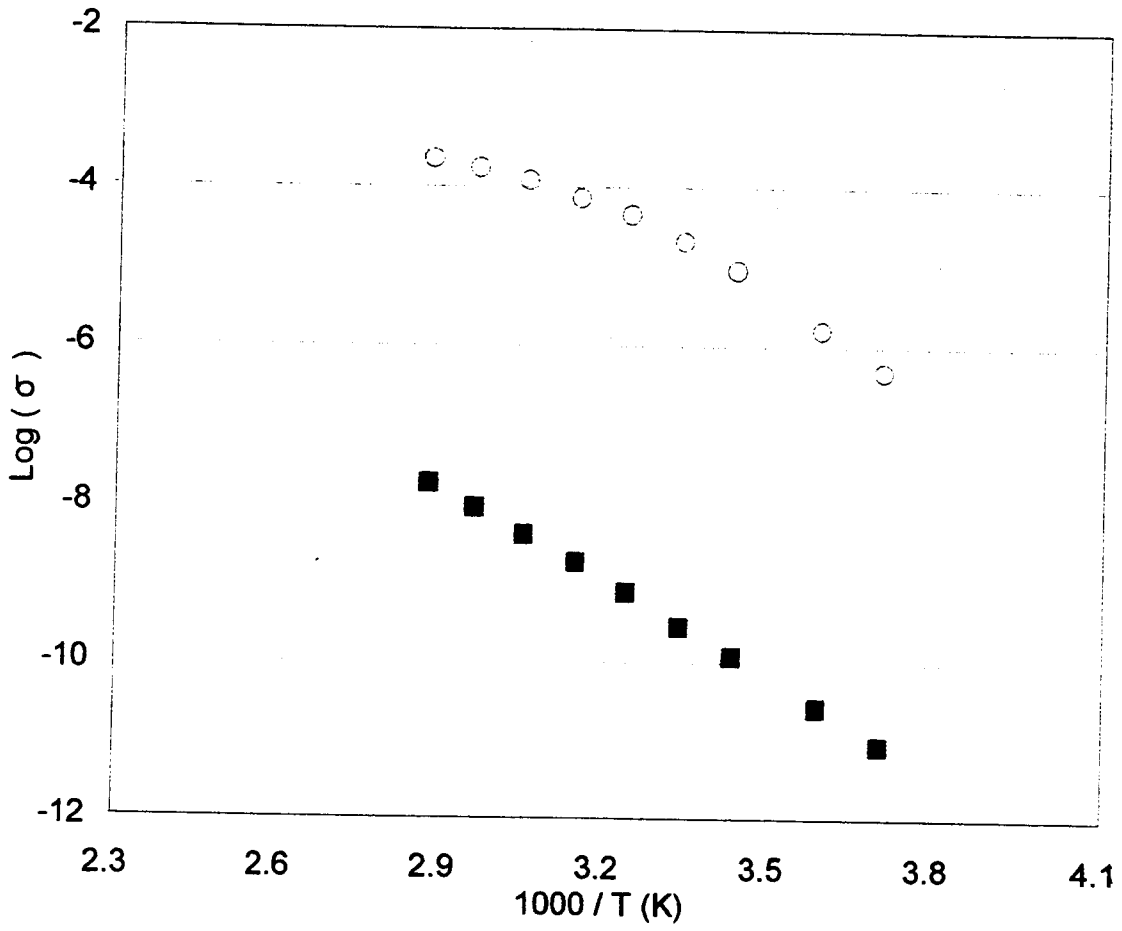

Figure 5.3. Arrhenius plot of (○) bulk conductivity, and (■) SEI conductivity in $PEM_{25}LiClO_4/Li$. The solid lines represent best fits using the VTF and Arrhenius equations for (a) and (b), respectively.

$$\sigma = A' T^{-1/2} e^{[-B'/k(T-T_0)]} \quad (5.1)$$

The bulk conductivities for PEM and XPEM-based electrolytes have been previously reported to be similar [16], which extends to the MXPEM, SXPEM and the plasticized polymer electrolytes (Figure 5.4). The range of conductivities for all these complexes is within a half-order of magnitude at ambient temperature, with the linear PEM complex exhibiting the highest, and SXPEM complex the lowest, conductivity.

Results of fitting the bulk conductivities to the VTF equation using the three parameters T_o (the equilibrium glass transition temperature, which should be 25 - 50 °C below T_g), B' (a pseudo-activation energy), and a pre-exponential term, A' (associated with the number of charge carriers), are presented in Table 5.3. Curve fitting is accomplished by varying the parameters established for the linear PEM salt complexes, first A' and then B' and/or T_o is optimized. The B' values obtained are essentially constant, so the change in conductivities is primarily accounted for by a decrease in A' in the crosslinked samples. The fits obtained also agree with those found previously in studies on PEM - sodium salt electrolytes [14, 15].

The interfacial responses of the electrolyte films investigated demonstrate Arrhenius behavior (Figure 5.3), which is consistent with formation of a solid electrolyte layer (SEI) in which ionic conduction occurs via a hopping mechanism [28]. Values for A and E_a are obtained by a fit to the Arrhenius equation:

$$\sigma = A e^{(-E_a / kT)} \quad (5.2)$$

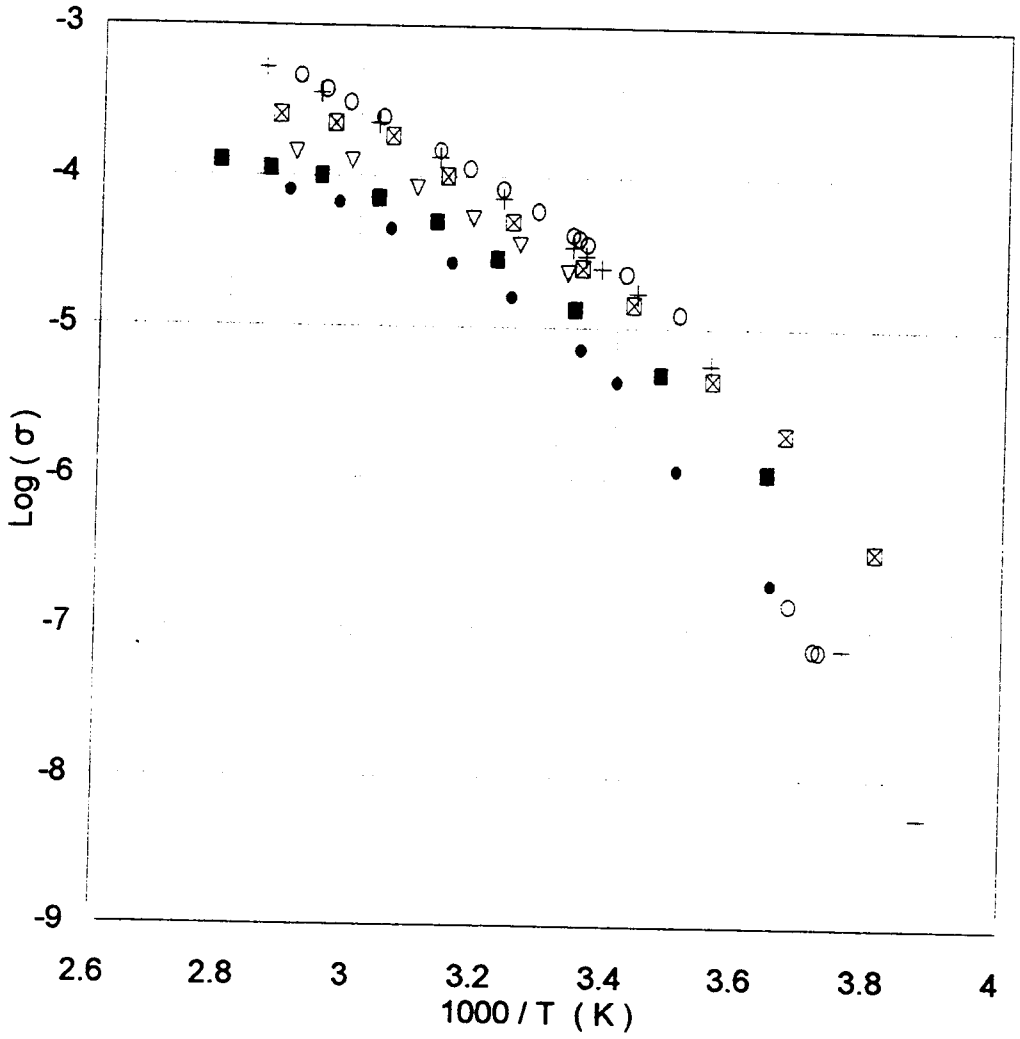

Figure 5.4. Arrhenius plots of bulk conductivity for electrolyte films based on (○) PEM, (+) MPEM, (⊠) XPEM+PEGDME, (▽) MXPEM, (■) XPEM, and (•) SXPEM. All electrolytes are $LiCLO_4$ complexes with O:Li::25:1.

Sample	A' / S $K^{-1/2}$ cm^{-1}	B' / eV	T_o / K
PEM	14	0.11	171
MPEM	14	0.11	181
XPEM + PEGDME	13	0.11	186
MXPEM	4.5	0.11	165
XPEM	4	0.11	170
SXPEM	2.5	0.11	170

Table 5.3. VTF equation parameters obtained from fitting the data in Figure 4.

and provided in Table 5.4. Also provided in the table are values of the frequency maxima, ω_{max}, the estimated SEI thickness, ℓ, and the double layer capacitance, C_{dl} for the interfaces formed after 1 week.

The estimated SEI thicknesses range from 100 Å for PEO to 1300 Å for XPEM: the thicker interfaces are associated with higher resistance, lower capacitance, and lower ω_{max}. Also, these estimations of ℓ agree well with those calculated by Peled and coworkers [29].

The temperature chosen for stability tests (50 °C) is well above the melting transition for PEM complexes so that bulk conductivities are within the useful range for battery applications (above 10^{-4} Scm^{-1}). At this temperature, thin, self-supporting crosslinked films can have bulk resistances as low as 10 Ωcm^2. A low melting transition temperature is an advantage for PEM-based complexes as PEO-based complexes generally do not display such conductivities below 70°C.

The temporal change in interfacial impedance corresponds to the growth of a resistive layer (SEI) between the lithium and the polymer electrolyte. Figure 5.5 indicates changes in R_{int} over time for each electrolyte film. The PEM complex forms a stable interface with $R_{int} = 900\Omega cm^2$ within 2 days. As is evident from Figure 5.6, R_{int} is strongly temperature dependent, and drops to about 150 Ωcm^2 when the temperature is raised to 70°C. This value is twice that of $PEO_{15}LiClO_4$ at the same temperature, i.e., the PEM complexes form a more resistive SEI than PEO complexes at temperatures exceeding the T_m for the PEO complexes. The difference in stabilities between these two polymer-salt complexes may be related to differences in molecular weight, or may derive from the

Sample	A S cm^{-1}	E_a eV	ω_{max} Hz	R_{int} Ω cm^2	ℓ Å	C_{dl} μF /cm^2
MPEM	9000	0.34	1000	1700	560	0.023
SXPEM	6000	0.34	700	2000	900	0.0092
XPEM	2500	0.34	100	17000	1300	0.0084
MXPEM	1800	0.34	300	2500	620	0.018
PEM	-	-	700	1000	389	0.16
PEO*	-	-	5000	100	119	0.35

* Values were obtained at 70°C.

Table 5.4. Data and calculated parameters for cells one week after construction. The pre-exponential factor, A, and activation energy, Ea, are obtained by fitting the data in Figure 5. The frequency of impedance arc maxima, ω_{max}, double-layer capacitance, C_{dl}, interfacial resistance, R_{int}, are derived from impedance data. The layer thickness, $\ell = \omega_{max} \varepsilon_0 \varepsilon_r R_{int} A$.

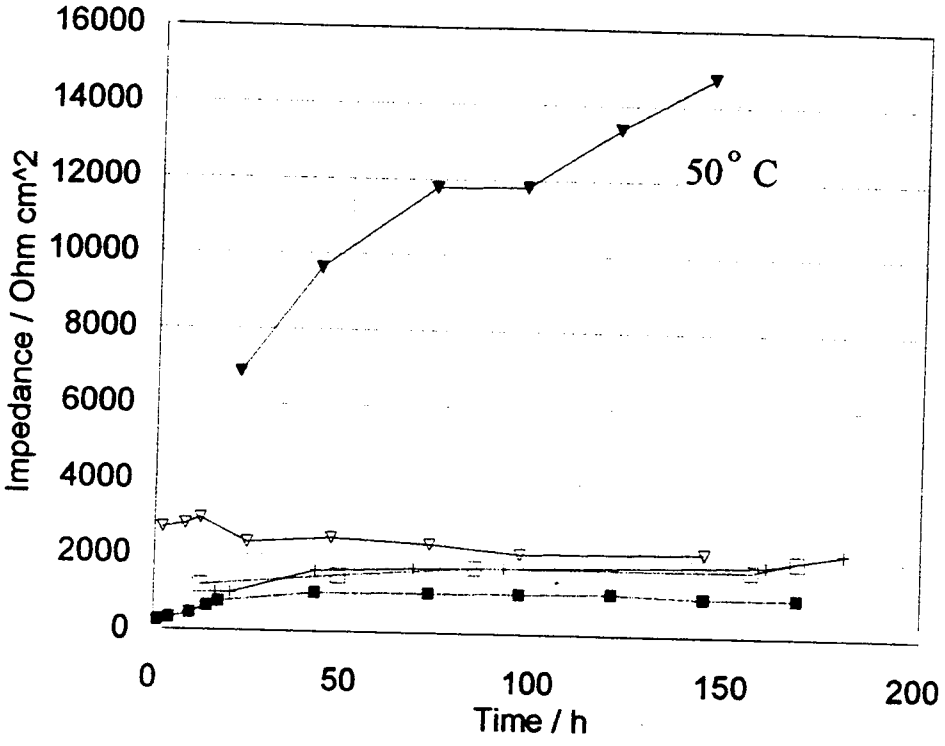

Figure 5.5. (a) R_{int} vs. time for electrolyte films based on (▼) XPEM, (▽) MXPEM, (+) SXPEM, (□) XPEM + 10% PEGDME, and (■) PEM. All electrolytes are $LiCLO_4$ complexes with O:Li::25:1. (b) R_{int} vs. time for $PEO_{15}LiClO_4$/Li.

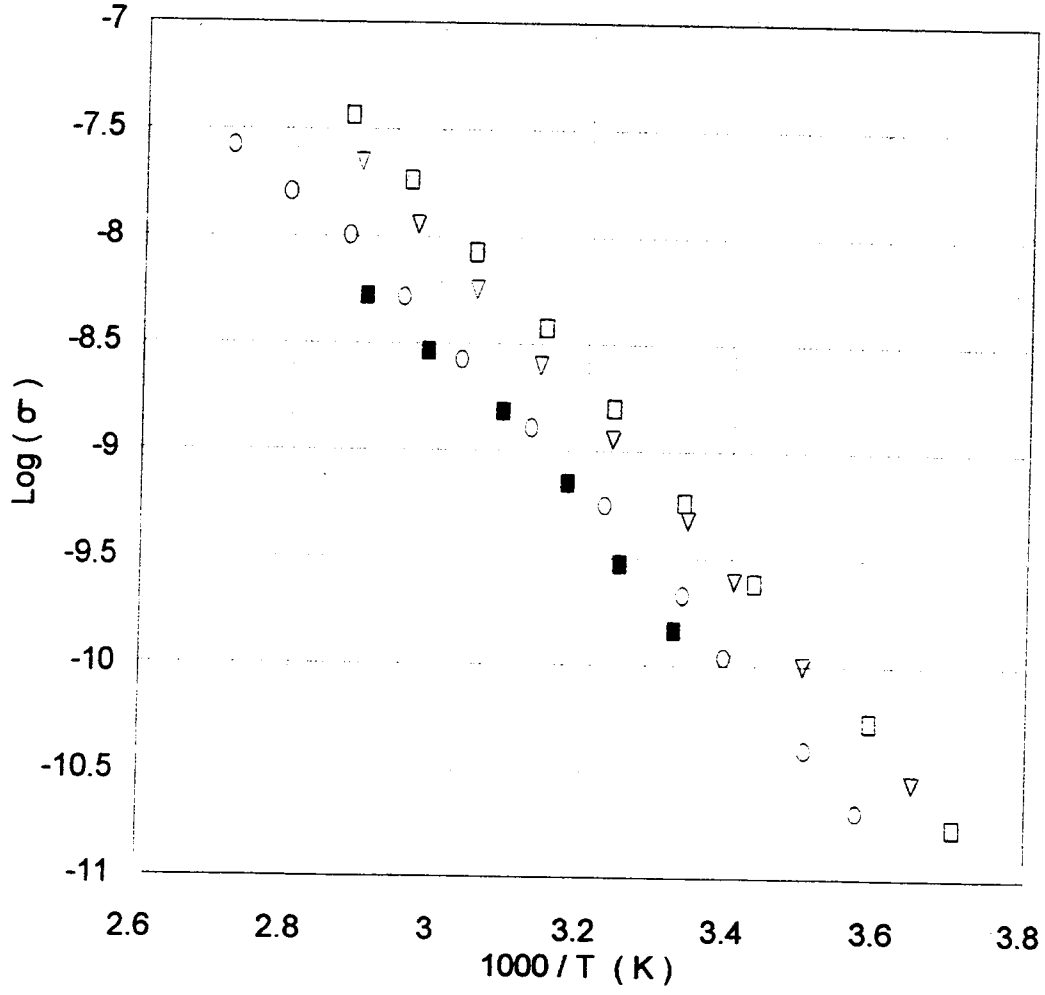

Figure 5.6. Arrhenius plot for the interfacial responses of electrolyte films based on (□) MPEM, (▽) SXPEM, (○) XPEM, and (■) MXPEM.

presence of oxymethylene links in the PEM chain. The O-Me-O unit should be somewhat less stable toward reduction than the oxyethylene moiety [30] and may therefore lead to a thicker SEI film and higher R_{int}.

The XPEM complex shows a much higher R_{int} which does not stabilize within one week. The highly-resistive SEI is expected to be an oxide or hydroxide layer developing from surface contact between Li and the hydroxyl moieties present in this electrolyte. Since the alkoxy and siloxy end groups are more resistant toward reduction [30], the films were exposed to a methylating or silylating agent and reexamined. MXPEM and SXPEM complexes show dramatically different behavior. Their R_{int} stabilizes within 2 days at about $2\times R_{int}$ for the linear PEM complexes.

An alternative method for decreasing R_{int} was the addition of the plasticizer PEGDME, although the addition of a plasticizer has detrimental effects on some electrolyte properties [31]. The interfacial impedance for the plasticized XPEM film is comparable to that of MXPEM.

The methylation reaction was also evaluated on the linear PEM polymer to determine whether the alkylation of hydroxyl end groups can improve the interfacial stability. These methylated (MPEM) complexes are found to exhibit essentially identical behavior to PEM with respect to SEI formation, although some differences in mechanical, and surface-wetting properties do exist. The average M_w of MPEM significantly decreases to 12 KD, with increased polydispersity. This indicats that polymer scission arises as a result of the HI byproduct from the methylation reaction. MPEM was observed

to wet polypropylene cloth much faster than PEM, which is likely a plasticizing effect resulting from scission products.

PEM, XPEM, and MXPEM electrolytes do not readily adsorb to a LiC_x electrode surface, all have R_{int} in the mega-ohm cm^2 range after annealing at 80 °C for 24 h. The MPEM complex forms a low impedance ($<1\Omega cm^2$), stable interface over the course of several days at 50°C, presumably due the presence of low MW fragments following methylation. As lower viscosity polymers are known to obtain a greater surface coverage, PEGDME was added to the crosslinked films. The plasticized films then rapidly form a conductive and stable interface, although, these cells short circuited due to electrolyte flow under pressure.

Voltammograms of the PEM and MXPEM-based electrolytes are shown in Figure 5.7. PEM and MXPEM films have approximately a 4V stability window, similar to that for PEO-based electrolytes [3]. The MXPEM film exhibits a dampened oxidative decomposition near 1 - 2 V as compared to PEM film. This effect is presumed to arise from the restricted motion in the crosslinked polymer chains, causing slower interaction of attached functionalities with the electrode surface. A cathodic current wave with an onset near -1V corresponds to reduction of ROH, and this feature is greatly magnified in experiments where PEG-OH is added to the electrolyte (5.7c).

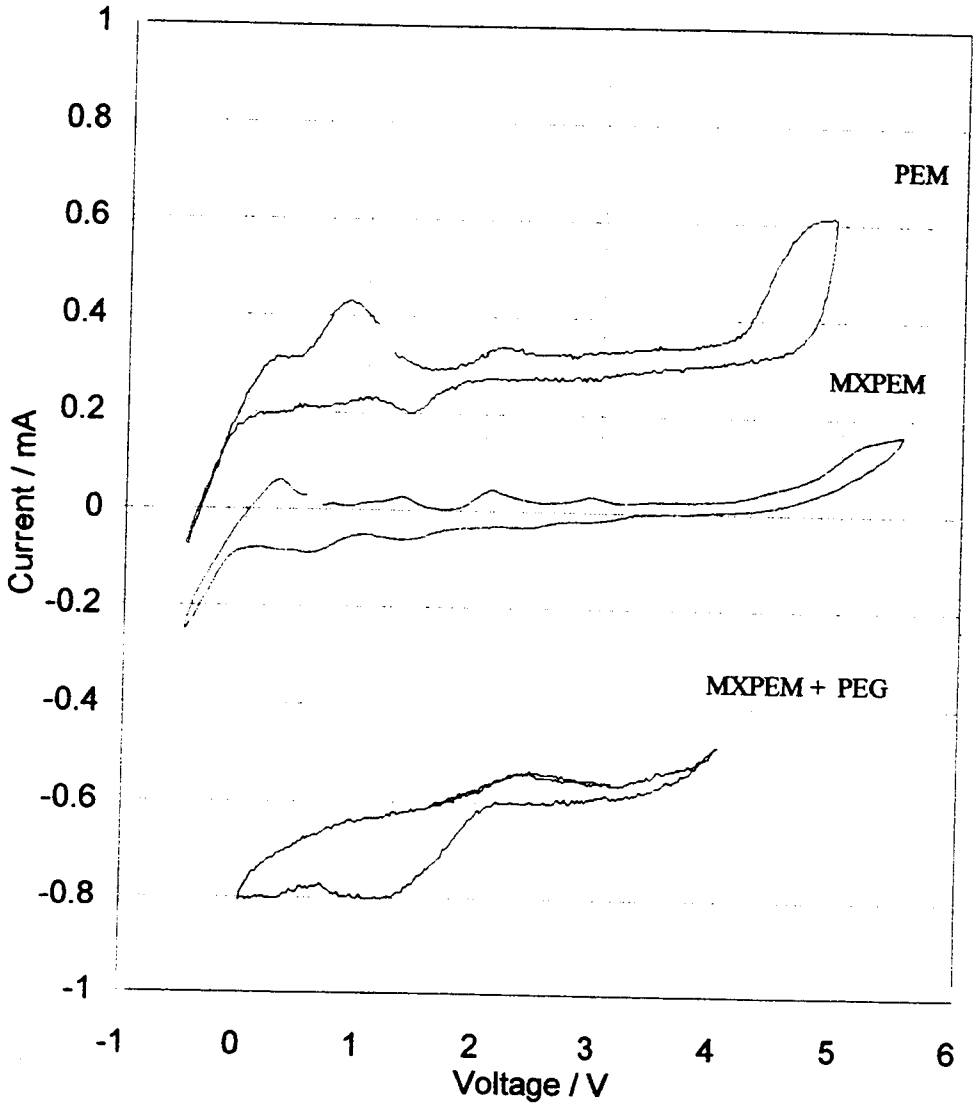

Figure 5.7. Voltammograms for $PEM_{25}LiClO_4$, $MXPEM_{25}LiClO_4$, and $MXPEM_{25}LiClO_4$ + 10 % PEG. Scan rates are at 10mV / s.

5.4 References.

1. Ratner, M., Shriver, D.F. *Chem. Rev.* **1988**, *88*, 109.

2. Gray, F. M. *Solid Polymer Electrolytes*, VCH: New York, 1991.

3. *Polymer Electrolyte Reviews-1* MacCallum, J. R.; Vincent, C. A. Ed.s, Elsevier Applied Science: New York, 1987.

4. *Polymer Electrolyte Reviews-2* MacCallum, J. R.; Vincent, C. A. Ed.s, Elsevier Applied Science: New York, 1989.

5. Shriver, D. F.; Bruce, P. G. in *Solid State Electrochemistry*, P.G. Bruce, Ed., Cambridge University Press: New York, 1995.

6. Bruce, P. G.; Gray, F. M. in *Solid State Electrochemistry*, P.G. Bruce, Ed. Cambridge University Press: New York, 1995.

7. Armstrong, R. D.; Todd, M. in *Solid State Electrochemistry*, P.G. Bruce, Ed., Cambridge University Press: New York, 1995.

8. Peled, E. *Proceedings of The Electrochemical Society* **1994**, *94-28*, 1.

9. Fauteux, D. *J. Electrochem. Soc.* **1988**, *135*, 2231.

10. Fauteux, D. *Electrochim. Acta* **1993**, *38*, 1199.

11. Murugesamoorth, K. A.; Owen, J. R. *Br. Polm. J.* **1988**, *20*, 227.

12. Linden, E.; Owen, J. R. *Br. Polm. J.* **1988**, *20*, 237.

13. Nicholas, C. V.; Wilson, D. J.; Booth, C.; Giles, J. R. M. *Br. Polym. J.* **1988**, *20*, 289.

14. Lemmon, J. P.; Lerner, M. M. *Macromolecules* **1992**, *25*, 2907.

15. Doan, K. E.; Heyen, B. J.; Ratner, M. A.; Shriver, D. F. *Chem. Mater.* **1990**, *2*, 539.

16. Sloop, S. E.; Lerner, M. M.; Stephens T. S.; Tipton, A. L.; Paull, D. G.; Stenger-Smith, J. D. *J. Appl. Polym. Sci.* **1994**, *53*, 1563.

17. Sonntag, C.; Schuchmann, H.; Schomberg, G. *Tetrahedron* **1972**, *28*, 4333.

18. Ivanova, T.; Melnikov, M.; Fok, N. *Dokl. Akad. Nauk SSSR* **1976**, *231*, 649.

19. Sperling, L. Ed., *Introduction to Physical Polymer Science* Wiley: New York, 1986.

20. Streitwieser, A. Jr.; Heathcock, C. H. *Introduction to Organic Chemistry - 2nd Ed.* Macmillan: New York, 1981, pp. 261-262.

21. Törnquist, J. *Acta Chem. Scand.* **1967**, *21*, 2095.

22. Pierce, A. E. *Silylation of Organic Compounds* Pierce Chemical Co.: Rockford, 1968.

23. Shu, Z. X.; McMillan, R. S.; Murray, J. J *J. Electrochem. Soc.* **1993**, *140*, 992.

24. Sørensen, P. R.; Jacobsen, T. *Electrochim. Acta* **1982**, *27*, 1671.

25. Gray, F. M. *Solid Polymer Electrolytes* VCH: New York, 1991, chapter 10.

26. Macdonald, J. R. *Impedance Spectroscopy* John Wiley & Sons: New York, 1978, pp.90-95.

27. Ratner, M. A. in *Polymer Electrolyte Reviews-1*, MacCallum, J. R.; Vincent, C. A. Ed.s Elsevier Applied Science: London, 1987.

28. West, A. R. *Solid State Chemistry and its Applications* John Wiley & Sons: New York, 1992.

29. Golodnitsky, D.; Ardel, G.; Peled, E. *Electronic Confrence on Solid Electrolytes*, Elsevier, 1995.

30. Streitwieser, A. Jr.; Heathcock, C. H. *Introduction to Organic Chemistry - 2nd Ed.* Macmillan: New York, 1981, p. 387. Compare the stability of HO-(CH_2CH_2-O)-H to HO-(CH_2-O)$_n$-H.

31. Gray, F. M. in *Polymer Electrolyte Reviews-1*, MacCallum, J. R.; Vincent, C. A. Ed.s, Elsevier Applied Science: London 1987.

A Comparison of two Interfaces: Nanocomposite $PEO_xLi_yMoO_3$/Polyether-Electrolyte and Li_xMoO_3/Polyether-Electrolyte

Chapter 6

6.0 **Abstract.**

Some characteristics of an interface between etheric-based polymer electrolytes and a nanocomposite of composition $PEO_xLi_yMoO_3$ are evaluated, and compared with those obtained using $LiMoO_3$. The interfacial impedance, and overall resistance of the cells composed of nanocomposite electrodes and a polymer electrolyte was less than cells composed of $LiMoO_3$.

6.1 **Introduction.**

Transition metal chalcogenides can be cathodically reduced by insertion of lithium cations (or other cations) within their structures. Such reversible behavior makes these solids candidates for secondary batteries [1]. Some of the layered structures within these solids, such as MoO_3, can be used as a host in the preparation of nanocomposites. Upon topotactic intercalation of with alkali metal ions, the MoO_3 layers of the host lattice are reduced, and the interlayer alkali metal ions provide charge balance to the solid, producing the nonstoichiometric compound which is known as a molybdenum bronze. This name derives from its metallic characteristics, such as high conductivity, which is thought to occur from the presence of delocalized electrons in the conduction band. The layer separations are small between the host lattice and the bronze, for example, lithium causes a layer separation of about 1.5 Å for $x = 0.5$ in Li_xMoO_3 ($0 < x < 0.5$).

The lithium bronze is a precursur to nanocomposites. In water, it can form colloidial dispersion, and when mixed with a solution of aquous polymer, such as polyethyelene oxide (PEO), a solid precipitates composed of polymer intercalated between the host lattice layers. Upon nanocomposite formation with PEO, MoO_3, and other layered solids incur an 8 Å expansion due to the intercalation of a double layer of the polymer [2]. The changes in the structure of MoO_3 upon formation of the bronze, and the nanocomposite with PEO are depicted in Figure 6.1

While structural changes are apparent in these nanocomposites, little work exists about their electrode performance with respect to the host material. Although, a recent ^{7}Li NMR study of $Li_x(PEO)_yV_2O_5$ shows mobile Li^+ ions that contribute to increased conductivity of the nanocomposite [3]. Investigations of the impedance response of V_6O_{13}/PE, or TiS_2/PE systems, as well as the V_6O_{13}/LE (liquid electrolyte), or TiS_2/LE systems show that an increase in the interfacial resistance, R_i, occurs over time, and may comprise a large portion of the overall cell resistance [4-8]. The liquid electrolytes, (propylene carbonate, ethylene carbonate), display a large capacity loss due to irreversible solvent intercalation into the cathode. Also, these investigations make no conclusions as to the presence of either a solid, or porous electrolyte interface (SEI, or PEI). This is, to our knowledge, the first known report about the interfacial behavior of a nanocomposite. This chapter describes the impedance reponse of the nanocomposite electrode, $PEO_xLi_yMoO_3$, when placed against polymer electrolytes (PEs) derived from $LiClO_4$ and polyethylene oxide (PEO), poly[oxymethylene- oligo(oxyethylene)] (PEM), or polyethylene glycol di-methyl ether 400 (PEGDME).

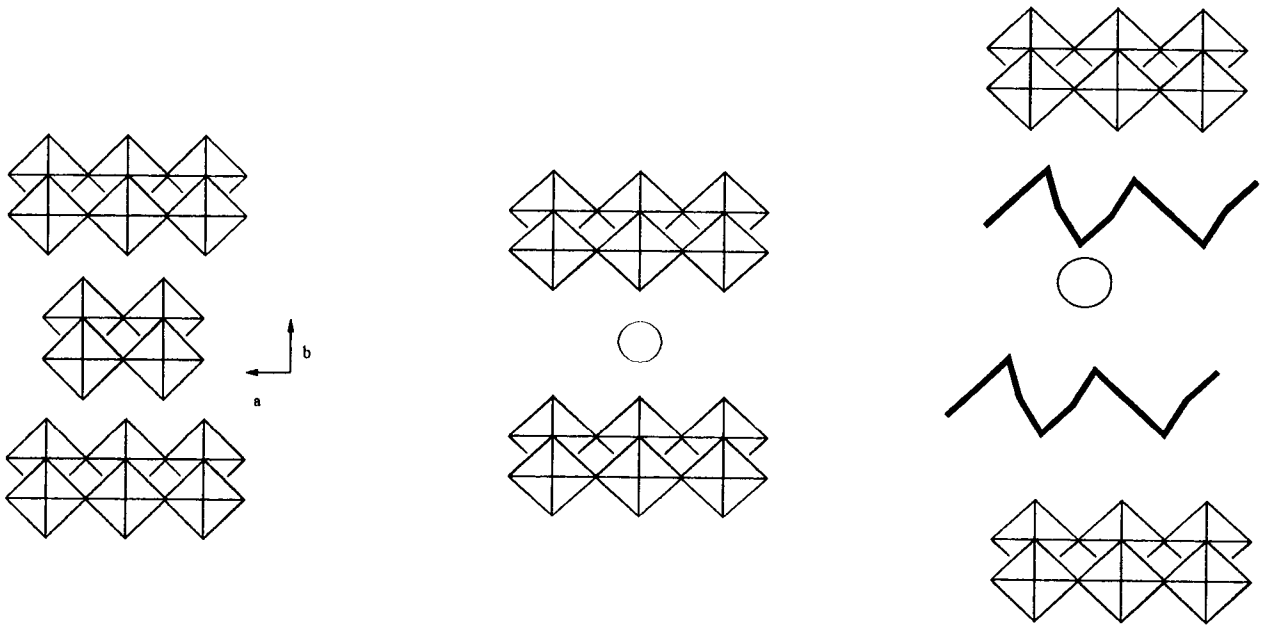

Orthorhombic MoO_3 $Li_{0.25}MoO_3$ $Li_xPEO_yMoO_3$

Figure 6.1. Structure changes of MoO_3 upon formation of the lithium bronze, and PEO nanocomposite.

6.2 **Experimental.**

6.2.1 **Nanocomposite synthesis.**

Li_xMoO_3 was prepared in a three-step process resembling the procedure outlined by Thomas, et al. [8]. The white starting material, MoO_3 (Aldrich, reagent, 5 g) was reacted with an aqueous solution of $Na_2S_2O_3$ (Aldrich, reagent, 1 M, 100 mL) and formed the black, sodium intercalated phase: $Na_{0.25}MoO_3$.

$$Na_2S_2O_4 + 4MoO_3 + H_2O \rightarrow$$

$$4\ (Na \bullet H_2O)_{.25}MoO_3 + Na^+ + SO_2^- + SO_{2(g)} \qquad (6.1)$$

Sonication at ultrahigh frequency for five minutes assisted in the dispersion of the solids, the reaction was stirred overnight, and then allowed to settle before decanting the supernatant. Subsequent washing with water removed excess sodium dithionite, and the side products, finally, the black product was dried *in vacuo*. X-ray diffraction (XRD) of $Na_{0.25}MoO_3$ indicated complete reaction by the absence of peaks associated with MoO_3.

Ion exchange of $Na_{0.25}MoO_3$ with lithium was accomplished by overnight stirring of the solid (1 g) with aqueous LiCl (Aldrich, reagent, 100 mL, 1 M). The mixture settled for several hours before the product was isolated by centrifugation. Sodium analysis by atomic absorption indicated that five repetitions of the ion exchange process reduced the sodium-ion content to $\leq$ 1 mol %. The stoichiometry is $Li_{0.25}MoO_3$ as determined in the work of Thomas, and its XRD shows no 020 peaks from the sodium phase (Figure 6.2).

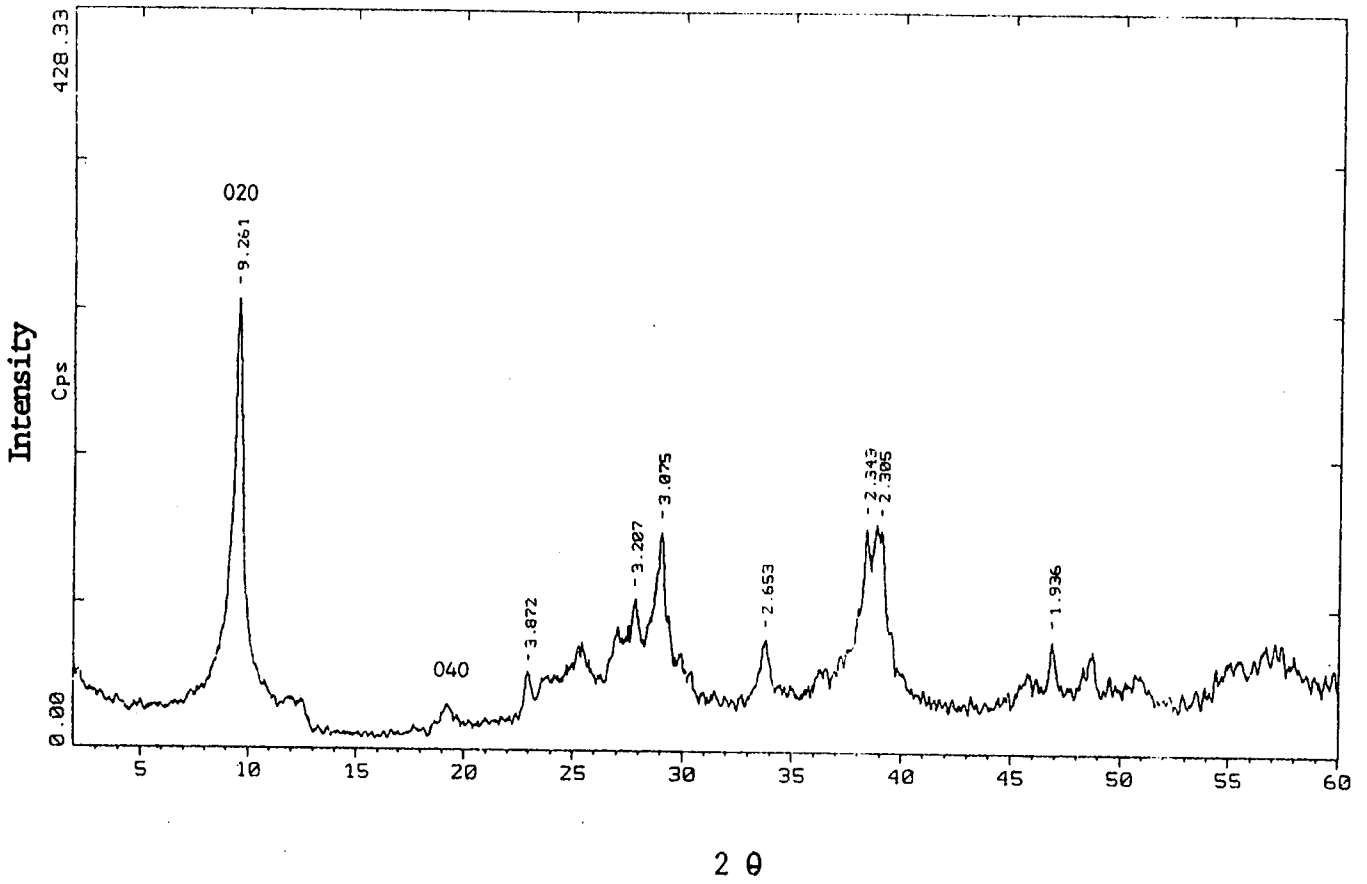

Figure 6.2. XRD pattern of $Li_{.25}MoO_3$. The 020 layers of this phase match with those reported by Thomas et al. The interlayer, 020, spacing of the sodium phase is absent (9.63Å) [8].

$Li_xPEO_yMoO_3$ nanocomposites were prepared with the exfoliation-absorption technique [2, 9]. Li_xMoO_3 was exfoliated by sonication in 50 mL of water. Afterward, and an aqueous solution of PEO (0.3 g in 60 mL) was added, and the reaction stirred overnight. Precipitation of the composite was aided by adjusting the reaction pH ~ 4, 5 with a few drops of 0.1 M aqueous HCl, followed by centrifugation. Finally, the product was rinsed with water and dried *in* vacuo. The $Li_xPEO_yMoO_3$ XRD pattern is displayed in Figure 6.3.

6.2.2 **Electrode Fabrication**.

The electrode consisted of a weight percent mixture of 54 % PEO (a binder), 4 % brij (Aldrich), 2 % carbon black, with the balance taken up by Li_xMoO_3. Other electrodes contained 50 % nanocomposite, 44 % PEO, 4 % brij, and 2 % carbon black. The PEO-lithium bronze nanocomposite was known to contain about 25 wt.% PEO from analysis of the thermogram in Figure 6.4.

Symmetrical cells were constructed for $Li_{0.25}MoO_3$ / PE / $Li_{0.25}MoO_3$, and $Li_xPEO_yMoO_3$ / PE / $Li_xPEO_yMoO_3$, where the polymer electrolyte is $PEO_{15}LiClO_4$, $PEM_{25}LiClO_4$, or $PEGDME_{15}LiClO_4$, all work was accomplished under an inert atmosphere in a drybox. The liquid electrolyte (PEGDME, Fluka, spectroscopic) and was mixed with dry $LiClO_4$, and saturated into Celgard 2400™ (linear, isotactic, polypropylene cloth, 0.1 mm thick) before use. All electrodes were discs measuring 1cm^2 in area.

After construction, the cells with solid PE's were contained in a modified C-clamp (Figure 6.5) and placed under Ar in an airtight container; the whole system was maintained

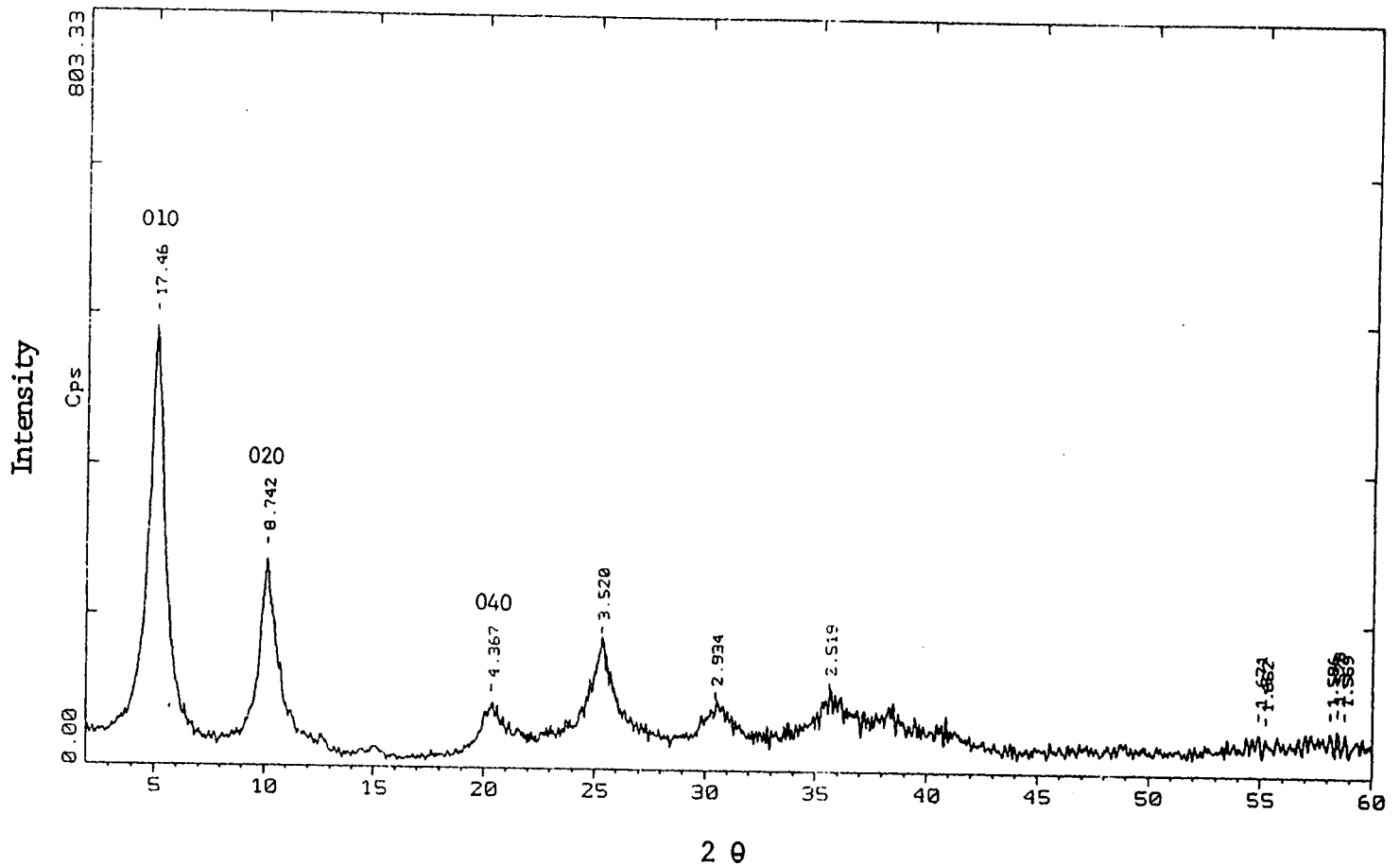

Figure 6.3. XRD of $Li_xPEO_yMoO_3$ shows multiple diffraction peaks 17.5Å. A bi-layer of PEO causes about an 8Å increase in the interlayer spacing [9, 2].

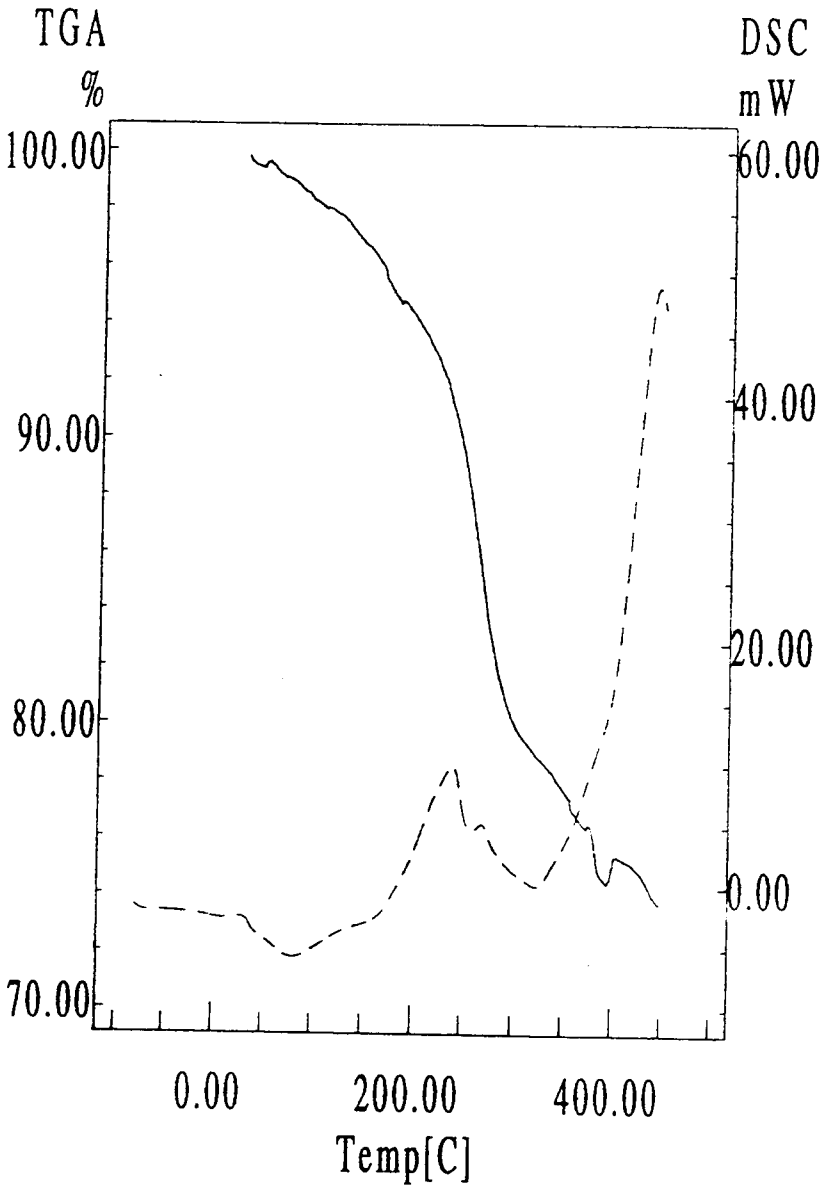

Figure 6.4. Thermal analysis of the degradation of $Li_xPEO_yMoO_3$ shows that the nanocomposite contains about 25 wt. % polymer.

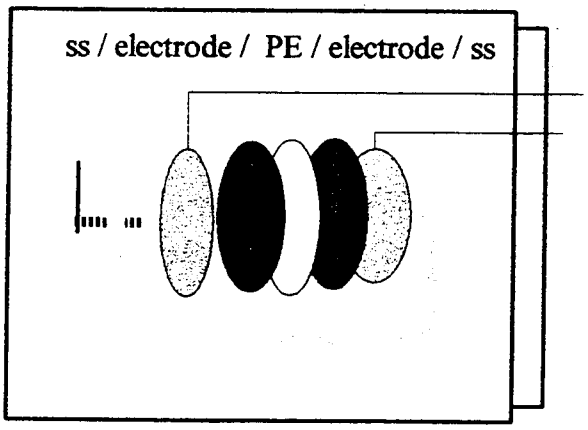

Figure 6.5. The modified C-clamp inside a Nalgene container. The "electrode" is $Li_xPEO_yMoO_3$, or $Li_{0.25}MoO_3$.

at 75°C in a dry N_2 atmosphere. The liquid electrolyte cells were placed into an air-tight Kel-F™ cell (Figure 6.6). The impedance of these cells was investigated with a Solartron Impedance Analyzer. Excitation voltages were varied between 0.01-1.0 V without a significant impedance change. Direct current experiments were performed upon these cells using a PAR potentiostat, voltage response to the applied current were recorded when the cell response stabilized after about 1 minute. After storage at 75°C for more than one week, these PEs appeared to decrease in viscosity, and their cells eventually short-circuited. The liquid electrolyte cell impedance remained stable for 2 months (when the apparatus was dismantled), and did not short circuit through the durable electrode separator.

6.3 **Results and Discussion.**

Nyquist plots of some representative cells are shown in Figures 6.7-6.12. The impedance analysis of these cathode/electrolyte cells do not provide well-defined interfacial and bulk responses as in the case of lithium metal/PEs. However, these impedance responses can be represented by an equivalent circuit shown in Figure 6.7, where the high frequency response represents the bulk resistance, R_b, of the electrolyte. The low frequency semicircle represents the interfacial resistance, R_i, between the electrolyte and cathode, finally, the ~45° low frequency spur is represented by the diffusion limited Warburg element. The expectations of this model are consistent with observations: R_b is dependent upon cell geometry (ie. R_b doubles with electrolyte thickness), and R_i is independent of cell geometry. The value of R_{b+i} agrees with the

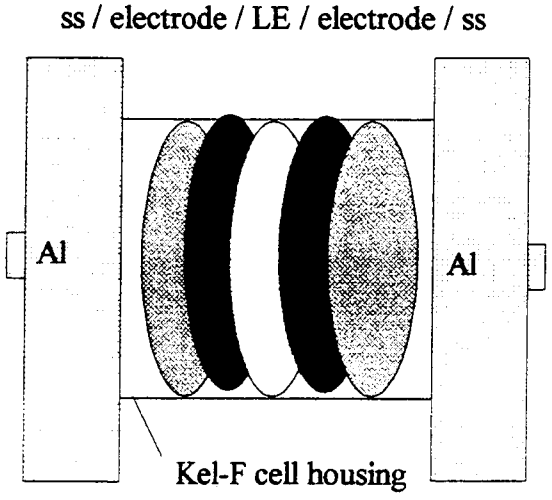

Figure 6.6. The Kel-F cell used to house the liquid electrolyte (LE). The "electrode" is $Li_xPEO_yMoO_3$.

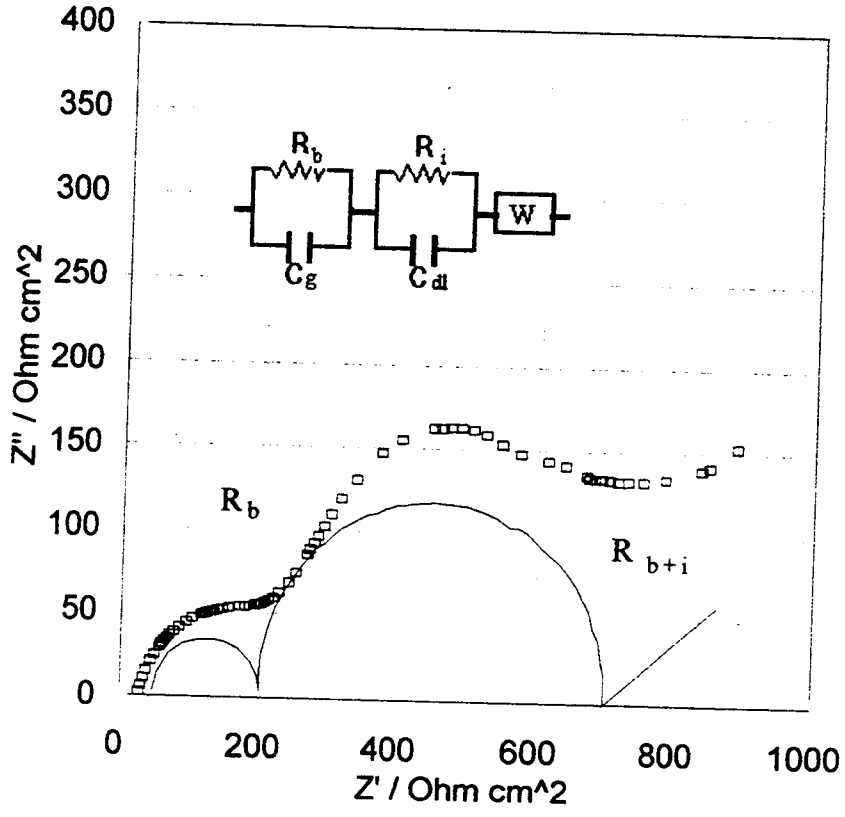

Figure 6.7. A Nyquist plot of $Li_xPEO_yMoO_3$ / $PEO_{15}LiClO_4$ / $Li_xPEO_yMoO_3$ (at 60° C) with an equivalent circuit. The bulk resistance is 200 Ω cm^2, and the interfacial resistance is 250 Ω cm^2.

overall-cell resistance measured in a DC experiment, which can be seen in comparison of Figures 6.12 and 6.13. Also, the change in R_b with temperature, seen in Figure 6.7, can be correlated with the conductivity of $PEO_{15}LiClO_4$. Finally, the double layer capacitances for these cells, shown in Table 6.1, are similar to other interfacial capacitances (0.001- 10 $\mu F\ cm^{-2}$) [10].

The Figure pair 6.7 and 6.9 reveal a difference between R_i for the nanocomposite, $Li_xPEO_yMoO_3$ and the host, $Li_{0.25}MoO_3$, against a PEO electrolyte. Figure 6.7 shows the $Li_xPEO_yMoO_3$/PEO R_i to be 250 $\Omega\ cm^2$. The R_i for the $Li_{0.25}MoO_3$/PEO cell is not directly observed in Figure 6.9, however, DC analysis revealed an overall cell resistance of about 20,000 $\Omega\ cm^2$, which can be used to calculate a representative value (10,000 $\Omega\ cm^2$). A similar trend in R_i values is observed between the $Li_xPEO_yMoO_3$/PEM, and $Li_{0.25}MoO_3$/PEM cells shown in Figure 6.10 and 6.11, where R_i = 750 $\Omega\ cm^2$, and 40,000 $\Omega\ cm^2$ respectively. The lower impedance values are time independent within the observation period (two weeks). The R_i values of control cells for the liquid electrolyte, however, appear to increase over time, which is consistent with other laboratories [5].

Table 6.1 summarizes R_i, ω_{max}, and C_{dl} for the cells shown in the Nyquist plots, where ω_{max} is the frequency at the interfacial semicircle maximum, and C_{dl} is the double layer capacitance. Large values of C_{dl} are known to correspond with high surface coverage between electrolytes and electrodes [10]. The $Li_xPEO_yMoO_3$/PEM interface has a larger C_{dl} than the $Li_{0.25}MoO_3$/PEM interface, which may indicate better adsorption, and fewer voids in the interface between soft, molten PEM electrolyte and polymer-coated nanocomposite. Upon heating the $Li_xPEO_yMoO_3$/ PEO cell shown in Figure 6.8*, C_{dl}

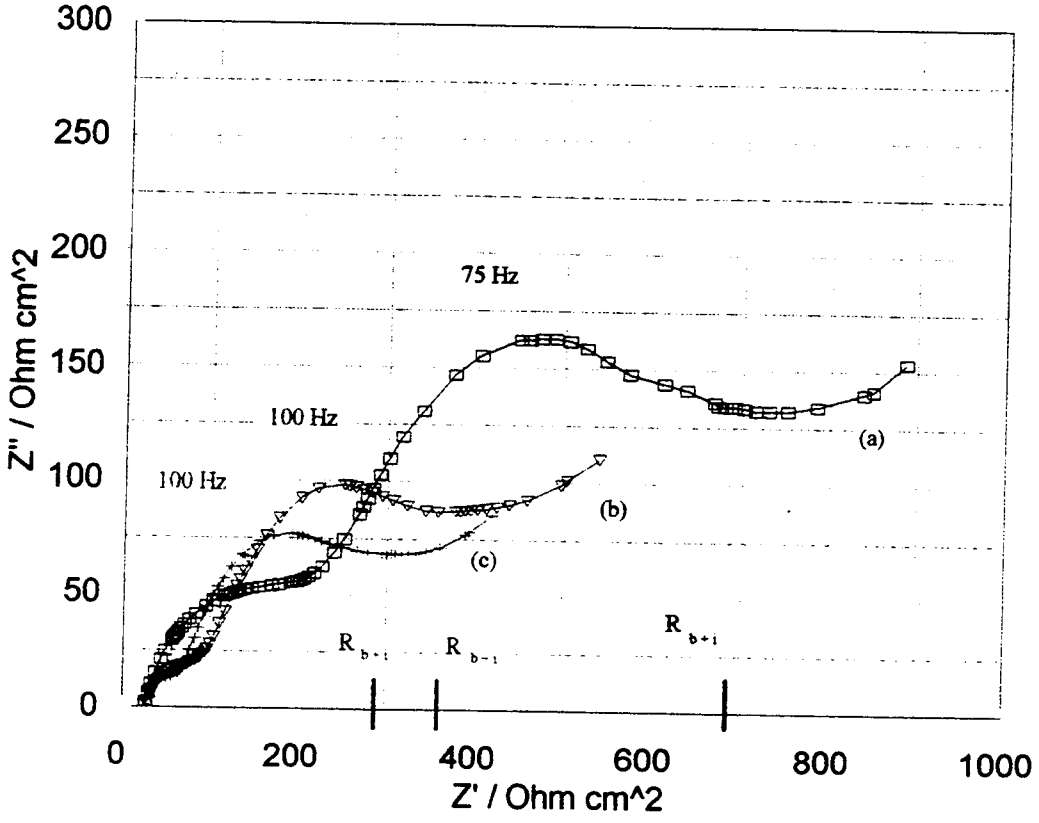

Figure 6.8. Nyquist plots of the cell in Figure 6.7 at (a) 60° C, (b) 70° C, and (c) 80° C. The frequency at maximum capacitance for each interfacial semicircle is provided on the graph.

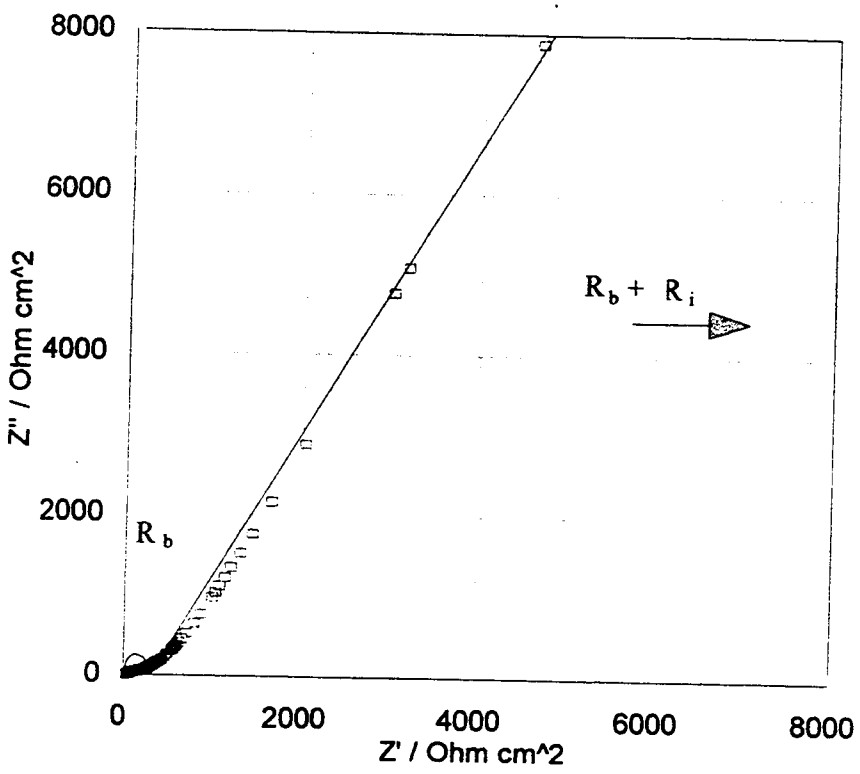

Figure 6.9. A Nyquist plot of $Li_{0.25}MoO_3$ / $PEO_{15}LiClO_4$ / $Li_{0.25}MoO_3$ at 60° C with an equivalent circuit model. The interfacial resistance is not observed with these frequencies (as low as 0.5 Hz), and is assumed to be much larger than R_i for the nanocomposite/PEO cell shown in Figure 6.7.

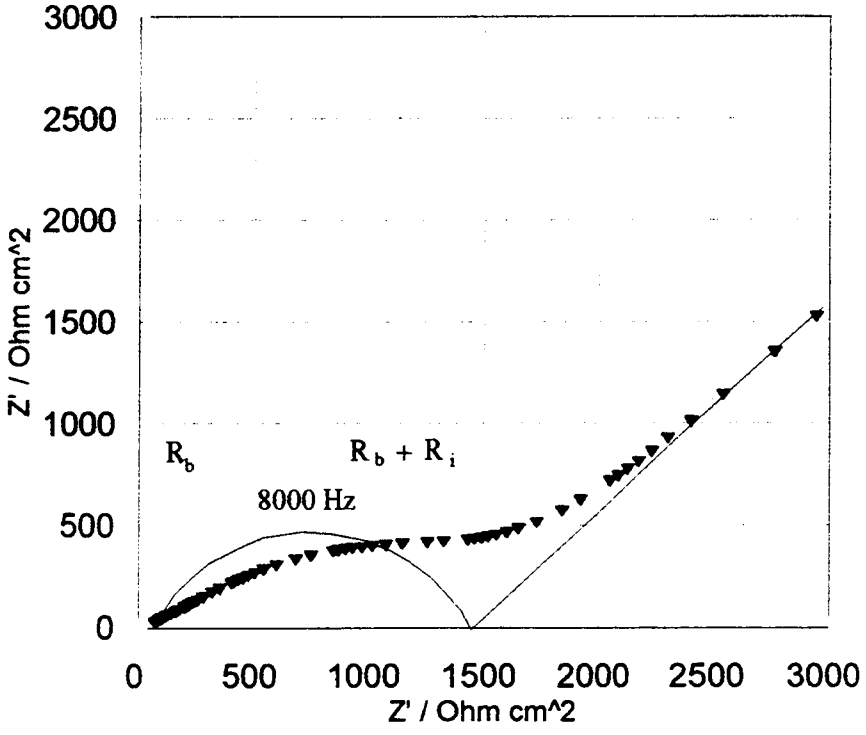

Figure 6.10. A Nyquist plot of $Li_xPEO_yMoO_3$ / $PEM_{25}LiClO_4$ / $Li_xPEO_yMoO_3$ at 50° C with an equivalent circuit model. The bulk resistance is about 100 Ω cm^2, and the interfacial resistance is 700 Ω cm^2.

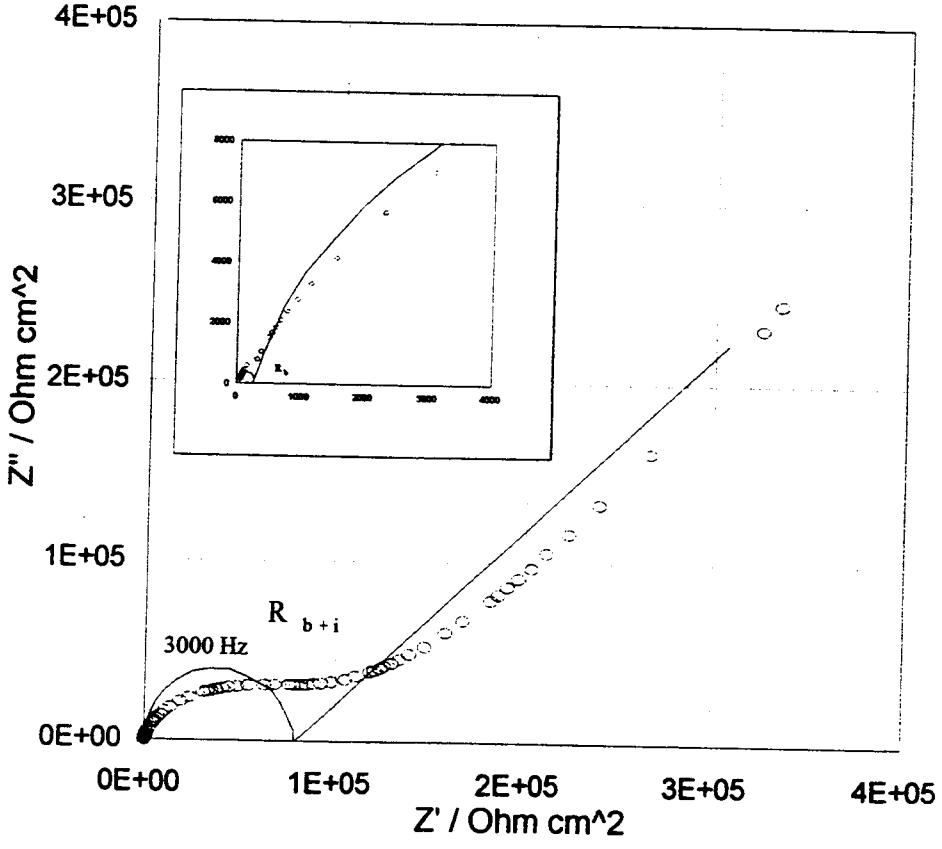

Figure 6.11. A Nyquist plot of $Li_{0.25}MoO_3$ / $PEM_{25}LiClO_4$ / $Li_{0.25}MoO_3$ at 50° C with an equivalent circuit model. The inset shows an enlargement of the high frequency end of the plot. The bulk resistance is about 100 Ωcm^2, and the interfacial resistance is about $4 \times 10^4\ \Omega\ cm^2$.

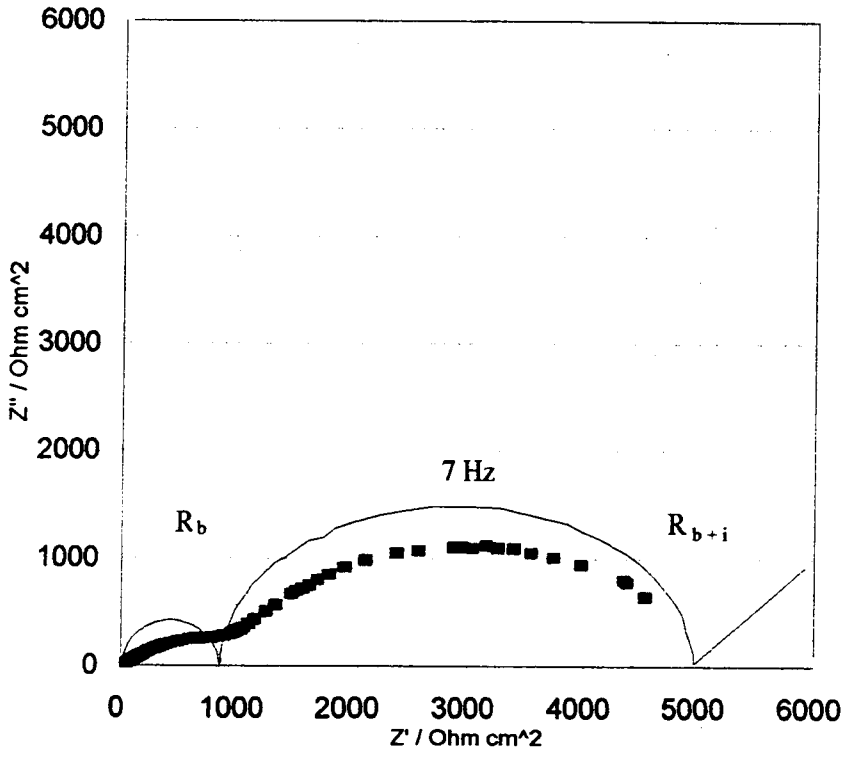

Figure 6.12. A Nyquist plot of $Li_xPEO_yMoO_3$ / $PEGDME_{15}LiClO_4$ / $Li_xPEO_yMoO_3$ at 50° C with an equivalent circuit model. The bulk resistance is 900 Ω cm^2, and the interfacial resistance is 2×10^3 Ω cm^2.

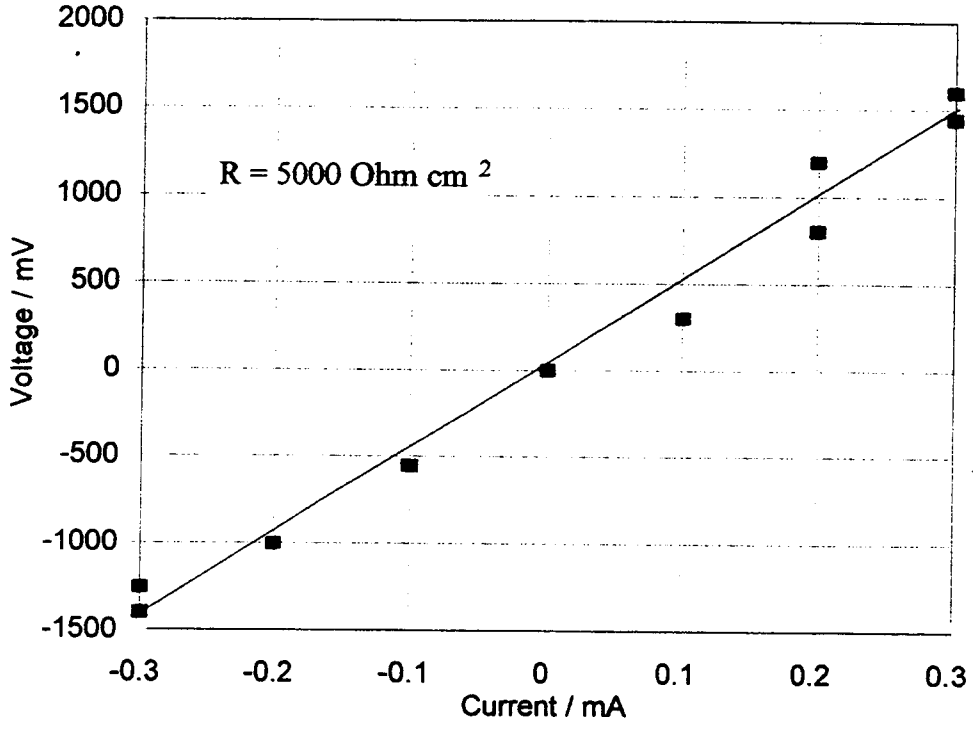

Figure 6.13. A V vs. I plot of $Li_xPEO_yMoO_3$ / $PEGDME_{15}LiClO_4$ / $Li_xPEO_yMoO_3$ for comparison with Figure 6.12. This demonstrates the general agreement between the overall cell resistance and the value of the low frequency minima in cell Nyquist plots. The overall cell resistance is $\Delta V/ \Delta I = 5000\ \Omega\ cm^2$, which is equal to R_{b+i}.

Cell	R_i / Ω cm^2	ω_{max} / Hz	C_{dl} / μF cm^{-2} *
PEO/Nanocomp. (60° C)	250	75	8.5
PEO/Nanocomp. (70° C)	130	100	12
PEO/Host (60° C)	~10,000	-	-
PEM/Nanocomp. (50° C)	750	8,000	0.027
PEM/Host (50° C)	40,000	3,000	0.0013
PEGDME/Nano. (50° C)	2,000	7	11

* $C_{dl} = (2\pi \omega_{max} R_i)^{-1}$

Table 6.1. Summary of interfacial resistances and capacitances.

increases, which is expected as the PE softens from 60-70° C, and achieves higher coverage of the electrode surface.

Curiously, the capacitances of the PEO electrolyte cells are higher than the PEM electrolyte cells, indicating greater coverage of the electrode/electrolyte interface in the PEO cell; the stiff, noncompliant nature of semicrystalline PEO (compared with amorphous PEM) may lead one to expect void formation at an interface and, therefore, low capacities [10]. These data indicate that the $Li_xPEO_yMoO_3$/PEO interface has higher degree of coverage than the $Li_xPEO_yMoO_3$/PEM interface.

The difference between R_i of the $Li_xPEO_yMoO_3$/PE and Li_xMoO_3/PE cells may be a result of two contributing factors. Firstly, faster charge-transfer kinetics in the nanocomposite may occur due to the increase in the MoO_3 host layer separation. Finally, high coverage of $Li_xPEO_yMoO_3$ with PE should produce a low impedance interface in comparison to the control cell. This may result from the chemical similarity of the PE and the $Li_xPEO_yMoO_3$ surface, which is likely to contain adsorbed polymer.

The nanocomposite structure may lead to a monolayer of adsorbed polymer that separates the electrode from the electrolyte, therefore a polymeric electrode/electrolyte interface may be expected, where the empirical difference between the transport properties of bulk and adsorbed PE are expressed within R_b and R_i. The time independence of R_i for these interfaces may indicate that bulk PE next to this chemically similar monolayer remains stable, which is expected, as the polymeric composition within pure $Li_xPEO_yMoO_3$ does not change over time. As in other investigations [5], Arrhenius plots derived from R_i are not provided because of the small temperature range in which R_i can

be observed. Therefore, the nature of conductance (classic Arrhenius vs. VTF behavior) at the interface remains inconclusive.

6.4 **Conclusion.**

Contact between PEs and a nanocomposite cathodic material, $Li_xPEO_yMoO_3$, results in a low impedance electrode/electrolyte interface compared with those formed with the native cathode material, $Li_{0.25}MoO_3$.

6.5 **References.**

1. Scrosati, B. in *Electrochemistry of Novel Materials* Lipkowski, J.; Ross, P. N. Eds., VCH: New York, 1994, chapter 3.

2. Lemmon, J. P.; Wu, J.; Oriakhi, C.; Lerner, M. M. *Electrochim. Acta* **1995**, *40*, 2245.

3. Liu, Y.-J.; Schindler, J. L; DeGroot, D. C.; Kannewurf, C. R.; Jirpo, W.; Kanatzidis, M. G. *Chem. Mater.* **1996**, *8*, 525.

4. Steele, B. C. H; Lagos, G. E.; Spurgens, P. C.; Forsyth, C. Foord, A. D. *Solid State Ionics* **1983**, *9/10*, 391.

5. Bruce, P. G.; Krok, F. *Electrochim. Acta* **1988**, *33*, 1669.

6. Bruce, P. G.; Krok, F. *Solid State Ionics* **1989**, 171.

7. Scrosati, B. *Br. Polym. J.* **1988**, *20*, 219.

8. Thomas, D. M.; McCarron, E. M.; *Mat. Res. Bull.* **1986**, *21*, 945.

9. Lemmon, J. P., Ph.D. Thesis, Oregon State University, 1994.

10. Peled, E. *Proc. Electrochem. Soc.* **1994**, *94-28*, 1.

Polyethylene Imine-Titanoniobate, and Titanate Nanocomposites

Chapter 7

7.0 **Abstract.**

A reaction of aqueous polyethylene imine (PEI) and $HTiNbO_5$ results in a nanocomposite with an interlayer separation of up to 35Å. The products have distinct layer expansions of 4, 14, and 28 Å with increasing polymer content in the reaction ratio of PEI:$TiNbO_5$, some products appear to form single phases. These nanocomposites form only under basic (pH > 8) conditions. Thermogravimetric analysis (TGA) of the pure host, as well as the nanocomposite demonstrates decomposition at about 300° C. The layered lepidocrocite structure, $H_xTi_{2-x/4}\square_{x/4}O_4 \cdot H_2O$, also expands by 27 Å after reaction with a PEI solution.

7.1 **Introduction to Polymer Intercalation of Layered Materials.**

Intercalation of polymers into layered inorganic compounds may produce composite assemblies with dimensions on the nanometer scale, which are termed nanocomposites. These new materials may have different characteristics than each pure, starting component. For example, nanocomposite battery electrode materials may possess different (and improved) electrochemical characteristics than the original host material, as seen in Chapter 6. The wide variety of uses for the individual polymers and hosts bring a large number, and variety, of potential applications to their nanocomposites; possibilities

include metal-ion removal from waste water [1, 2], optical devices [3, 4], or other materials with new electrical, or mechanical properties compared to their separate components [5-7]. Nanocomposites from the layered titanates, titanoniobates, and niobates may be of interest because of the photocatalytic activity displayed by their host materials [8-13].

There are at least four methods to produce polymer-layered-metal-oxide nanocomposites: (i) the *in-situ polymerization* method, (ii) the *exfoliation-adsorption* method, (iii) *latex-colloid* interaction, and (iv) *topotactic intercalation.* The *in-situ polymerization* process involves intercalation of small molecules into the host layers followed by *in situ* polymerization [14]. The exfoliation of a host material (in method ii) occurs when solvent molecules intercalate its galleries, increasing the layer separation to such an extent that individual layers become solvated as colloidal particles in solution. When these suspended single-layer sheets are reacted with solvated polymer, adsorption and flocculation of the nanocomposite may occur [15]. Method (iii) may be employed if the polymer and host are not soluble in a common solvent, it uses a two-phase solid-solution reaction between an emulsified polymer and an exfoliated host to produce the nanocomposite [4]. Finally, topotactic intercalation of the polymer into the host galleries may occur if reaction kinetics do not limit the extent of reaction.

There are many classes of polymeric candidates for nanocomposite synthesis including conjugated, aliphatic, and ionomeric macromolecules. Also, there are numerous host solids, in which each class may bring its own specialized method of polymer intercalation. For example, nanocomposites based on MPS_3 may form in a wholly

different way than any outlined above, where the polymer serves as a template during host-layer formation [4]. On the other hand, layered solids with high surface-area-to-charge ratios (~ 30 $Å^2$(negative charge)$^{-1}$) can exfoliate in water. Table 7.1 lists the charge density of some layered solids, and Table 7.2 shows the calculation of charge densities for the layered titanates. A comparison of the layered silicates, mica and montmorillonite, demonstrates the effect of high charge density upon (aqueous) exfoliation. Subsitution of Mg^{2+} for Al^{3+} in the aluminosilicate layers decreases the charge density of montmorillonite vs. mica, and contributes to ease of layer separation and exfoliation. The titanic acids, and and $HTiMO_5$ (M= M^{5+}), with charge densities of ~ 25 $Å^2(-)^{-1}$, are observed to form finite layer expansion hydrates, but are not observed to exfoliate in water. Up until now, these solids have not been reported to incorporate polymers.

7.2 **Intercalation of Titanates, and Titanoniobates.**

The host compound, $HTiNbO_5$, consists of corrugated sheets with composition $TiNbO_5^-$, where Ti^{4+}, and Nb^{5+} ions are randomly distributed in octahedral sites inside the double layers, and the galleries are occupied by hydronium ions (Figure 7.1). Half of the octahedra have a unique oxygen, which occupies corner positions inside the gallery, producing the step, or corrugated, appearance when viewed along the b axis. The alkali titanoniobate crystallizes in an orthorhombic unit cell, with space group *Pnma*, and cell dimensions of a= 6.459, b= 3.792, c=14.865Å for the potassium titanoniobate. [16]

The series of related sheet structures are characterized by the quantity of unique oxygens, or steps, on the sheet surfaces. The compounds can be referred to as step 2, 3,

Compound	Area (Å^2/charge)
Kaolinite	Neutral
MoS_2	Neutral
Smectites	40-120
$M_{0.25}MoO_3$	117
M_xFeOCl	100
$M_{0.3}MS_2$	60
$Li_{2x}Mn_{1-x}PS_3$ (x = 0.25)	64
Vermiculies	27-40
$Zr(HPO_4)_2 \cdot H_2O$	34
$HCa_2Nb_3O_{10}$	28
Mica	24

Table 7.1 Layered solids and their charge densities [34].

♪	a	b	c	α	β	γ	Area Å^2/(-)
$TiNbO_5^-$	6.447	3.797	18.43*	90	90	90	ab/1 = 24.49
$Ti_2O_5^{2-}$	11.35	3.80	6.63*	90	100.1	90	ab/2 = 21.6
$Ti_3O_7^{2-}$	8.571*	3.804	9.135	90	101.57	90	bc(sin 180-β)/2 = 17.02
$Ti_4O_9^{2-}$	22.4*	3.79	12.04	90	104	90	" = 22.1
$Ti_5O_{11}^{2-}$	19.7*	3.81	15.02	90	106.9	90	" = 27.4
$Ti_{(2-x/4)}\square_{x/4}O_4^{x-}$	3.837	17.198*	2.960	90	90	90	ac/x = 16.2

* Stacking direction

♪ Each unit cell contains two formula units, and two layers, therefore, there is one formula unit per layer within the cell, with the noted charge.

Table 7.2. Area-per-charge for the titanates as calculated from their lattice parameters. The leprodocite-like structured titanate has $x \approx 0.70$, which was used to calculate the charge density value.

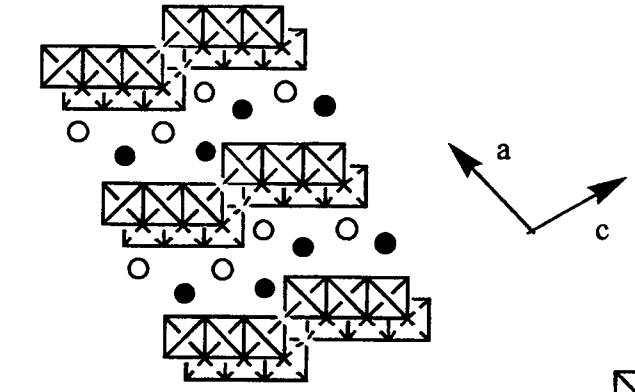

(a) a = 8.571, b = 3.804
c = 9.135, B = 101.57

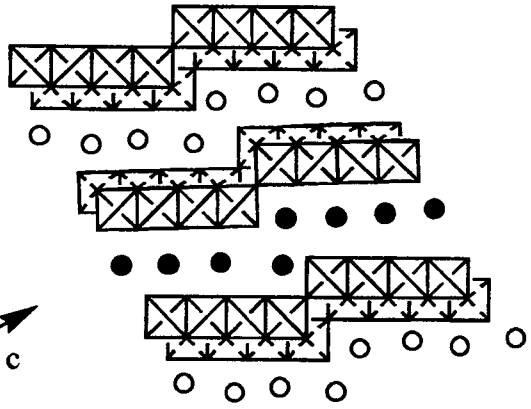

(b) a = 22.4, b = 3.79,
c = 12.04, B = 103.7

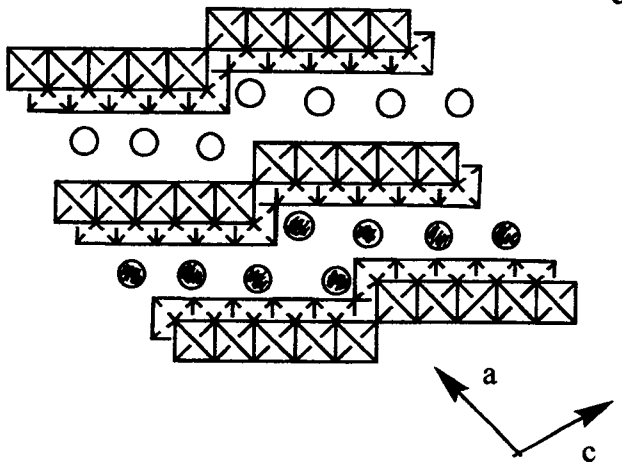

(c) a = 19.7, b = 3.81
c = 15.02 B = 106.9

Figure 7.1. The structure of some idealized layered titanates: (a) $Na_2Ti_3O_7$ [32] (b) $K_2Ti_4O_9$ [30] (c) $Cs_2Ti_5O_{11}$ [31] (d) $Cs_xTi_{2-x/4}\square_{x/4}O_4$ [17], and (e) $KTiNbO_5$ [10, 16]. The stacking direction is indicated for each structure.

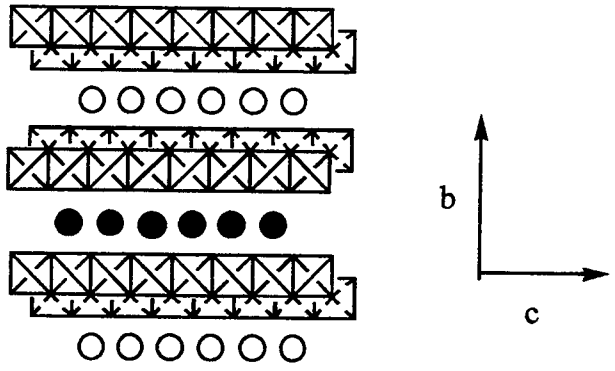

(d) a = 3.84, b = 17.20, c = 2.96

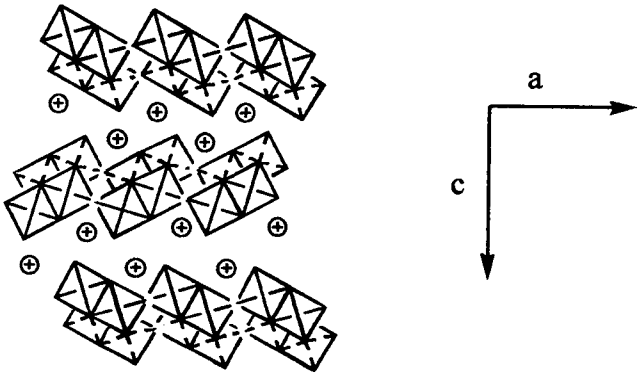

(e) a = 6.459, b = 3.792, c = 18.472

Figure 7.1 continued.

4, and 5 structures (Figure 7.1), where each step size increase has a successively lower layer charge density. A planar sheet, in this series, would be charge neutral; however, vacancies inside the octahedral layers can provide a net charge. The compound $Cs_xTi_{2-x/4}\square_{x/4}O_4 \cdot H_2O$ has planar sheets, and is described by the lepidocrocite structure, where octahedral vacancies in the Ti^{4+} layers are stabilized by exchangeable Cs^+ ions (the box represents a vacancy). This compound crystallizes in an I-centered, orthorhombic cell with dimensions a=3.837, b= 17.198, c=2.960 Å [17]. This is the highest charge density titanate, as seen in the comparison made in Table 7.2.

Figure 7.1 shows the structure of $KTiNbO_5$, $Cs_xTi_{2-x/4}\square_{x/4}O_4 \cdot H_2O$, and other layered titanates. These solids are Brønsted-Lowry bases due to prodonation of the unique oxygens, or, in the case of lepidocrocite, due to incorporation of H_3O^+ between the layers. Upon reaction with acid, the alkali metal ions exchange with protons, producing the acidic solid [18, 19]. The X-ray diffraction (XRD) patterns of $KTiNbO_5$, and $Cs_xTi_{2-x/4}\square_{x/4}O_4 \cdot H_2O$, as well as their acid exchanged forms are shown in Figure 7.2-7.3.

The protonated form of these solids can intercalate of organic bases, such as primary, secondary, and tertiary amines [20]. The structure of these compounds (Figure 7.4) is deduced from analysis of the increase in basal spacing with the chain length of the alkyl ammine intercalate, and consists of double layers of alkylammonium ions reclining at an angle within the titanate galleries. The rate of intercalation follows the order of $1° > 2° > 3°$, and no reaction occurs if the solid is basic (ie. contains an alkali metal charge balancing ion) [20-22].

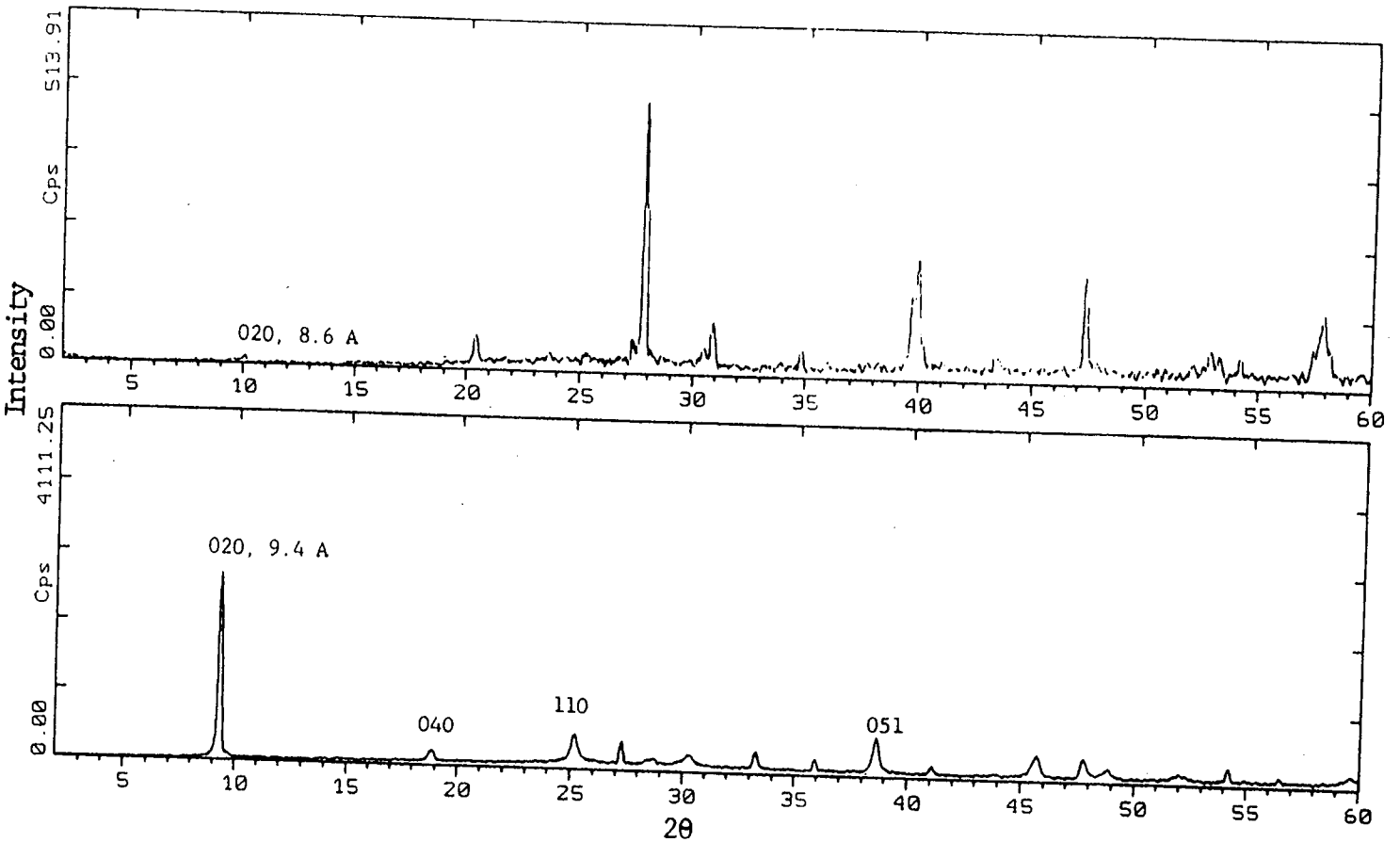

Figure 7.2. XRD of $Cs_xTi_{2-x/4}\square_{x/4}O_4$ (upper window) and $H_xTi_{2-x/4}\square_{x/4}O_4 \bullet H_2O$.

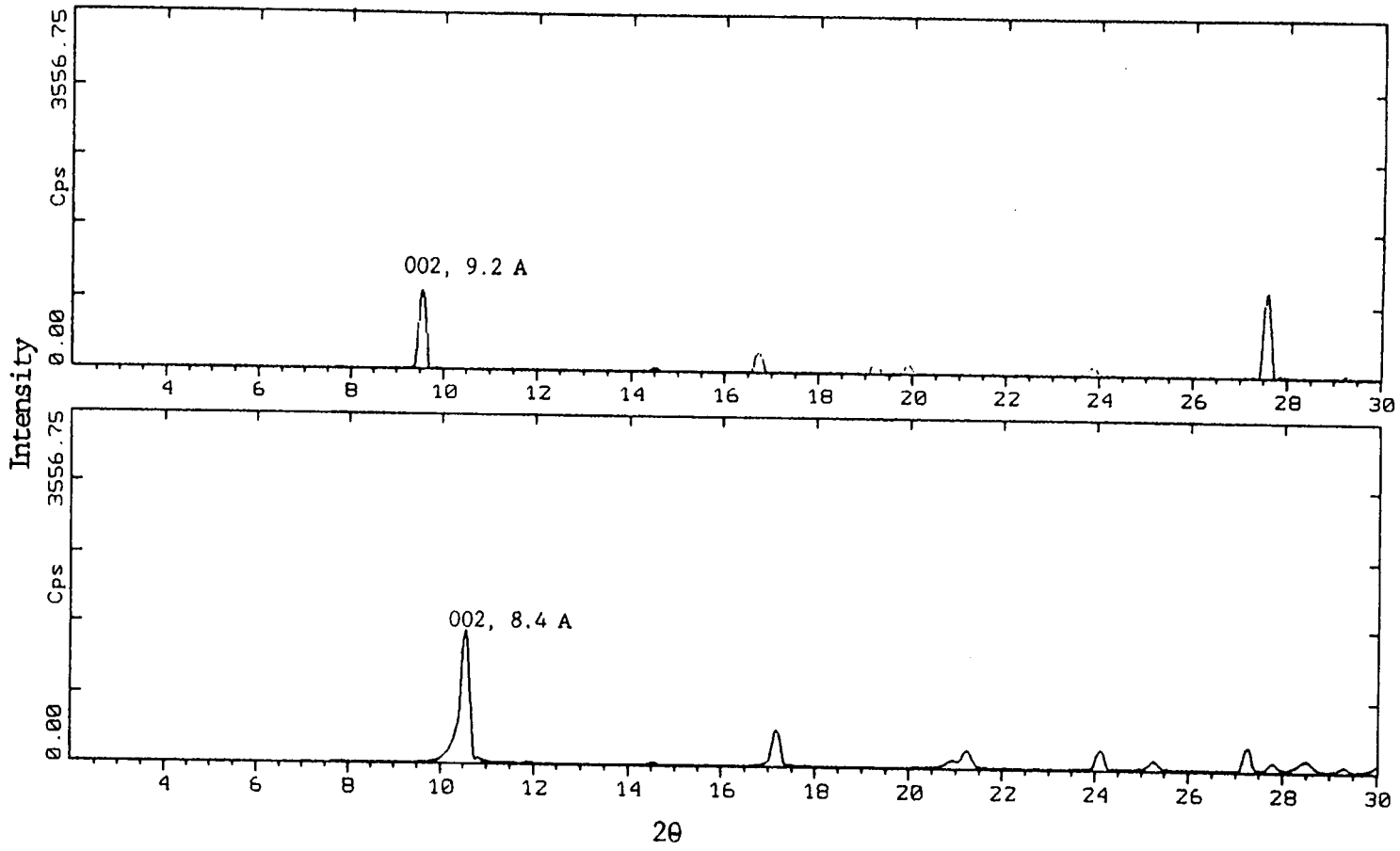

Figure 7.3. XRD of $KTiNbO_5$ (upper window), and $HTiNbO_5$.

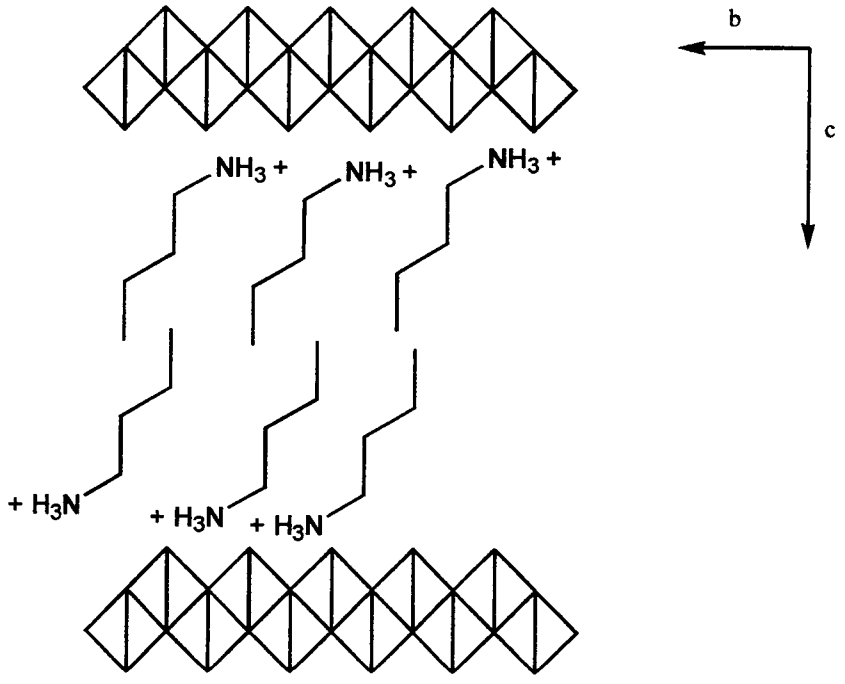

Figure 7.4. The orientation of an n-alkylammonium intercalate in a high charge density solid host such as $HTiNbO_5$.

Neither the alkali metal titanates, titanoniobates nor the titanic, and titanoniobic acids exfoliate in water. Apparently, the solvent-ion hydration energy does not overcome the electrostatic attraction between the negatively-charged oxide layers and the intercalated cations. Lithium titanates / titanoniobate may form milky suspensions, which are likely suspended microparticles of the oxide, rather than solvated, individual sheets. Titanates, therefore, are not observed to form nanocomposites via the exfoliation-adsorption route when mixed with an aqueous polymer as do smectite clays, or other layered structures that form colloids in water. Even PEO has a dielectric constant sufficient to solvate the easily expandable smectite clays, and the molten polymer is observed to intercalate them. However, the titanate solids do not react with neat, molten PEO.

Recently, an effort to obtain suspended layers of a titanate was reported by Sasaki *et al.* The reaction of $H_xTi_{2-x/4}\square_{x/4}O_4 \cdot H_2O$ + $[N(C_4H_9)_4]OH$ (tetrabutylammonium hydroxide, TBAOH) resulted in a wet product with layers expanded > 100Å [23], and the aqueous system was claimed to have exfoliated. Curiously, we observe that aqueous PEO added to this reaction mixture does not result in the formation of a nanocomposite. These sheets may not expand enough to resemble suspended, colloidal sheets, that are likely to form nanocomposites via adsorption, as with exfoliated smectite clays. Further investigation into the reactivity of an aqueous polymer and titanates intercalated with a series of tetra-alkylammonium hydroxides has not been accomplished, and may lead to an exfoliation.

Other laboratories have proposed exfoliation followed by restacking as the process that occurs in the multi step intercalation of subsequently weaker bases into $HTiNbO_5$, in which alkylamine is replaced by a weak base, such as spiropyran, or azodianiline, using the sequence of reactions described below [20].

$$KTiNbO_5 \xrightarrow[HCl]{} HTiNbO_5$$

$$HTiNbO_5 \xrightarrow[C_nH_{(2n+1)}NH_2]{} [C_nH_{(2n+1)}NH_3]_xH_{(1-x)}TiNbO_5 \qquad (7.1)$$

$$C_nH_{(2n+1)}NH_3]_xH_{(1-x)}TiNbO_5 \xrightarrow[azodianiline]{} [N_2(C_6H_5NH_2)_2H_y]_xH_{(1-xy)}TiNbO$$

In our laboratory, neither PEI, nor PEO was not observed to intercalate the titanoniobate in this manner (substitute azodianiline with a polymer in the final reaction above). The term, exfoliation may be descriptive in the context of the work of Sasaki, and Tagaya, however, as explained above, there are differences in the behavior of exfoliated smectite clay, and the TBAOH - titanate system with respect to their interaction with aqeous PEO.

This chapter demonstrates the ability of PEI to intercalate into $HTiNbO_5$ and $H_xTi_{2-x/4}\square_{x/4}O_4 \bullet H_2O$.

7.3 **Experimental.**

7.3.1 **Preparation of $KTiNbO_5$, and $Cs_xTi_{2-x/4}\square_{x/4}O_4 \cdot H_2O$.**

An intimate mixture of potassium carbonate (Mallinkrodt, reagent), anatase (Spectrum, reagent) TiO_2, and Nb_2O_5 (Aldrich, reagent) was achieved by grinding an acetone slurry with a mortar and pestle. This mixture was pelletized, and heated in air overnight at 800°C in an alumina crucible to produce pure $KTiNbO_5$. The reaction is shown below:

$$K_2CO_3 \quad 2TiO_2 \quad Nb_2O_5 \rightarrow 2KTiNbO_5 \quad CO_2 \qquad (7.2)$$

The solid was identified, and its purity was determined by X-ray powder diffraction (Figure 7.2), the patterns matched those reported by Wadsley [24]. $Cs_xTi_{2-x/4}\square_{x/4}O_4$ was synthesized using anatase and $CsNO_3$ (Aldrich, reagent) treated as described above, its XRD pattern (Figure 7.3) matched those reported by Grey *et al.* [17].

Titanic, and titanoniobic acids were obtained by hydronium-ion exchange with the cesium titanate and the potassium titanoniobate in an excess of 2 M HCl, the reaction solution was decanted and replaced three times. These solid acid products display single phases corresponding to hydronium ions present within their galleries. As shown in Figure 7.2 and 7.3, the titanoniobic acid interlayer spacing is 8.4 Å (a decrease from 9.2 Å), and the titanic acid is 9.5 Å (an increase from 8.6 Å). The titanoniobate interlayer spacing decreases upon protonation of the unique, basic oxygens on the layer surfaces; the lepidocrocite structure does not have the basic, edge oxygens, therefore, hydronium ions

are not as closely associated with its sheets, and the structure expands from the presence of two layers of water [18].

7.3.2 Nanocomposite Preparation.

Polymer-titanoniobate nanocomposites were prepared from a mixture of $HTiNbO_5$ and a 7 % (by weight) solution of PEI (Pfaltz & Balmer, linear, M_w= 60,000 D, pH 10). Aqueous PEI reacts with acid as noted below.

$$(CH_2CH_2NH)_n \quad H_3O^+ \rightleftharpoons \quad (CH_2CH_2NH)_n^+ \quad H_2O \tag{7.3}$$

The PEI solution as received is ~ 20 % protonated, where n≈5 [2]. Various pH conditions were investigated by adding 1M HCl to the polymer solutions before reaction with the host solid. Stoichiometric mixtures were measured as monomer units of PEI (CH_2CH_2NH) per formula unit of the anion $TiNbO_5^-$. The reactions were completed after one day of gentle heating at 80°C, or 14 days of stirring at 40° C, and were not affected by exposure to air and light. The products were isolated by centrifugation, and washed three times with dionized water, then heated *in vacuo* at 80-120°C, or air dried.

Thermogravimetric analyses of the titanoniobate samples were accomplished using a Shimadzu TGA 50 with the heating rate set to 10° C min^{-1} and a 40 mL min^{-1} flow of air over a platinum pan.

7.4 Results and Discussion.

Figure 7.5 shows XRD patterns of nanocomposites prepared with increasing PEI:$TiNbO_5^-$ composition. The host material gradually disappears from the products with

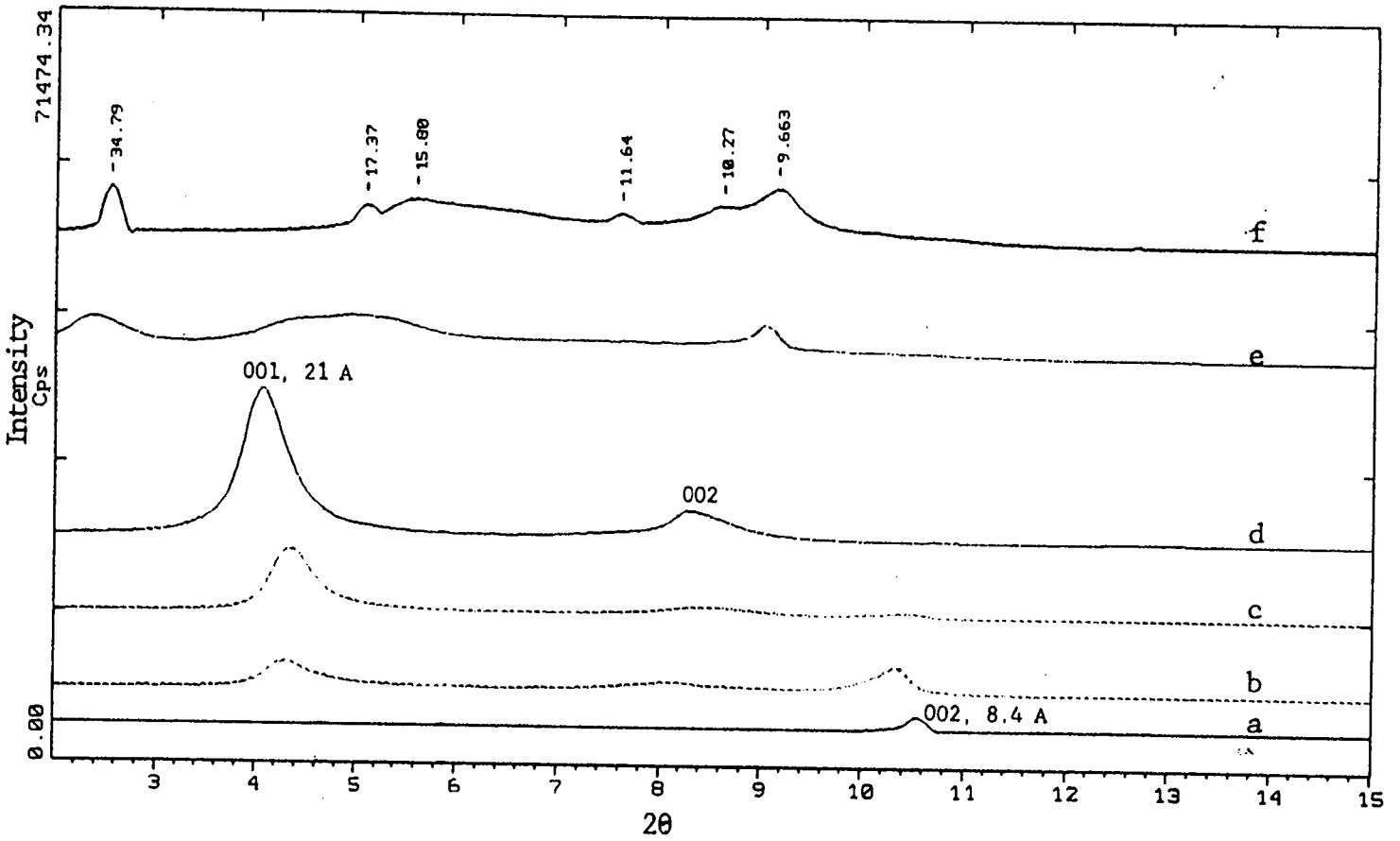

Figure 7.5. XRD of $PEI_xH_yTiNbO_5$ as a function of increased intital $PEI:TiNbO_5$ ratio (mol/mol). (a) $HTiNbO_5$ (b) 1:1 (c) 2:1 (d) 3:1 (e) >7:1 (f) > 12:1, reacted at room temperature.

greater PEI content, also the intensity increases for a phase with a basal separation of 20-21 Å. The 3:1 mixture appears to form a single ordered phase with a 20.2 Å basal spacing. When excess PEI reacts with the host, a highly crystalline phase is evident with the basal repeat distance of 33 Å, exhibiting multiple 00ℓ reflections, as well as evidence of other phases.

Table 7.3 summarizes the changes in the separation of the basal planes within these products. The layer expansion does not gradually increase during reaction progress, instead a series of discrete expanded phases are observed. The initially layer expansions of 3.7 Å and 14 Å are subsquently replaced with a layer expansion of 28 Å. Moderate heating (80° C) of a >12:1 reaction ratio of PEI produces a single phase product with an interlayer spacing of 37Å.

Figure 7.6 shows the reaction progress of the lepidocrocite structure with excess PEI. The nanocomposite formed progresses through very similar phases to the PEI-titanoniobate. The final product contains a large polymer layer of 27 Å, with a basal repeat of 35 Å. The layer expansion for this structure is found from α - 8.2 Å, where α is the observed basal repeat distance.

Heating the products *in vacuo* at 100° C results in visible water condensation in the container above the samples. XRD of these dry products show conservation of the large basal repeat distance, and indicate that these layer expansions do not derive from water uptake. Upon drying, however, products show a 2 Å decrease in the broad diffraction peaks, such as the ones at 15.8 and 10.3 Å in Figure 7.5.

Pattern location	*00l* reflections present	α (Å)	α-7.2 *	PEI:$TiNbO_5^-$	wt % PEI ♭
7.3	001 ($HTiNbO_5$)	8.41	---	0	2% ♯
7.5(b)	001	21, 8.4	13.8	< 1:1	----
7.5(d)	001, 002	21.0	13.8	≈3:1	12%
7.5(e)	001, 002, 003	33.0, 19.2	25.8	≈7:1	34%
7.5(f)	001, 002, 003, 004, 005	34.7, 15, 10	27.5	>>7:1	35%
7.7(e)	001, 002	21, (10.9)	(3.7)	≈3:1	34%

α = basal plane repeat distance.
* α - 7.2 Å represents the expansion due to polymer uptake in $TiNbO_5$
♯ This represents dehydration at 300° C.
♭ Dehydration below 150° C is not included in the values.

Table 7.3. Summary of PEI-$TiNbO_5$ diffraction and TGA.

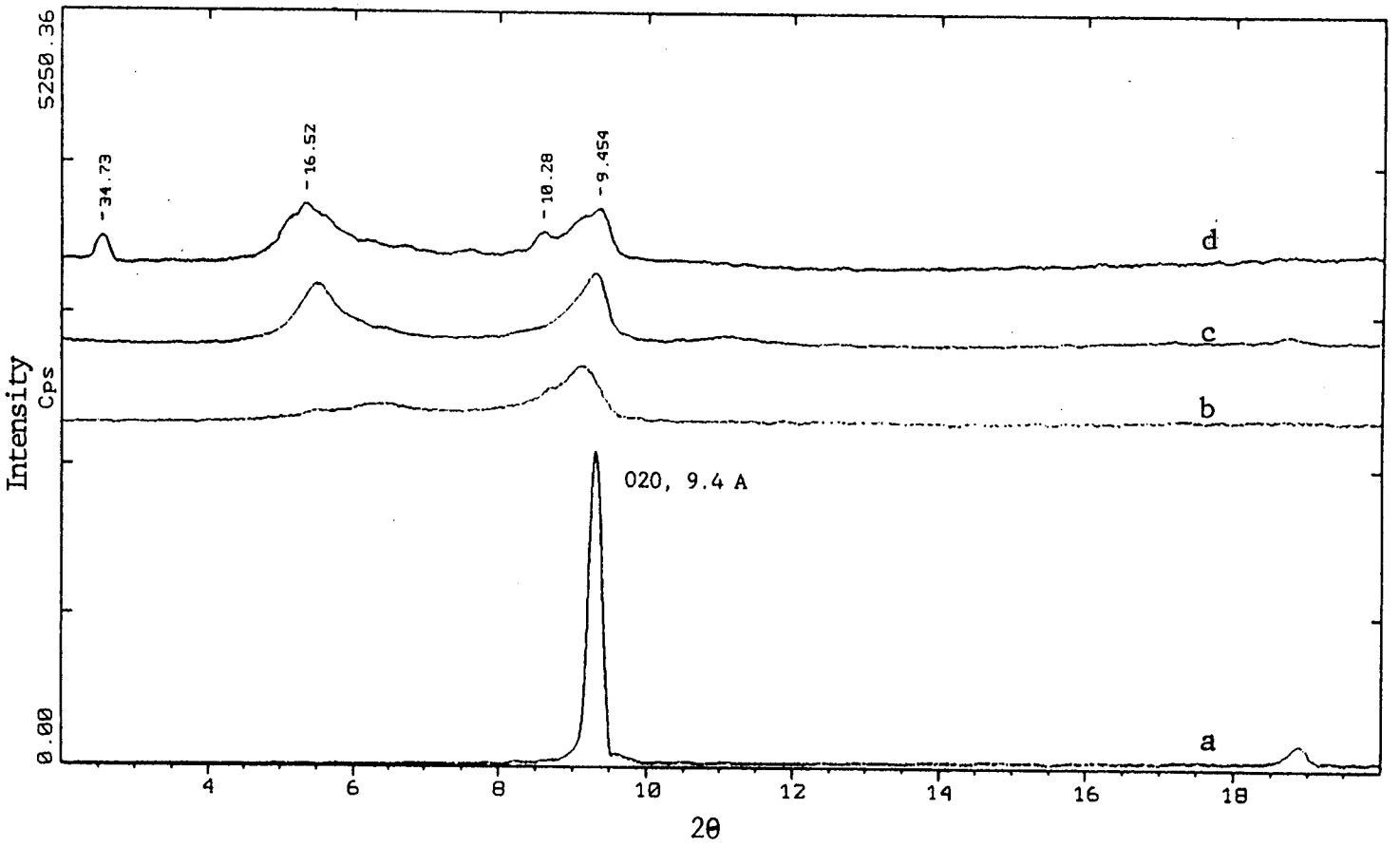

Figure 7.6. XRD of $PEI_xH_yTi_{2-x/4}\square_{x/4}O_4$ as a function of time from a room temperature reaction of excess PEI in $H_xTi_{2-x/4}\square_{x/4}O_4 \cdot H_2O$. (a) $H_xTi_{2-x/4}\square_{x/4}O_4 \cdot H_2O$ (b) 2 days (c) 8 days (d) 9 days.

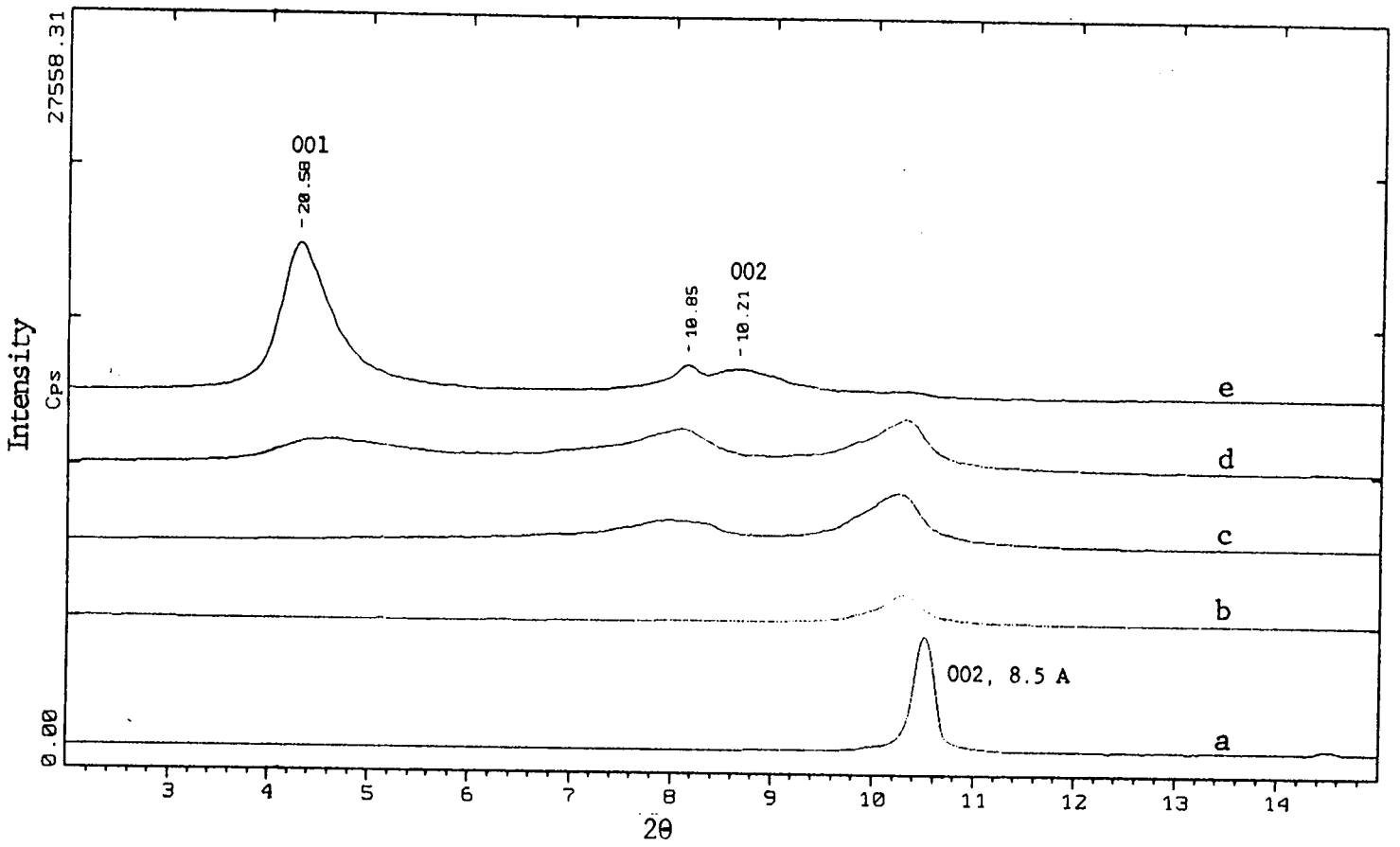

Figure 7.7. XRD of $PEI_xH_yTiNbO_5$ as a function of pH of a 3:1 reaction mixture. The pH was adjusted with HCl before the addition of the solid to the reaction vessel. (a) $HTiNbO_5$, (b) pH 4, (c) pH 6, (d) pH 8, (e) pH 10. The polymer solution is originally at pH 10.

The diffraction patterns in Figure 7.7 demonstrate the reaction progress as a function of pH, and show that intercalation increases with the basicity of the PEI solution. When PEI is protonated above 30% (below pH 10), the polymer does not enter the galleries to a great extent, and at pH 4 there is no evidence of any layer expansion. These data suggest that an acid-base reaction is involved in the progress of intercalation. Under the more basic conditions, the polymer is less ionized, but may still coordinate alkali ions in solution; however, the acidity within the host layers may drive the intercalation.

Figure 7.8 shows scanning electron micrographs (SEM) from products of 3:1 and 7:1 reaction ratios, as well as the host material. The particle size decreases with increasing PEI content. The 3:1 solid appears homogeneous with dimensions of $10 \times 10 \times 2\mu$m, while particles from the 7:1 solid are $5 \times 5 \times 2\mu$m. All products show are square (or rectangular), and flat, with a decreased thickness compared to the host material.

The TGA of the host material, PEI or alkyl amine titanoniobate nanocomposites are shown in Figure 7.9, and the weight percentage lost from the nanocomposites are summarized in Table 7.3. The host experiences dehydration at about 300° C, which coincides with the nanocomposite decomposition. All of the nanocomposites that were dried in air appear to lose water from 50 - 150° C. This feature disappears for the vacuum dried samples. Weight loss above 150° C is assumed to derive from polymer degradation only. These data indicate that the weight of PEI in the galleries of the product in Figure 7.5 (c) is about one-third that of the product shown in 7.5 (e), which is consistent with the large expansion noted in XRD data.

The polymer orientation within any host may not be easily determined, especially because spectroscopic, and thermal data from a polymer within galleries may not be differentiated from a polymer outside of the galleries. Some spectroscopic data of PEO montmorillionite nanocomposites indicate that helical PEO exists within the galleries; however, this is probably misleading as an excess of polymer is used in the nanocomposite synthesis [26]. However, recent XRD patterns from $Li_x(PEO)_yV_2O_5$ were used to produce 1D electron density maps that may suggest extended (zigzag) chains of PEO intercalated as a monolayer, or bilayer within the host [27].

The progression of layer expansions observed in this report departs from previous work. PEO nanocomposites with 4 or 8 Å expansions have been observed previously at low and high polymer loading respectively, these expansions correspond with a polymer monolayer, or bilayer [14, 15]. In the titanate-PEI chemistry, an initial expansion of 3.7 Å may be explained by a monolayer of PEI, however, the larger expansions evident may not be easily explained with known conformations of PEI. The crystal structure data of protonated PEI indicate the presence of planes (about 4 Å thick) with hydrogen bound water molecules in between layers of the polymer [28]. An initial layer expansion of about 4 Å, therefore, matches well with a monolayer of polymer oriented in similar planes parallel to the sheets.

The large expansions of 14, and 28 Å may result from an interplay of lattice and solvation enthalpies, rather than from steric factors of polymer conformation. This sort of behavior is observed with smectite clays. For example, montmorillionite may swell in water to some stable states with basal spacings of 9.7, 12.0, 15.5, and 18.3 Å (20.7 and

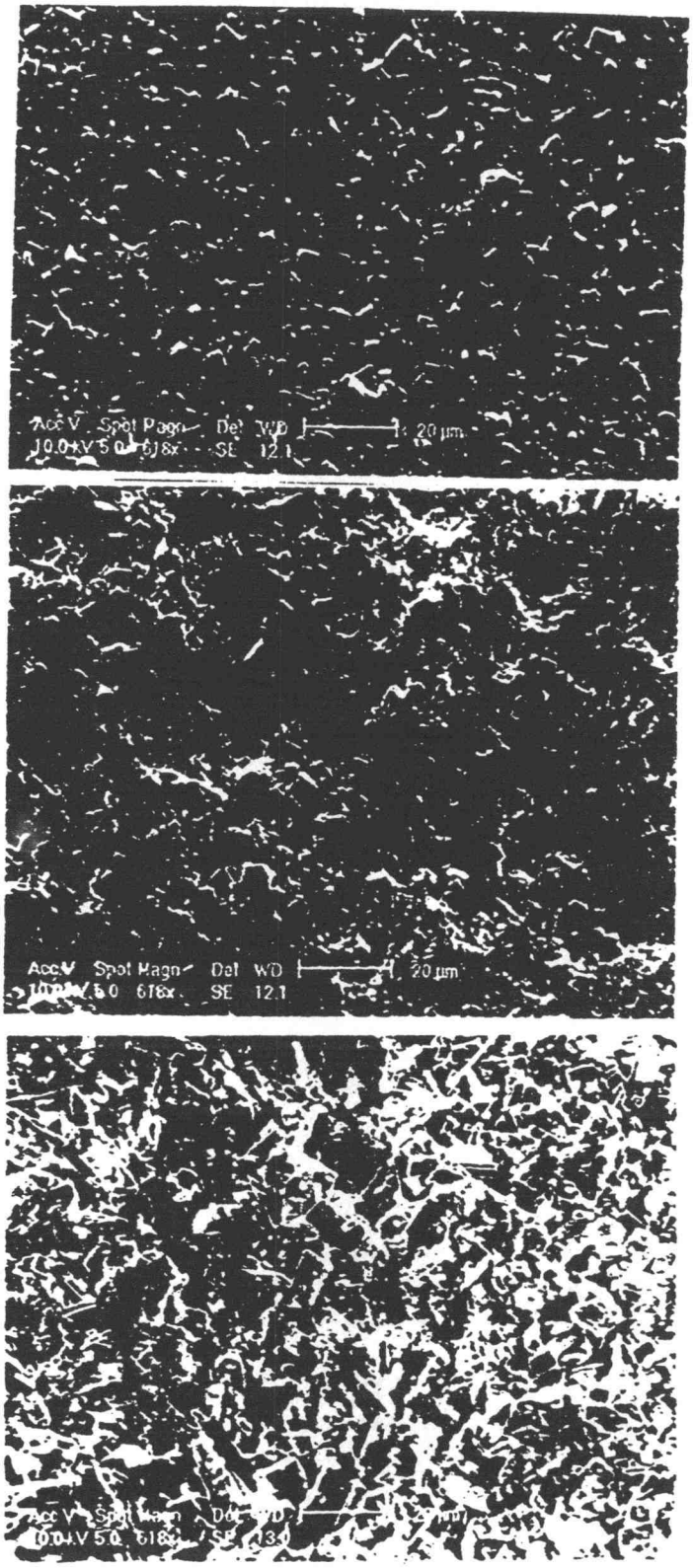

Figure 7.8. SEM of (a) $HTiNbO_5$ and the PEI intercalated products from (b) the 3:1 and (c) the 7:1 mixture. Each image was obtained using the same scale.

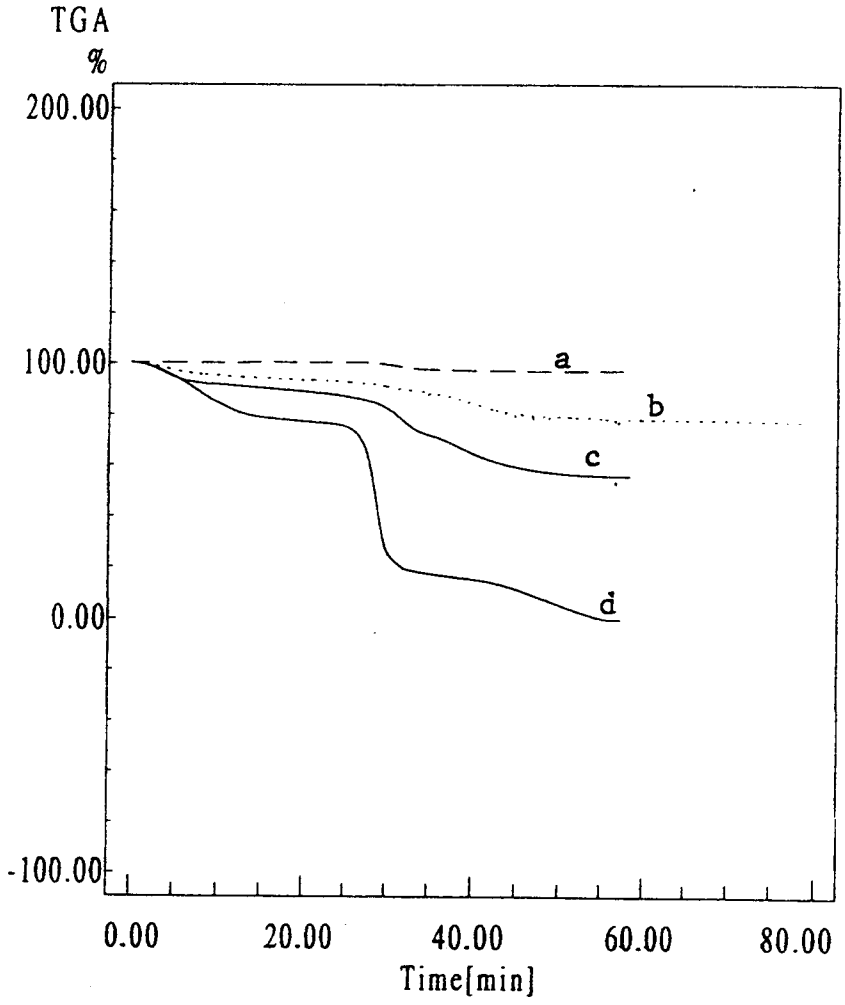

Figure 7.9. TGA of (a) $HTiNbO_5$ and products obtained from (b) the 3:1 (c) 7:1 mixtures, the TGA of >12:1 product is similar to (c), (d) pure PEI. The initial weight loss is likely surface adsorbed water.

23.5 Å interlayer spacings are also observed). The basal spacing increases stepwise, and the process is thought to occur with additions of one, three, and five water layers along with adsorption and desorption of water from the clay surfaces, rather than incremental additions of one water layer after another [29]. The similar layer expansions of about 28 Å observed in PEI:$TiNbO_5$ and PEI:$H_xTi_{2-x/4}\square_{x/4}O_4$ (see Figure 7.10) in this investigation, as well with PEI_x $Zr(HPO_4)$ in the work of Costantino and Marmottini [34], may indicate that these expansions are driven by polymer conformation within the galleries.

7.5 **Conclusion.**

When solvated PEI is added to solid titanic, or titanoniobic acid, the polymer intercalates into the solid. There are several phases of nanocomposite which correspond to increasing concentrations of PEI, allowing for control in the size of the nanocomposite gallery, the interlayer expansions occur with values 4, 14, and 28 Å for the titanoniobate, and the lepidocrocite structure is observed to have similar behavior. The intercalation may be driven by Brønsted-Lowry acid - base interactions, as well as electrostatic interactions between charged layers and intercalated molecules.

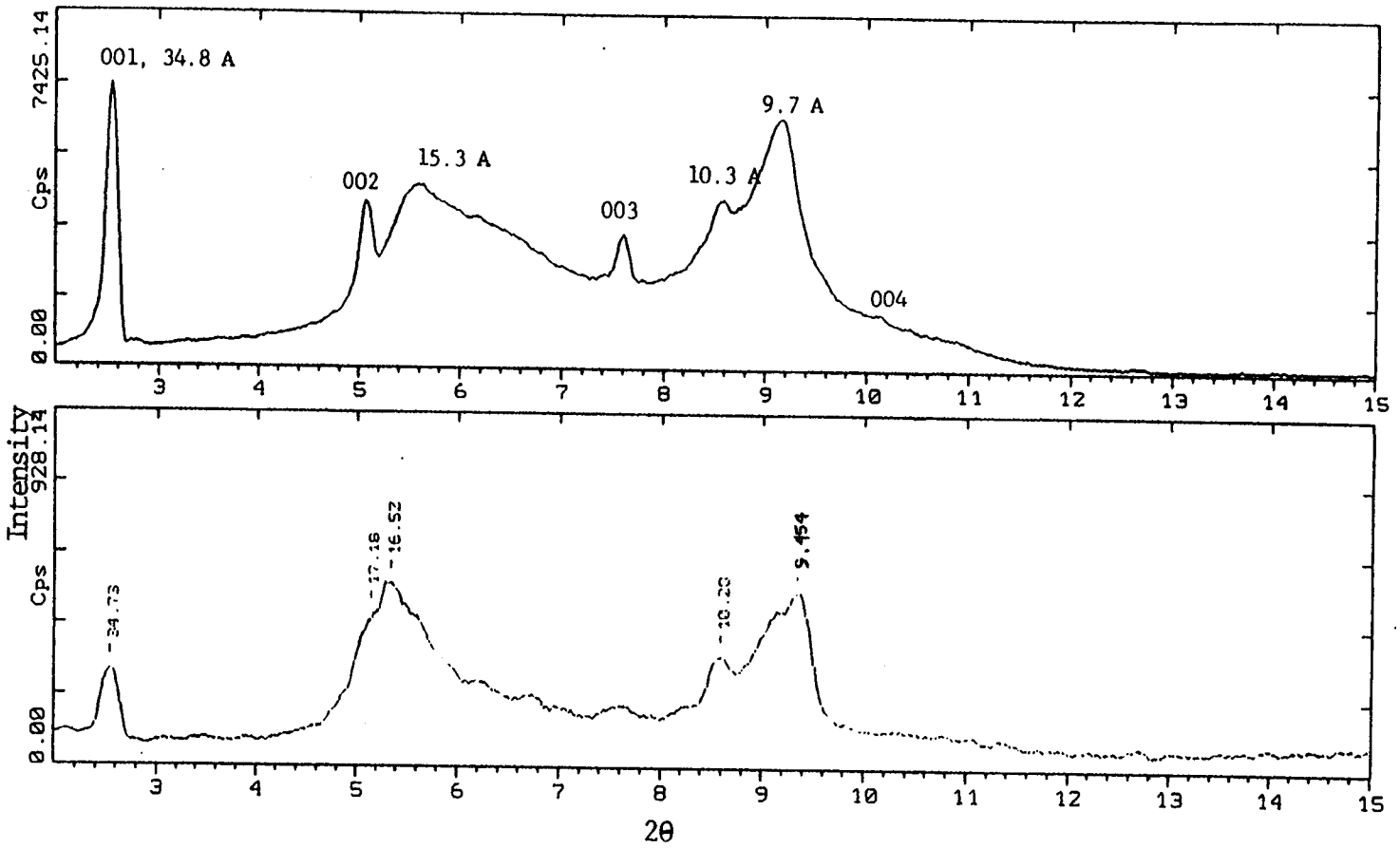

igure 7.10. XRD comparison of $PEI_y\ H_xTi_{2-x/4}\square_{x/4}O_4 \cdot H_2O$ (lower window) and $PEI_xH_yTiNbO_5$ (upper window) nanocomposites. oth products are from a reaction of the solid in excess PEI.

7.6 **References.**

1. Ogawa, M.; Kuroda, K. *Chem. Rev.* **1995**, *95*, 399.

2. Zelewsky, A. von; Barbosa, L.; Schlapfer, C. W. *Coord. Chem. Rev.* **1993**, *123*, 229.

3. Willner, I.; Eichen, Y.; Frank, A. J.; Fox, M. A. *J. Phys. Chem.* **1993**, *97*, 7264.

4. Oriakhi, C., Ph.D. Thesis, Oregon State University, 1996.

5. Yano, K.; Usuki, A.; Okada, A.; Kurauchi, T.; Kamigaito, O. *Polym. Prepr.* **1991**, *32*, 65.

6. Okada, A.; Fukumori, K.; Usuki, A.; Kojima, Y.; Kurauchi, T.; Kamigaito, O. *Polym. Prepr.* **1991**, *32*, 540.

7. Okada, A; Kawasumi, M.; Usuki, A.; Kojima, Y.; Kurauchi, T.; Kamigaito, O. *Mater. Res. Soc. Symp. Proc.* **1990**, *171*, 45.

8. Domen, K.; Kudo, A; Shibata, M.; Tanaka, A.; Maruya, K.; Onishi, T. *J. Chem. Soc., chem. Commum.* **1986**, 1706.

9. Kudo, A.; sayama, K.; Tanaka, A.; Asakura, K; Domen, K.; Maruya, K; Onishi, T. *J. Catal.* **1989**, *120*, 337.

10. Kudo, A.; Tanaka, A.; Domen, K.; Maruya, K; Aika, K.; Onishi, T. *J. Catal.* **1989**, *111*, 67.

11. Sayama, K; Tanaka, A.; Domen, K.; Maruya, K.; Onishi, T. *J. Phys. Chem.* **1991**, *95*, 1345.

12. Kim, Y. I.; Salim, S.; Huq, M. J.; Mallouk, T. E. *J. Am. Chem. Soc.* **1991**, *95*, 1345.

13. Kim, Y. I.; Atherton, S. J.; Brigham, E. S.; Mallouk, T. E. *J. Phys. Chem.* **1993**, *97*, 11802.

14. Lan, T.; Kaviratna, P. D.; Pinnavera, T. J. *Chem. Mater.* **1995**, *7*, 2144.

15. Lemmon, J. P.; Wu, J.; Oriakhi, C.; Lerner, M. M. *Electrochim. Acta* **1995**, *40*, 2245.

16. Wadsley, A. D. *Acta Cryst.* **1964**, *17*, 623.

17. Grey, I. E.; Li, C.; Madsen, I. C.; Watts, J. A. *J. Solid St. Chem.* **1987**, *66*, 7. (f)

18. Sasaki, T.; Watanabe, M.; Michiue, Y.; Komatsu, Y.; Izumi, F.; Takenouchi, S. *Chem. Mater.* **1995**, *7*, 1001.

19. Sasaki, T.; Watanabe, M.; Komatsu, Y.; Fujiki, Y. *Inorg. Chem.* **1985**, *24*, 2265.

20. Tagaya, H.; Saito, K.; Kusahara, T.; Kadokawa, J.; Chiba, K. *Catal. Today* **1993**, *16*, 463.

21. Izawa, H.; Kikkawa, S.; Koizumi, M. *Polyhedron* **1983**, *2*, 741.

22. Weiss, A.; Weiss, A. *Angew. Chem.* **1960**, *72*, 413.

23. Sasaki, T.; Watanabe, M.; Hashizume, H.; Yamada, H.; Nakazawa, H. *Chem. Commum.* **1996**, 229.

24. Wadsley, A. D. *Acta Cryst.* **1964**, *17*, 623.

25. Daniel, M. F.; Desbat, B.; Sassegues, J. C. *Solid State Ionics* **1988**, *28-30*, 632.

26. Ruiz-Hitzky, E.; Casal, Blanca *J. Chem. Soc., Faraday Trans. 1* **1986**, *86*, 1597.

27. Liw, Y.-J; Schindler, J. L.; DeGroot, D. C.; Kannewurf, C. R.; Hirpo, W.; Kanatzidis, M. G. *Chem. Mater.* **1996**, *8*, 525.

28. Chatani, Y.; Tadokoro, H.; Saegusa, T.; Ikeda, H. *Macromolecules*, **1981**, *14*, 315.

29. Karaborni, S.;Smit, B.; Heidug, W.; Urai, J.; van Oort, E. *Science* **1996**, *271*, 1102.

30. Dion, M.; Piffard, Y.; Tournoux, M. *J. Inorg. Nucl.Chem.* **1978**, *40*, 917.(c)

31. Grey, I. E.; Madsen, I. C.; Watts, J. A.; Bursill, L. A.; Kwiatkowska, J. *J. Solid St. Chem.* **1985**, *58*, 350.

32. Anderson, S.; Wadsley, A. D. *Acta Crystallogr.* **1961**, *14*, 1245.

33. Costantino, U.; Marmottini, F. *Mater. Chem. and Phys.* **1993**, *35*, 193.

34. Jacobson, A. J. *Mat. Sci. For.* **1994**, *152*, 1.

Conclusion

Chapter 8

Many new materials exist that may be useful as battery electrodes, and electrolyte salts. Small, thin batteries and the materials composing the electrode pose unique requirements for the electrolyte. Polyethers are some possible electrolyte candidates for use in these batteries because of their processability, electrochemical stability, and abiltiy to conduct ions. The development of solid polymeric electrolytes (SPEs) for battery separator devices has been limited by relatively low conductivity that exists below the melting point of the polymer. Also, amorphous SPE have mechanical limitations, and form a resistive layer upon contact with the electrodes. This research effort produced mechanically stable UV crosslinked polyethers for SPEs, as shown in Chapter 4. Crosslinking polyethers with UV radiation produces alcohol as a reaction by-product, which decreases the stability of the resulting PE against lithium elecectrodes. Chapter 5 demonstrated that treatment of these crosslinked films with methylating, silylating agents, or plasticization can produce electrochemical, and stability against lithium metal on par with other linear polyethers.

Electrode/electroltye interactions between the cathode and SPE have not been extensively studied. Chapter 6 demonstrated that a layered nanocomposite, $Li_xPEO_yMoO_3$, forms a low impedance interface with SPEs as well as liquid electrolytes (LEs) compared with the control cell constructed from the Li_xMoO_3 host material.

This provides some evidence as to the possible utility of using nanocomposites as electrodes in battery devices.

While the titanates may not find utility in batteries, they may be useful within other electrochemical devices, and the formation of nanocomposites from these layered solids may be of interest. Chapter 7 reports upon the incorporation of polyethylene imine (PEI) into $HTiNbO_5$ and $H_xTi_{2-x/4}\square_{x/4}O_4 \bullet H_2O$. These nanocomposites form only under basic (pH > 8) conditions. Thermogravimetric analysis (TGA) of the pure host, as well as the nanocomposite demonstrates decomposition at about 300° C. These solids, as well as $Zr(HPO_4)$ are observed to undergo a 28 Å interlayer expansion upon reaction with aqueous PEI, such a large expansion provides a challenge to future workers as to the structural description of the polymer within these galleries.

BIBLIOGRAPHY

Allcock, H. R.; Nelson, C. J.; Coggio, W. D. *Proceedings of the American Chemical Society Division of Polymeric Materials: Science and Engineering* **1993**, *68*, 76.

Anderson, S.; Wadsley, A. D. *Acta Crystallogr.* **1961**, *14*, 1245.

Armand, M.; Sanchez, J. Y.; Gauthier, M.; Choquette, Y. In *Electrochemistry of Novel Materials* Lipkowski, J.; Ross, P. N. Ed.s; VCH: New York, 1994; ch. 2.

Armstrong, R. D.; Todd, M. in *Solid State Electrochemistry* Bruce, P. G. Ed.; Cambridge: New York, 1995; ch. 10.

Ballard, D. G. H.; Cheshire, P.; Mann, T. S.; Przeworski, J. E. *Macromolecules* **1990**, *23*, 1256.

Bennett, J. L.; Dembeck, A. A.; Allcock, H. R.; Heyen, B. J.; Shriver, D. F. *Chem. Mater.* **1989**, *1*, 14.

Benrabah, D.; Sanchez, J. Y.; Armand, M. *Electrochim. Acta* **1992**, *37*, 1737.

Berthier, C.; Gorecki, W.; Miner, M.; Armand, M. B.; Chabagno, J. M.; Rigaud, P. *Solid State Ionics* **1983**, *11*, 91.

Blonsky, P. M.; Shriver, D. F.; Austin, P.; Allcock, H. R. *J. Am. Chem. Soc.* **1986**, *106*, 6854.

Booth, C.; Nicholas, C. V.; Wilson, D. J. *Polymer Electrolyte Reviews-2* Maccallum, J. R. and Vincent, C. A. Eds, Elsevier Applied Science, NY, p. 241.

Boroghini, M. C.; Mastragostino, M.; Passerini, S.; Scosati, B. *J. Electrochem. Soc.* **1995**, *142*, 2118.

Bruce, P. G.; Krok, F. *Solid State Ionics* **1989**, 171.

Bruce, P. G.; Gray, F. M. in *Solid State Electrochemistry* Bruce, P. G. Ed.; Cambridge: New York, 1995; ch. 6.

Bruce, P. G. *Electrochim. Acta.* **1995**, *40*, 2077.

Bruce, P. G. in *Polymer Electrolyte Reviews-1* MacCallum, J. R.; Vincent, C. A.; Elsevier: New York, 1989; ch. 8.

Bruce, P. G.; Krok, F. *Electrochim. Acta* **1988**, *33*, 1669.

Chatani, Y.; Okamura, S. *Polymer* **1987**, *28*, 1815.

Chatani, Y.; Tadokoro, H.; Saegusa, T.; Ikeda, H. *Macromolecules*, **1981**, *14*, 315.

Clancy, S.; Shriver, D. F.; Ochrymowycz, L. A. *Macromolecules* **1986**, *19*, 606.

Cohen, J. E. *Science* **1995**, *269*, 341.

Cohen, M. H.; Turnbull, D. *J. Chem. Phys.* **1959**, *31*, 1164.

Cohen, M. H.; Grest, G. S. *Phys. Rev. B* **1980**, *B21*, 4113.

Colbow, K. M.; Dahn, J. R.; Haering, R. R. *J. Power Sources* **1989**, *26*, 397.

Costantino, U.; Marmottini, F. *Mater. Chem. and Phys.* **1993**, *35*, 193.

Craven, J. R.; Mobbs, R. H.; Booth, C.; Giles, J. R. M. *Makromol. Chem., Rapid. Commun.* **1986**, *7*, 81.

Dahn, J.R.; Zheng, T.; Liu, Y.; Xue, J.S. *Science* **1995**, *270*, 590.

Daniel, M. F.; Desbat, B.; Sassegues, J. C. *Solid State Ionics* **1988**, *28-30*, 632.

Dion, M.; Piffard, Y.; Tournoux, M. *J. Inorg. Nucl.Chem.* **1978**, *40*, 917.(c)

Doan, K. E.; Heyen, B. J.; Ratner, M. A.; Shriver, D. F. *Chem. Mater.* **1990**, *2*, 539.

Domen, K.; Kudo, A; Shibata, M.; Tanaka, A.; Maruya, K.; Onishi, T. *J. Chem. Soc., Chem. Commum.* **1986**, 1706.

Fauteux, D. *Proc. Electrochem. Soc.* **1994**, *94-28*, 16.

Fauteux, D. *Proceedings of The Electrochemical Society* **1994**, *94-28*, 379.

Fauteux, D. *Electrochim. Acta* **1993**, *38*, 1199.

Fauteux, D. *J. Electrochem. Soc.* **1988**, *135*, 2231.

Ferry, J. *Viscoelastic Properties of Polymers* Wiley: New York, 1980; ch. 11.

Flory, P. J. *Principles of Polymer Chemistry* Cornell, UP: Ithica NY, 1953; ch. 3.

Gauthier, M.; Belanger, A; Kapfer, B.; Vassort, G.; Armand, M. In *Polymer Electrolyte Reviews-2* MacCallum, J. R.; Vincent, C. A. Eds. Elsevier: New York, 1989; p. 285.

Gianncoli, D. C. *Physics* 2nd Ed.; Prentice Hall: New Jersey, 1985; ch.s 15-18.

Giles, J. R. M.; Booth, C.; Mobbs, R. H. *Proceddings, 6th Risø International Symposium on Metallurgy and Materials Science* Risø National Lab., Roskilde; 1985, p. 329.

Gnanou, Y.; Hild, G.; Rempp, P. *Macromolecules* **1987**, *20*, 1662.

Golodnitsky, D.; Ardel, G.; Peled, E. *Electronic Confrence on Solid Electrolytes*, Elsevier, 1995.

Gopalakrishnan, J. *Chem. Mater.* **1995**, *7*, 1265.

Gosser, D. K. *Cyclic Voltammetry* VCH: New York, 1994.

Gray, F. M. in *Polymer Electrolyte Reviews-1*, MacCallum, J. R.; Vincent, C. A. Ed.s, Elsevier Applied Science: London 1987.

Gray, F. M. *Solid Polymer Electrolytes* VCH: New York, 1991.

Grey, I. E.; Madsen, I. C.; Watts, J. A.; Bursill, L. A.; Kwiatkowska, J. *J. Solid St. Chem.* **1985**, *58*, 350.

Grey, I. E.; Li, C.; Madsen, I. C.; Watts, J. A. *J. Solid St. Chem.* **1987**, *66*, 7. (f)

Guerard, D.; Herold, A. *Carbon* **1975**, *13*, 337.

Gummow, R. J.; de Kock, A.; Thackeray, M. M. *Solid State Ionics* **1994**, *69*, 59.

Harris, J. M. Ed. *Poly(ethylene glycol) Chemistry: Biotechnical and Biomedical Applications* Plenum Press: New York, 1992.

Harris, C. S.; Shriver, D. F.; Ratner, M A. *Macromolecules* **1986**, *19*, 188.

Hennink, W.; Juizer, L.; U.S. Patent 5,019,100; 1991.

Ivanova, T.; Melnikov, M.; Fok, N. *Dokl. Akad. Nauk SSR* **1976**, *231*, 649.

Izawa, H.; Kikkawa, S.; Koizumi, M. *Polyhedron* **1983**, *2*, 741.

Jacobson, A. J. *Mat. Sci. For.* **1994**, *152*, 1.

Kalhammer, F. R.; Kozawa, A.; Moyer, C. B.; Owens B. B. *Interface* **1996**, *Spring*, 32.

Karaborni, S.;Smit, B.; Heidug, W.; Urai, J.; van Oort, E. *Science* **1996**, *271*, 1102.

Khan, I. M.; Yuan, Y.; Fish, D.; Wu, E.; Smid, J. *Macromolecules* **1988**, *21*, 2684.

Killis, A.; LeNest, J. F.; Gandini, A.; Cheradame, H.; Cohen-Addad, J. P. *Solid State Ionics* **1984**, *14*, 231.

Killis, A., LeNest, J. F., Cheradame, H.; Gandini, A. *Macromol. Chem.* **1982**, *183*, 2835.

Kim, Y. I.; Atherton, S. J.; Brigham, E. S.; Mallouk, T. E. *J. Phys. Chem.* **1993**, *97*, 11802.

Kim, Y. I.; Salim, S.; Huq, M. J.; Mallouk, T. E. *J. Am. Chem. Soc.* **1991**, *95*, 1345.

King, P. A.; U.S. Patent 3,419,006; 1966.

Kudo, A.; sayama, K.; Tanaka, A.; Asakura, K; Domen, K.; Maruya, K; Onishi, T. *J. Catal.* **1989**, *120*, 337.

Kudo, A.; Tanaka, A.; Domen, K.; Maruya, K; Aika, K.; Onishi, T. *J. Catal.* **1989**, *111*, 67.

Kuruda, N.; Kobayashi, H.; Matsuura, K.; U.S. Patent 4,970,012; 1990.

Laidler, K. J.; Mieser, J. H. *Physical Chemistry* Benjamin/Cummings: Menlo Park, 1982.

Lan, T.; Kaviratna, P. D.; Pinnavera, T. J. *Chem. Mater.* **1995**, *7*, 2144.

Le, D. B.; Passerini, S.; Chu, X.; Chang, D.; Owens, B. B.; Smyrl, W. H. *Proceedings of The Electrochemical Society* **1994**, *94-28*, 306.

Lemmon, J. P., Ph.D. Thesis, Oregon State University, 1994.

Lemmon, J. P.; Lerner, M. M. *Macromolecules* **1992**, *25*, 2907.

Lemmon, J. P.; Wu, J.; Oriakhi, C.; Lerner, M. M. *Electrochim. Acta* **1995**, *40*, 2245.

LeNest, J. F.; Callens, S.; Gandini, A.; Armand, M. *Electrochim. Acta* **1992**, *37*, 1585.

Li, W.; Reimers, J. N.; Dahn, J. R.; *Solid State Ionics* **1994**, in press.

Lightfoot, P.; Metha, M. A.; Bruce, P.G. *J. Mater. Chem.* **1992**, *2*, 379.

Linden, E.; Owen, J. R. *Br. Polm. J.* **1988**, *20*, 237.

Liu, Y.-J.; Schindler, J. L; DeGroot, D. C.; Kannewurf, C. R.; Jirpo, W.; Kanatzidis, M. G. *Chem. Mater.* **1996**, *8*, 525.

Liu, W.; Farrington, G. C.; Chaput, F.; Dunn, B. *J. Electrochem. Soc.* **1996**, *143*, 897.

Lonergan, M. C. Ph.D. Thesis Northwestern Universtiy 1994.

Lonergan, M. C.; Shriver, D. F.; Ratner, M. A. *Electrochim. Acta* **1995**, *40*, 2041.

MacCallum, J. R.; Vincent, C. A. Ed.s *Polymer Electrolyte Reviews - 2* Elsevier: New York, 1989.

MacCallum, J. R.; Vincent, C. A. Ed.s *Polymer Electrolyte Reviews - 1* Elsevier: New York, 1987.

MacCallum, J.R., Smith, M.J., Vincent, C.A. *Solid State Ionics* **1984**, *11*, 307.

Macdonald, J. R. *Impedance Spectroscopy* J. Wiley & Sons: New York, 1987.

MacFarlane, D.; Philpott, A.; Tetaz, J.; U.S. Patents 5,153,820 and 5,146,391; 1992.

Magaura, T. *Prog. Batt. And Batt. Mater.* **1991**, *10*, 209.

Mebrey, M.; Graham, N.; U.S. Patents 5,079,009; 1992. And 5,017,382; 1991.

Mehta, M. A.; Lightfoot, P.; Bruce, P. G. *Chem. Mater.* **1993**, *5*, 1338.

Mizushima, K.; Jones, P. C.; Wiseman, P. J.; Goodenough, J. B. *Mat. Res. Bull.* **1980**, *15*, 783.

Murugesamoorth, K. A.; Owen, J. R. *Br. Polm. J.* **1988**, *20,* 227.

Nafshun, R. L.; Lerner, M. M., 1995, unpublished results.

Nafshun, R. L.; Lerner, M. M.; Hamel, N. N.; Nixon, P. G.; Gard, G. L. *J. Electrochem. Soc.* **1995**, *142* , L153.

Nagoka, K., Naruse, K., Naruse, H., Shinohara, I., Watanabe, M. *J. Polym. Sci. Polym. Let.* **22**, *1984*, 659.

Namilova, V.A.; Guerard, D.; Lelaurain, M.; Fateev, O. *Carbon*, in press.

Nelson, C. J.; Coggio, W. D.; Allcock, H. R. *Chem. Mater.* **1991**, *3*, 786.

Nicholas, C.V.; Wilson, D. J.; Booth, C.; Giles, J. R. M. *Br. Polym. J.* **1988**, *20*, 289.

Ogawa, M.; Kuroda, K. *Chem. Rev.* **1995**, *95*, 399.

Ohzuku, T.; Ueda, A.; Nagayama, M. *J. Electrochem. Soc.* **1993**, *140*, 1862.

Ohzuku, T.; Ueda, A.; Nagayama, M.; Komori, H. *Electrochim. Acta* **1993**, *28*, 1159.

Okada, A.; Fukumori, K.; Usuki, A.; Kojima, Y.; Kurauchi, T.; Kamigaito, O. *Polym. Prepr.* **1991**, *32*, 540.

Okada, A; Kawasumi, M.; Usuki, A.; Kojima, Y.; Kurauchi, T.; Kamigaito, O. *Mater. Res. Soc. Symp. Proc.* **1990**, *171*, 45.

Oriakhi, C., Ph.D. Thesis, Oregon State University, 1996.

Pand, Y.; Mai, S-M.; Huang, K-Y.; Luo, Y-Z.; Thatcher, J. H.; Colley, R. A.; Nicholas, C. V.; Booth, C. *J. Mater. Chem.* **1995**, *5*, 831.

Papke, D. L.; Ratner, M. A.; Shriver, D. F. *J. Electrochem. Soc.* **1982**, *129*, 1694.

Park, H. K.; Smyrl, W. H. *J. Electrochem. Soc.* **1994**, *141*, L25.

Peled, E. *Proc. Electrochem. Soc.* **1994**, *94-28*, 1.

Peled, E. *J. Electrochem. Soc.* **1979**, *126*, 2047.

Peled, E.; Golodnitsky, D.; Ardel, G.; Eshkenazy, V. *Electrochim. Acta* In Press.

Peled, E. *Proceedings of The Electrochemical Society* **1994**, *94-28*, 1.

Peng, X. Ba, H.; Chen, D.; Wang, F. *Electrochim. Acta* **1992**, *37*, 1569.

Pierce, A. E. *Silylation of Organic Compounds* Pierce Chemical Co.: Rockford, 1968.

Ratner, M., Shriver, D.F. *Chem. Rev.* **1988**, *88*, 109.

Ratner, M. A. in *Polymer Electrolyte Reviews-1* MacCallum, J. R.; Vincent, C. A. Ed.s; Elsevier: New York, 1987; ch. 7.

Reimers, J. N.; Fuller, E. W.; Rossen, E.; Dahn, J. R. *J. Electrochem. Soc.* **1993**, *140*, 3396.

Rossen, E; Reimers, J. M.; Dahn, J. R. *Solid State Ionics* **1993**, *62*, 53.

Rossouw, M. H.; Liles, D. C.; Thackeray, M. M. *J. Solid State Chem.* **1993**, *104*, 464.

Rudin, A. *The Elements of Polymer Science* AP: New York, 1982.

Ruiz-Hitzky, E.; Casal, Blanca *J. Chem. Soc., Faraday Trans. 1* **1986**, *86*, 1597.

Sasaki, T.; Watanabe, M.; Komatsu, Y.; Fujiki, Y. *Inorg. Chem.* **1985**, *24*, 2265.

Sasaki, T.; Watanabe, M.; Hashizume, H.; Yamada, H.; Nakazawa, H. *Chem. Commum.* **1996**, 229.

Sasaki, T.; Watanabe, M.; Michiue, Y.; Komatsu, Y.; Izumi, F.; Takenouchi, S. *Chem. Mater.* **1995**, *7*, 1001.

Sayama, K; Tanaka, A.; Domen, K.; Maruya, K.; Onishi, T. *J. Phys. Chem.* **1991**, *95*, 1345.

Scosati, B. in *Electrochemistry of Novel Materials* Lipkowski, J.; Ross, P. N. Ed.s; VCH: New York, 1994; ch. 3.

Scrosati, B. *Br. Polym. J.* **1988**, *20*, 219.

Scrosati, B. in *Electrochemistry of Novel Materials* Lipkowski, J.; Ross, P. N. Eds., VCH: New York, 1994, chapter 3.

Shackle, D.; Lee, M. ; U.S. Patent 5,037,712; 1991.

Shodai, T.; Sakurai, Y.; Okada, S. *Proceedings of The Electrochemical Society* **1994**, *94-28*, 224.

Shriver, D. F.; Bruce, P. G. in *Solid State Electrochemistry*, P.G. Bruce, Ed., Cambridge University Press: New York, 1995.

Shu, Z. X.; McMillan, R. S.; Murray, J. J *J. Electrochem. Soc.* **1993**, *140*, 992.

Sloop, S. E.; Lerner, M. M.; Stephens T. S.; Tipton, A. L.; Paull, D. G.; Stenger-Smith, J. D. *J. Appl. Polym. Sci.* **1994**, *53*, 1563.

Sonntag, C.; Schuchmann, J.; Schomberg, G. *Tetrahedron* **1972**, *28*, 4333.

Sørensen, P. R.; Jacobsen, T. *Electrochim. Acta* **1982**, *27*, 1671.

Sperling, L. Ed., *Introduction to Physical Polymer Science* Wiley: New York, 1986.

Stead, J. B.; Hindley, A. H. *J. Chromatog.* **1969**, *42*, 470.

Steele, B. C. H; Lagos, G. E.; Spurgens, P. C.; Forsyth, C. Foord, A. D. *Solid State Ionics* **1983**, *9/10*, 391.

Strazielle, C. *Makromol. Chem.* **1958**, *119*, 50.

Streitwieser, A. Jr.; Heathcock, C. H. *Introduction to Organic Chemistry - 2nd Ed.* Macmillan: New York, 1981.

Suziki, D. Keynote Address to the National Science Teachers Association, Seattle, Wa. 1989.

Tagaya, H.; Saito, K.; Kusahara, T.; Kadokawa, J.; Chiba, K. *Catal. Today* **1993**, *16*, 463.

Takahara, Z.; Ogumi, Z.; Kanamura, K.; Uchimoto, Y. *The Electrochemical Society Fall Meeting*, New Orleans, Louisiana, Oct. 10-15, 1993, extended abstract no. 4.

Takahashi, Y.; Takadoro, H. *Macromolecules* **1973**, *6*, 672.

Thackeray, M. M.; de Kock, A.; Rossouw, M. H.; Liles, D. C.; Hoge, D.; Bittihn, R.; *J. Electrochem. Soc.* **1992**, *139*, 363.

Thackeray, M. M. *Proceedings of The Electrochemical Society* **1994**, *94-28*, 233.

Thakeray, M. M.; David, W. I. F.; Goodenough, J. B. *Mat. Res. Bull.* **1982**, *17*, 785.

Thomas, D. M.; McCarron, E. M.; *Mat. Res. Bull.* **1986**, *21*, 945.

Torell, L. M.; Schantz, S. Polymer *Electrolyte Reveiws-2* Eds Maccallum, J. R. and Vincent, C. A., Elsevier Applied Science, NY, p. 1.

Törnquist, J. *Acta Chem. Scand.* **1967**, *21*, 2095.

Wadsley, A. D. *Acta Cryst.* **1964**, *17*, 623.

Watanabe, M.; Oohashi, S.; Sanui, K.; Ogata, N.; Kobayashi, T.; Ohataki, Z. *Macromolecules* **1985**, *18*, 1945.

Weiss, A.; Weiss, A. *Angew. Chem.* **1960**, *72*, 413.

West, A. R. *Solid State Chemistry and its Applications* John Wiley & Sons: New York, 1992.

Willner, I.; Eichen, Y.; Frank, A. J.; Fox, M. A. *J. Phys. Chem.* **1993**, *97*, 7264.

Xia, D. W.; Soltz, K.; Smid, J. *Solid State Ionics* **1984**, *14*, 221.

Yamamoto, O. in *Solid State Electrochemistry* Bruce, P. G. Ed.; Cambridge, New York, 1995; ch. 11.

Yankov, L.; Filipova, S.; Zlatonov, I.; Budevski, E. ; U.S. Patent 4,959,396; 1990.

Yano, K.; Usuki, A.; Okada, A.; Kurauchi, T.; Kamigaito, O. *Polym. Prepr.* **1991**, *32*, 65.

Yata, S. et al., *Synth. Met.* **1994**, *62*, 153.

Young, L. *Anodic Oxide Films* Academic Press: New York, 1961.

Zelewsky, A. von; Barbosa, L.; Schlapfer, C. W. *Coord. Chem. Rev.* **1993**, *123*, 229.

Zhang, L.; Zhang, W.; Zhang Z.; Yu, L.; Zhang, H.; Qi, Y.; Chen, D. *Radiat. Phys. Chem.* **1992**, *40*, 501.

Zheng, T. et al. *J. Electrochem. Soc.* **1995**, *142*, 1281.